3D Micro-Architected Materials for Batteries

Thesis by

Yuchun Sun

In Partial Fulfillment of the Requirements for

the Degree of

Doctor of Philosophy

CALIFORNIA INSTITUTE OF TECHNOLOGY

Pasadena, California

2024

Defended March 26, 2024

Yuchun Sun
ORCID: 0000-0002-7028-3523

ACKNOWLEDGEMENTS

This voyage has unfolded as the most challenging but exhilarating chapter in my life. I have been very fortunate to have all the wonderful colleagues and friends throughout my PhD journey. First, I would like to thank my advisor, Prof. Julia R. Greer, for her enthusiastic support and patient guidance over the years. Thank you for leading me into the world of science, caring about me as a friend, and entrusting me with the independence to explore freely and forge my own path. I also want to thank Prof. Katherine T. Faber, Prof. Kimberly A. See, and Dr. William C. West for their insightful advice as members of my thesis committee.

I sincerely appreciate all the support from everyone in the Greer group. I would like to thank the former battery-troops, Dr. Xiaoxing Xia, Dr. Michael A. Citrin, Dr. Kai Narita, Dr. Max A. Saccone, Dr. Fernando J. Villafuerte and Dr. Heng Yang, for sharing their knowledge and inspiring my research. I'm also grateful for all the insightful discussions with Yingjin Wang and Ethan Klein, the current members of battery subgroup. I would like to thank my cohort in the Greer group, Dr. Weiting Deng and Dr. Andrew C. Friedman, for sharing joys and facing fears together with me on this journey. I want to thank my lovely former and current office mates, Dr. Ryan C. Ng, Dr. Amylynn C. Chen, Dr. Weiting Deng, Seola Lee and Yingjin Wang, for encouraging me in all those days and nights and supporting me through all the highs and lows. I would like to thank all the current Greer group members for standing by me throughout the journey of completing my thesis. Thank you to Wenxin Zhang, Thomas T. Tran, Cyrus Fiori and Ethan Klein for your insightful feedback on this thesis. Thank you to Sammy Shaker, Kevin H. Nakahara and Wenyuan Chen for the inspiring discussions. I would also like to thank the former Greer group members, Dr. Haolu Zhang, Dr. Bryce W. Edwards, Dr. Anthony Kwong, Dr. Daryl W. Yee and Dr. Rebecca A. Gallivan, for training me with great patience, and Dr. Carlos M. Portela, Dr. Luizetta V. Elliott, Dr. Andrey Vyatskikh and Dr. Widianto P. Moestopo, for providing insights that helped me shape my projects.

I'm grateful for Dr. Ruoqian Lin, Hui Li Seong and Matthew Salazar for being so knowledgeable and enthusiastic to collaborate with me. I would like to thank Dr. Chi Ma, Dr. Nathan F. Dalleska and Alex Wertheim for all the help and advice. I want to thank my Materials Science cohort, Dr. Chen-Hsuan Lu, Zachery W. Iton, Magel P. Su and Benjamin Hatanpaa, for the amazing times we spent together in and out of the classroom. I would also like to thank all my best friends at Caltech, Xiaoqiao Chen, Dr. Ruizhi Cao, Yongzhao Guo, Dr. Zhiquan Yuan, Yang Zhang, Dr. Ding Zhong, Dr. Cheng Shen, Dr. Tianzhe Zheng and Dr. Lue Wu for all the wonderful moments we shared and the countless enjoyable weekends we spent together in the past five years.

Finally, I want to convey my deepest gratitude to my family. Thank you to my parents, Jun Hu and Peidong Sun, for their unconditional love and support. Thank you to the love of my life, Tian Xie, for his continuous support. Thank you for being an incredible husband, and for always being there. I wouldn't have made it through all the difficulties if it weren't for the love from all of you that I'm so fortunate to have.

ABSTRACT

Additive manufacturing (AM) enables three-dimensional micro-patterning of battery electrode materials, permitting complex structural designs beyond those of traditional slurry electrodes. We demonstrate two novel AM approaches for architecting electrode materials in lithium-ion batteries. First, we introduce a process for fabricating 3D micro-architected cathodes utilizing gel infusion additive manufacturing, and demonstrate this technique with lithium cobalt oxide (LCO). This method combines VP-based 3D printing with subsequent ion infusion and calcination processes. It starts with the printing of a blank organogel structure using a customized acrylate-based photoresin. This organogel is then converted into a hydrogel, infused with lithium and cobalt precursors, and finally subjected to calcination to form the LCO structure. This technique achieves 3D micro-architected LCO lattices with beam diameters of 45 μm, and maintains the designed architecture with tunable microstructures. By fabricating 3D micro-architected $LiNi_{0.33}Mn_{0.33}Co_{0.33}O_2$ (NMC111) through a very similar process, we demonstrate the potential for this gel infusion additive manufacturing method to engineer a variety of cathode materials for lithium-ion batteries in 3D.

We also develop a fabrication method to create 3D lithium anodes supported by micro-architected carbon scaffold. By pyrolyzing 3D printed polymer microlattices, mechanically robust carbon electrodes are produced. Their micro-scale features and flexible structural control make them suitable as scaffolds for lithium-metal anodes. Surface functionalization and lithium electrodeposition are explored for dense lithium nucleation and uniform epitaxial growth on the carbon framework, resulting in micro-architected lithium/carbon anodes. With the rapid development of high-resolution AM techniques in recent decades, these approaches to additively manufacture cathode and anode materials provide promising pathways to build batteries with customizable 3D designs, and pursue higher energy and power densities for different applications.

PUBLISHED CONTENT AND CONTRIBUTIONS

1. K. Narita, M. A. Saccone, Y. Sun, J. R. Greer, "Additive Manufacturing of 3D Batteries: A Perspective." *J. Mater. Res.* **2022**, *37*, 1535. DOI: 10.1557/s43578-022-00562-w.

Contributions: Y.S. helped conceive the paper structure and wrote the manuscript.

Chapter 1.2–1.3, Chapter 2, and Chapter 4.2 have been adapted from

2. Y. Sun, J. R. Greer, "Micro-Architected Lithium Cobalt Oxide for Batteries." *In Preparation.*

Contributions: Y.S. conceived the study, developed the fabrication process, fabricated all samples, designed and performed the experiments, analyzed the data, and wrote the manuscript.

Chapter 3 has been adapted from

3. Y. Sun, H. L. Seong, J. Pasalic, M. Smart, J. R. Greer, "Micro-Architected Lithium/Carbon Anode for Rechargeable Lithium Metal Batteries." *In Preparation*.

Contributions: Y.S. conceived the study, developed the fabrication process, fabricated samples, designed and performed the experiments, analyzed the data, and wrote the manuscript.

TABLE OF CONTENTS

LIST OF FIGURES

LIST OF TABLES

Chapter 1

INTRODUCTION: ADDITIVE MANUFACTURING OF 3D-ARCHITECTED ELECTRODE MATERIALS FOR LIHTIUM-ION BATTERIES

1.1 Potentials and Challenges of Lithium-Ion Batteries

In recent decades, lithium-ion batteries have profoundly transformed various aspects of our daily lives. With high energy density and the lightweight nature, they have revolutionized portable electronic devices including smartphones, laptops and wearable technologies, which in turn have fundamentally changed how people communicate and access information [1]. Portable medical devices such as pacemakers, insulin pumps and oxygen concentrators, and portable household appliances such as electric toothbrushes, handheld vacuum cleaners and cordless power tools also grew more durable, powerful, and compact due to the advancements in lithium-ion battery technologies. They are also significantly accelerating the transition from traditional gasoline-powered vehicles to electric vehicles (EVs) by making EVs more viable and competitive, supplying longer driving ranges, shorter charging times, and generally greater performance than earlier rechargeable battery technologies [2,3]. This shift helps to reduce the emission of CO_2 and other greenhouse gases and decrease reliance on fossil fuels, contributing to environmental and energy sustainability. Lithium-ion batteries are also increasingly used for another important sustainability effort: the integration of renewable energy into the grid [4]. Many renewable energy sources like solar and wind are intermittent by nature and highly variable in their output. As a result, they require the storage of excess energy generated during the peak hours for use when the production is lower. Lithium-ion batteries are becoming key components in energy storage systems, facilitating a more stable and reliable energy grid. In addition to these impacts on our daily lives, lithium-ion batteries are used in many aerospace applications, powering drones, satellites, and space exploration vehicles [5]. Their high energy density and durability make them suitable for these critical applications in challenging environments.

The commercialization of lithium-ion batteries began in the 1970s with Whittingham's discovery of reversible lithium intercalation in TiS_2 [6]. In 1980, Goodenough reported $LiCoO_2$ as a cathode material which enabled a 4.0 V rechargeable battery against lithium metal [7]. Yoshino developed an efficiently working lithium-ion battery with heat-treated petroleum coke as anode and $LiCoO_2$ as cathode in 1985 [8], which was then successfully commercialized by Sony in 1991 [8]. Lithium-ion batteries have significantly advanced the performance of rechargeable batteries compared to earlier technologies like nickel-cadmium or nickel-metal hydride batteries [9]. With a standard reduction potential of -3.04 V versus the standard hydrogen electrode, lithium has the highest electrochemical potential of any metal, which allows it to drive higher voltage reactions when paired with various materials in a battery's cathode [10]. The higher battery voltage translates to higher power output for a given current, contributing to a higher energy density relative to both weight and volume. The lithium intercalation mechanism, which involves the insertion and removal of lithium ions into and from electrode materials without significant alteration of the material's structure, offers better electrochemical and mechanical stabilities [11,12]. The minimal material volume change reduces the stress on the battery's internal structure during cycling and enhances its mechanical stability, which leads to less capacity loss over time.

Slurry-based electrodes are commonly used in most commercial lithium-ion batteries. They are manufactured by creating a slurry mixture that contains the cathode or anode active material particles, conductive additives, and binders dissolved in a solvent [13]. This slurry is coated onto a metal foil which serves as the current collector, and then dried to remove the solvent, leaving behind a thin and uniform film of the solid slurry mixture. The commercial slurry electrode films, with a stochastic porous structure, is usually limited to a thickness of 50–100 μm to balance between energy and power densities [14]. For a specific electrode material, higher energy density requires either higher thickness or lower porosity of the slurry film, and both of which reduce its power density. For lithium-ion battery electrodes, this trade-off between energy and power densities poses a significant challenge to improve battery performance. To overcome this limitation, battery electrodes with controlled structures have been proposed.

1.2 3D Batteries and 3D-Architected Electrodes

Beyond conventional batteries with stacked 2D layers of slurry electrodes, various 3D battery architectures have been explored as a means of pursuing higher energy density and power density since they maximize cell volume loading while minimizing transport lengths for ions and electrons. As illustrated in Figure 1.1, Long et al. outlined in their review article from 2004 four representative designs: interdigitated arrays of cathode and anode cylinders; interdigitated electrode plate arrays; arrays of one electrode cylinders with in-filled counter electrodes; and an aperiodic porous electrode with an in-filled counter electrode [15].

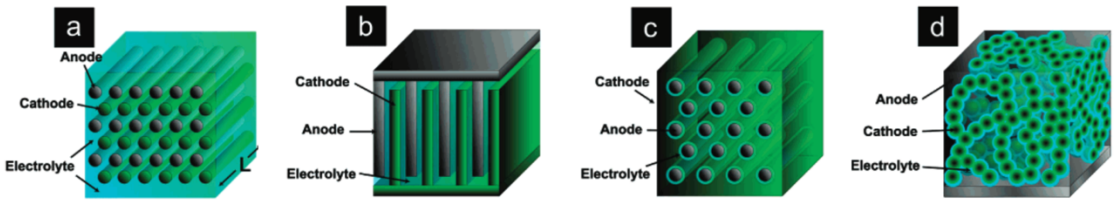

Figure 1.1 Illustrations of 3D batteries. Designs include a) interdigitated arrays of cathode and anode cylinders, b) interdigitated electrode plate arrays, c) arrays of one electrode cylinders with in-filled counter electrodes, and d) an aperiodic porous electrode with an in-filled counter electrode. Adapted with permission from reference [15]. Copyright 2004 American Chemical Society.

3D batteries with the interdigitated plate configuration have been successfully created with direct ink-writing, an extrusion-based 3D printing technique [16,17]. Semiconductor-based processes have been utilized to fabricate 3D-architected anode arrays of 100 μm diameter cylinders with in-filled cathode slurries, although the anode material was limited to silicon, a material known for its enormous volume expansion upon lithiation which often results in rapid mechanical degradation of the battery [18]. Many attempts for other materials in this rod-array geometry are limited to single electrodes [19,20]. The last design, requiring a conformal solid electrolyte layer on all surfaces of one electrode and dense counter electrode in-fill into micro or nanopores, has yet to be realized with existing manufacturing techniques, and the state-of-the-art works are mostly limited to the fabrication of a single electrode with aperiodic porous structures [21].

1.3 Techniques to Fabricate 3D-Architected Electrode Materials

Additive manufacturing (AM) offers an efficient approach to construct self-supporting, three-dimensional (3D) electrode architectures for batteries. Among the diverse range of AM techniques, the extrusion-based direct ink-writing (DIW) stands out as an early technique to fabricate 3D architected electrode materials. Typically, a viscous ink as a blend of active material particles, polymers, and solvents is extruded through a nozzle and solidified upon layering to build a prescribed 3D structure. Sun et al. have demonstrated in their pioneering work the utility of DIW to fabricate $LiFePO_4$ and $Li_4Ti_5O_{12}$ interdigitated electrodes for a 3D battery (Figures 1.2a–b) [16]. Using this technique, Fu et al. also created a similar interdigitated battery with the same cathode and anode active materials, with the addition of graphene oxide for improved ink rheology (Figures 1.2c–d) [17].

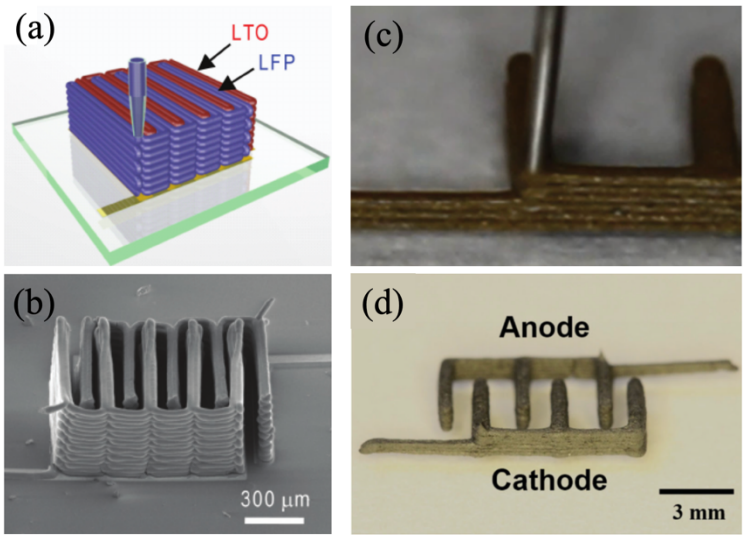

Figure 1.2 Examples of 3D interdigitated electrodes for lithium-ion batteries printed via direct ink-writing. a) Schematic and b) SEM image of interdigitated $LiFePO_4$ cathode and $Li_4Ti_5O_{12}$ anode. Adapted with permission from reference [16]. Copyright 2013 Wiley. Optical images of c) an electrode being printed and d) the interdigitated battery electrodes for a 3D lithium-ion battery with $LiFePO_4$/graphene oxide cathode and $Li_4Ti_5O_{12}$/graphene oxide anode. Adapted with permission from reference [17]. Copyright 2016 Wiley.

Although DIW enables AM of a wide range of materials, it encounters intrinsic limitations due to the viscous nature of the ink, requiring additional support structures for overhanging parts, which complicates post-print processing and renders it incapable of producing features with micron- and sub-micron resolution while maintaining adequate pattern fidelity. These limitations restrict most ink-written electrode geometries to vertically stacked 2D-patterned layers, whose aspect ratios are constrained by the maximum number of layers that can be self-supporting when vertically stacked [16,17]. The electrode feature sizes are predominantly determined by the extrusion nozzle diameter, which must accommodate the rheological properties of the viscous inks. Thinner nozzles enable the production of finer features but are more susceptible to clogging. Typical line thicknesses of ink-written 3D microlattice electrodes are around 200–400 μm, as demonstrated by Lacey et al. in their 3D graphene oxide electrodes shown in Figures 1.3a–b [22] and Gao et al. in the sulfur/carbon composite electrodes shown in Figures 1.3c–d [23].

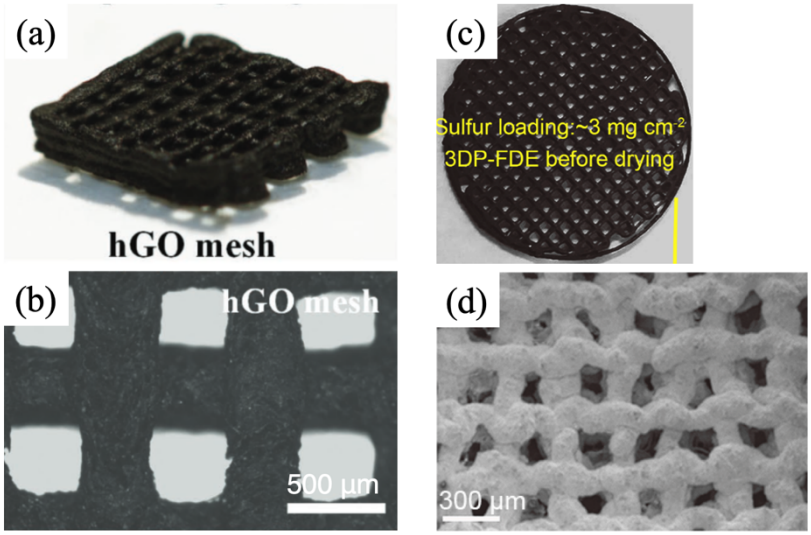

Figure 1.3 Examples of 3D microlattice electrodes printed via direct ink-writing. a) Optical image of a holey graphene oxide (hGO) 3D microlattice electrode and b) a top-view of the lattice mesh. Adapted with permission from reference [22]. Copyright 2018 Wiley. c) Optical image of a sulfur/carbon 3D microlattice electrode and d) top-view SEM image of the lattice mesh. Adapted with permission from reference [23]. Copyright 2018 Elsevier.

Vat photopolymerization (VP) 3D printing is a promising technique that allows for the fabrication of high-resolution three-dimensional architectures compared with traditional 3D printing and offers significant flexibility and control of attainable geometries and printing parameters. This method utilizes a photo-polymerizable liquid resin, which can be uniquely synthesized and cured with UV light layer-by-layer to produce the computed or designed 3D structures. For example, during the digital light processing (DLP) 3D printing, a high-resolution VP 3D printing technique, as illustrated in Figure 1.4a, a strong UV light is redirected by a digital micromirror to project a light pattern of one layer of the 3D model through a transparent window. Above the window, there is liquid photoresin containing oligomer molecules, photoinitiator which starts the chain reaction, and UV blocker to prevent UV light from penetrating too deeply into the resin. UV light penetration into the resin follows the Beer-Lambert law,

$$I(l) = I_0 e^{-\mu l}$$

where I_0 is the initial light intensity, μ is the attenuation coefficient, l is the length of the travelling path of light and $I(l)$ is the light intensity after travelling a distance l (Figure 1.4b). The liquid resin will cure into a solid when it receives a sufficient dose of energy, where the dose is the product of light intensity and exposure time.

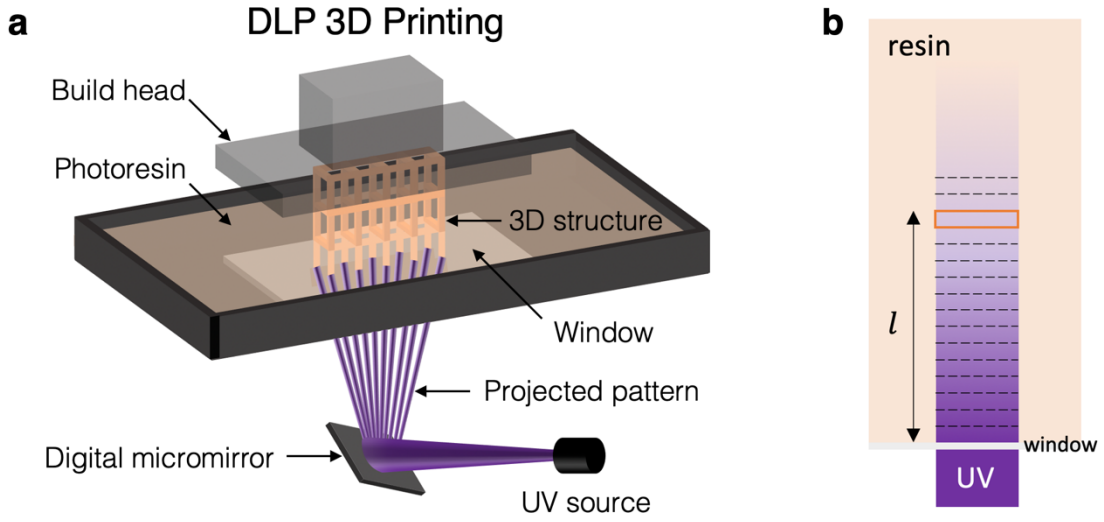

Figure 1.4 Schematics of a) digital light processing (DLP) 3D printing and b) UV light travelling through a transparent window and penetrating into the photoresin.

VP 3D printing technique provides a promising pathway for the fabrication of 3D architected carbon as the anode material for lithium-ion batteries, as demonstrated by Narita et al. (Figure 1.5) [24]. By pyrolyzing a printed polymer microlattice, a 3D architected carbon electrode with beam diameters as small as 28 μm was fabricated.

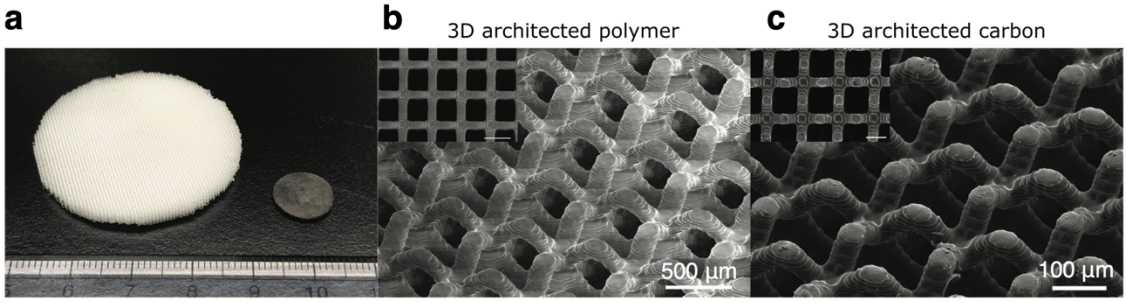

Figure 1.5 Example of 3D carbon microlattice. a) Optical image of a printed 3D architected polymer lattice and the corresponding 3D architected carbon lattice after pyrolysis. SEM images of b) the printed 3D architected polymer lattice and c) the 3D architected carbon lattice. Adapted with permission from reference [24]. Copyright 2020 Wiley.

Unlike the straightforward conversion of 3D printed polymer lattices into carbon anodes through pyrolysis, VP-based AM techniques face more challenges to fabricate cathode materials for lithium-ion batteries, mainly with incorporating the desired electrode materials into the 3D printed polymer structure. A common strategy is to incorporate the powder of the desired battery electrode material into the photoresin, followed by a post-print thermal process to remove polymers [25]. Unlike DIW, significant challenges arise from the presence of particles in the photoresin due to their absorption and scattering of UV light, leading to inhomogeneous polymerization and a diffused gelation profile as demonstrated in Figure 1.6. Moreover, particle sedimentation in the resin suspension often occurs in long prints of several hours, which gives nonuniform density throughout the 3D structure.

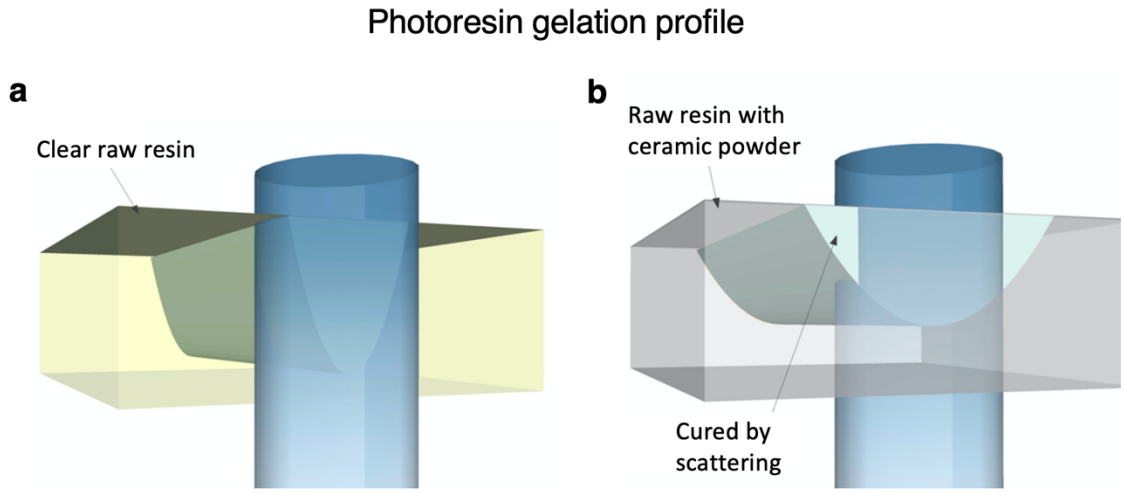

Figure 1.6 Comparison between photoresin gelation profiles of a) clear raw resin and b) a resin suspension with ceramic powders, when a laser beam scans a straight line with the same exposure time. Adapted with permission from reference [25] under open-access CC-BY license.

In an alternative approach, pioneering works have explored dissolving soluble precursors for the desired battery electrode materials in the photoresin rather than by suspending them as insoluble powders, and synthesizing the electrode material during post-print thermal processing. For example, as shown in Figure 1.7a–c, Yee et al. demonstrated the additive manufacturing of a 3D $LiCoO_2$ lattice by printing a hydrogel using an aqueous photoresin containing lithium and cobalt nitrates followed by calcination [26]. This method opens a pathway for high-resolution AM of battery electrode materials, but its generalization for a broader range of materials is hindered by the need to individually customize photoresin composition and optimize 3D printing parameters for each material. The solubility of electrode material precursors limits possible candidate solvent, photoinitiator, and UV blocker chemicals, and their interactions with UV light further complicates the photoresin design for high-resolution print. In the state-of-art works, 3D electrodes fabricated in this manner achieve beam diameters of 100–300 μm, as shown in Figure 1.7 [26,27].

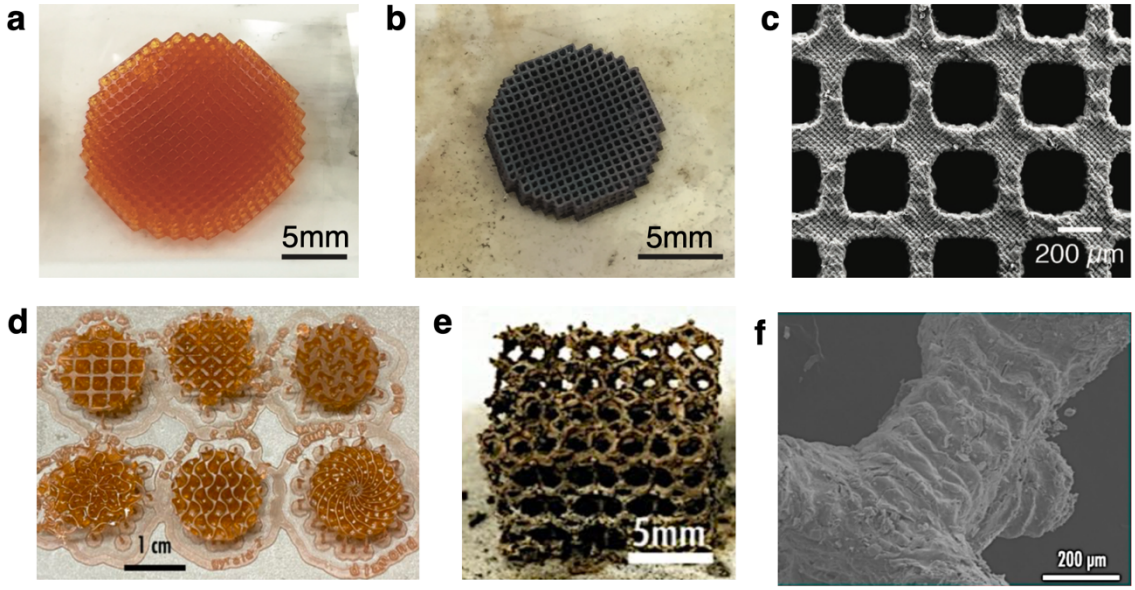

Figure 1.7 Examples of 3D $LiCoO_2$ (LCO) and $LiNi_{0.33}Mn_{0.33}Co_{0.33}O_2$ (NMC111) microlattices. Optical images of a) a 3D architected hydrogel lattice printed with a vat photopolymerization 3D printer, with lithium and cobalt nitrates dissolved in the aqueous photoresin and b) the corresponding 3D architected LCO lattice after calcination. c) SEM image of the LCO lattice from top-view. Adapted with permission from reference [26]. Copyright 2020 Wiley. Optical images of d) a 3D architected hydrogel lattice printed with a vat photopolymerization 3D printer, with lithium, nickel, manganese and cobalt nitrates dissolved in the aqueous photoresin and e) the corresponding 3D architected NMC111 lattice after calcination. f) SEM image of a beam of the NMC111 lattice. Adapted with permission from reference [27] under open-access CC-BY license.

Chapter 2

GEL INFUSION ADDITIVE MANUFACTURING OF MICRO-ARCHITECTED LITHIUM COBALT OXIDE

2.1 Overview

Building on the advancements in vat-photopolymerization (VP) 3D printing and addressing its challenges, we developed a gel infusion AM technique for creating micro-architected battery electrode materials, demonstrating with the fabrication of $LiCoO_2$ (LCO) 3D microlattices. The process starts with VP 3D printing to create a blank organogel microlattice. The absence of electrode material powders or their precursors in the photoresin prevents undesired UV absorption and scattering during printing. After solvent exchange, the gel is infused with LCO precursors, which then undergoes a high-temperature synthesis process. A 3D LCO microlattice preserving the designed architecture while achieving 45 μm beam diameters is synthesized, with promising electrochemical and mechanical functionalities and tunable microstructures. This method utilizes VP's advantage of high resolution while simplifying photoresin design, making it adaptable for a wide range of battery electrode materials.

2.2 Gel Infusion Additive Manufacturing Technique

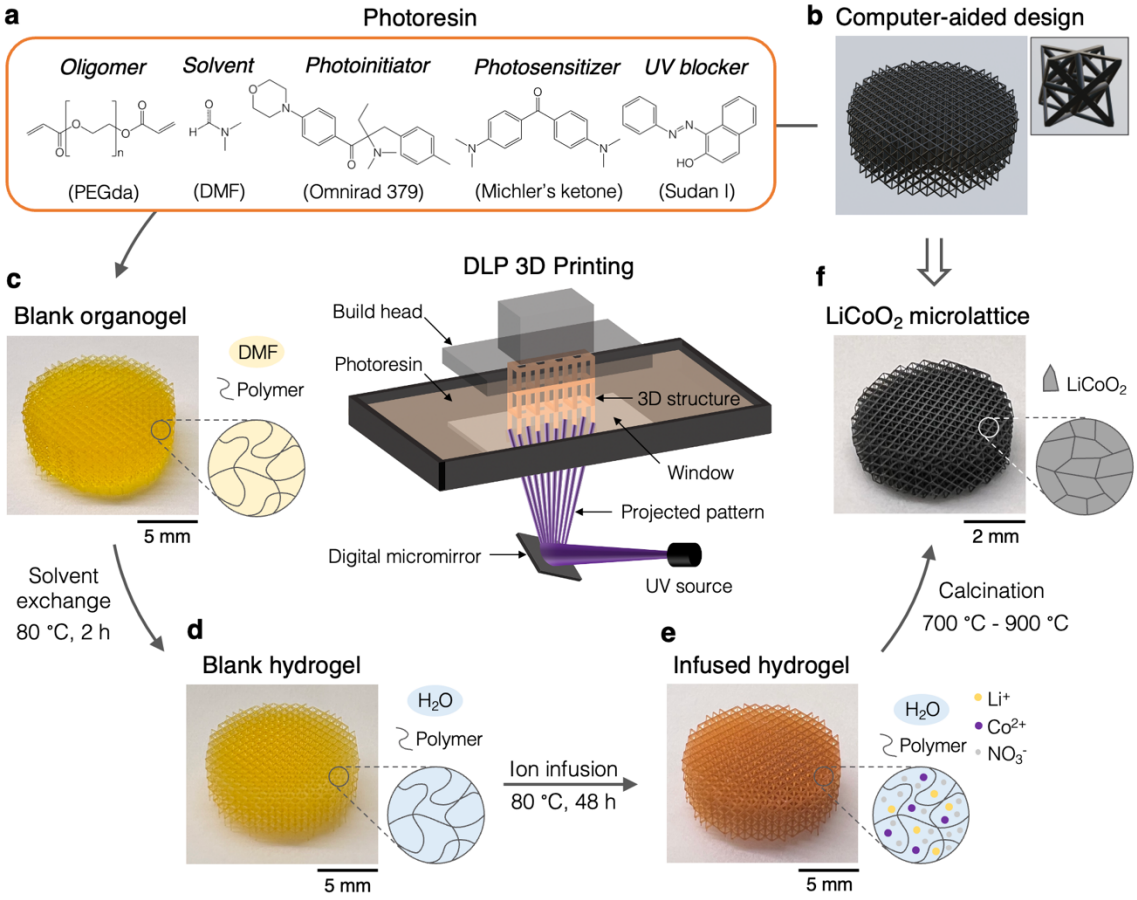

Figure 2.1 Fabrication of 3D micro-architected LCO using the gel infusion additive manufacturing technique. Schematic of digital light processing (DLP) 3D printing (center). a) Composition of the photoresin for vat-photopolymerization 3D printing. b) Computer-aided design (CAD) of an octet truss 3D lattice, with unit cell shown on the right. Optical images and schematics of corresponding compositions of c) printed blank organogel after soaked in *N,N*-Dimethylformamide (DMF), d) blank hydrogel, e) infused hydrogel and f) synthesized LCO microlattice.

Figure 2.1 illustrates the gel infusion AM processes of the 3D-architected gels and LCO microlattice. A digital light processing (DLP) 3D printer is used where high intensity 385 nm UV light is redirected by a digital micromirror and projected through a transparent window into the liquid photoresin, which cures an entire layer of resin at once, realizing 3D structures through layer-by-layer printing. Composition of the customized acrylate-based photoresin is

shown in Figure 1a with details listed in Table 2.1.To prepare the photoresin, 57.5 g (0.10 mol) of poly(ethylene glycol) diacrylate (PEGda, M_n = 575) was dissolved in 40 mL *N,N*-Dimethylformamide (DMF). 506.1 mg (1.33 mmol) of 2-dimethylamino-2-(4-methyl-benzyl)-1-(4-morpholin-4-yl-phenyl)-butan-1-one (Omnirad 379), 335.4 mg (1.25 mmol) of Bis[4-(dimethylamino)phenyl]methanone (Michler's ketone) and 14.90 mg (0.06 mmol) of 1-(Phenyldiazenyl)naphthalen-2-ol (Sudan I) were dissolved in 11.3 mL of DMF separately, and then mixed with the previous solution to form a clear photoresin with orange color.

Component	Amount
N,N-Dimethylformamide	51.3 mL
Poly(ethylene glycol) diacrylate (average M_n 575)	0.10 mol
Omnirad 379	1.33 mmol
Michler's ketone	1.25 mmol
Sudan I	0.06 mmol

Table 2.1 Composition of the customized arylate-based photoresin for VP 3D printing.

Starting with the 3D lattice from computer-aided design (CAD, Figure 2.1b), an organogel 3D lattice (Figure 2.1c) is printed with Titan 3 printer from MicroSLA, using the printing parameters shown in Table 2.2. We demonstrate the process with an octet truss lattice which has hanging beams in horizontal and 45° angled directions, to demonstrate the versatility of this AM method to fabricate sophisticated micro-scale 3D structures, challenging for extrusion-based 3D printing techniques.

Slice thickness (mm)	0.01	**LED Current (5.86 mA per unit)**	300	
	Exposure Time (s)	**Lift Height (mm)**	**Lift Speed (mm min^{-1})**	**Down Speed (mm min^{-1})**	**Delay Time (s)**
First layer	3	7	10	150	2
Remaining layers	0.8	7	25	150	2

Table 2.2 Printing parameters for the customized photoresin using Titan 3 DLP printer (MicroSLA).

Using a printer with 25 μm XY pixel size and 10 μm layer thickness, a gel with cylindrical beams of 120 μm in diameter and 707 μm in length is printed (Figure 2.2). The overall geometry was designed to be circular, with 12.8 mm in diameter and 4.5 mm in thickness. The periodic surface roughness is due to the square pixels and layer thickness in DLP 3D printing. The printed gel is soaked in DMF for 2 hours to remove photosensitizer and UV blocker, and then is subjected to solvent exchange in water at 80 °C for 2 hours, transforming it into a hydrogel (Figure 2.1d). The hydrogel is infused in a 2M $LiNO_3$ and $Co(NO_3)_2$ aqueous solution at 80 °C for 48 hours (Figure 2.1e). Upon reaching ion infusion equilibrium, indicated by stable gel mass discussed in Chapter 2.3, the gel is calcined and sintered in a tube furnace to synthesize LCO, giving 3D architected LCO microlattice with the same geometry as designed in CAD (Figure 2.1f). The overall dimensions of the LCO lattice experience an isotropic linear shrinkage to around 40% of the infused gel.

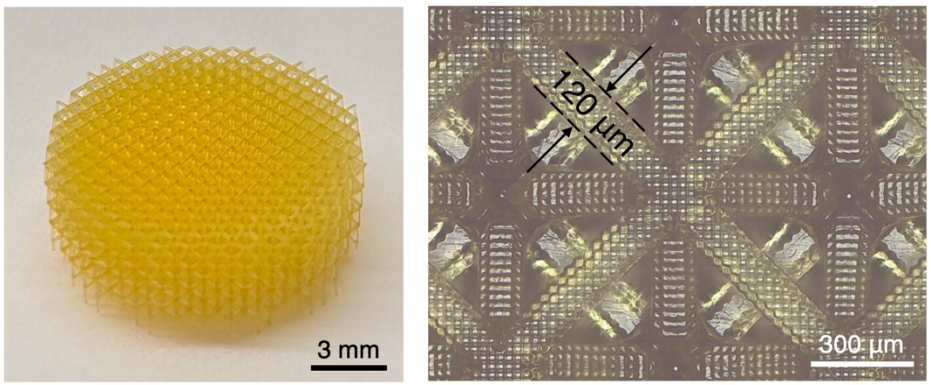

Figure 2.2 Optical and optical microscope images of a 3D printed gel microlattice.

During 3D printing of the microlattice, it is important to set the lift height larger than the sample thickness to allow the liquid photoresin to drain out of the structure between the printing of adjacent layers. If the resin draining is not sufficient, when the accumulated dose of scattered UV light in the trapped resin exceeds the gelation dose over the curing of multiple layers, resin will partially cure and form solid in the pores, giving undesired features on the printed structure. Figure 2.3 shows images of a printed gel with overall sample thickness of

4.5 mm and lift height set to 2 mm. Resin near the center of the sample was significantly trapped, which caused undesired gelation in the pores.

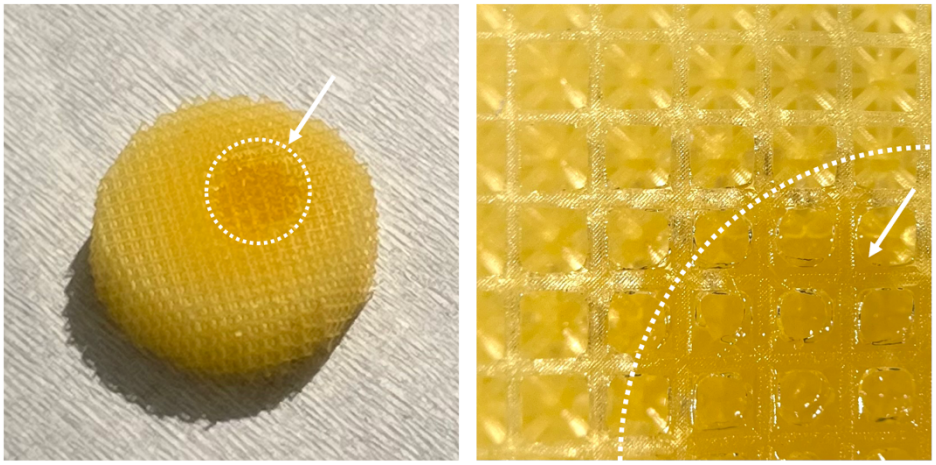

Figure 2.3 Optical images of a 3D printed gel with photoresin gelation in the pores of the microlattice.

Figure 2.4 shows the 3D architected LCO microlattice in multiple scales. Figure 2.4b presents a top-view scanning electron microscope (SEM) image of the LCO octet truss lattice, which has beam diameters of 45 μm, as shown in Figure 2.4c. The characteristic pixel-type surface roughness from DLP 3D printing is retained on the synthesized LCO structure. Figure 2.4d captures a representative image of LCO grains on the surface of the microlattice.

In addition to the octet truss lattice, LCO fabricated in cubic lattices with various beam diameters and unit cell sizes are highlighted in Figure 2.5, demonstrating the versatility and design freedom offered by this gel infusion AM process for creating diverse architectures of electrode materials.

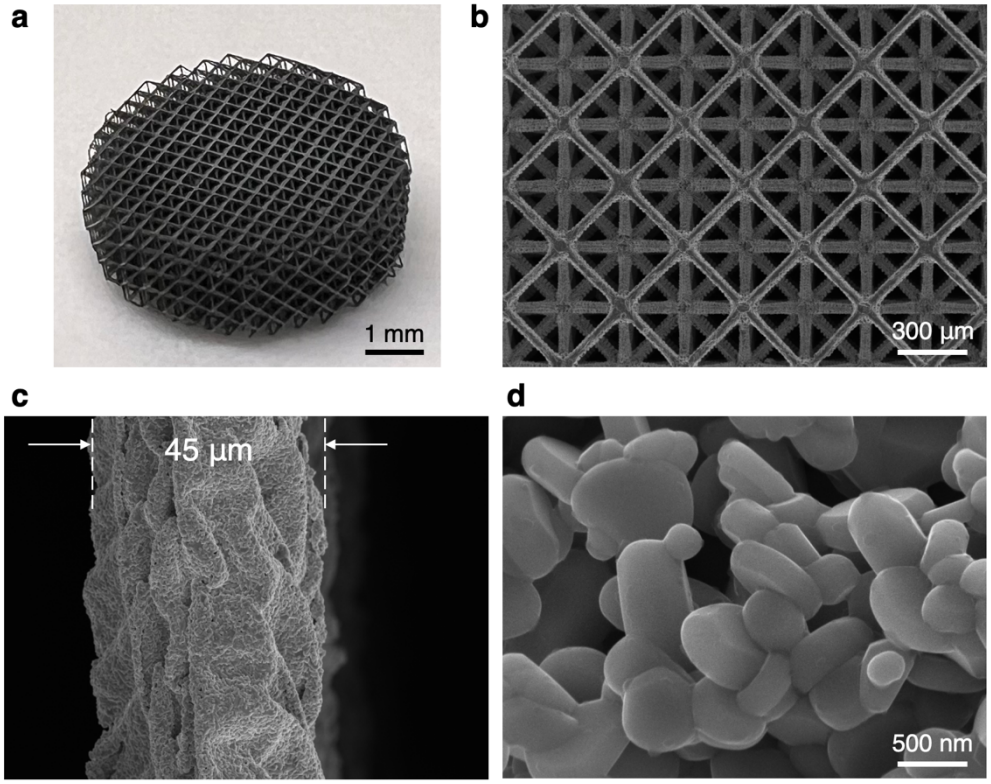

Figure 2.4 a) Optical image and b) SEM image in top view of a 3D micro-architected LCO octet truss lattice. c) SEM image of a beam in the LCO microlattice. d) SEM image of LCO grains on the surface of the LCO microlattice.

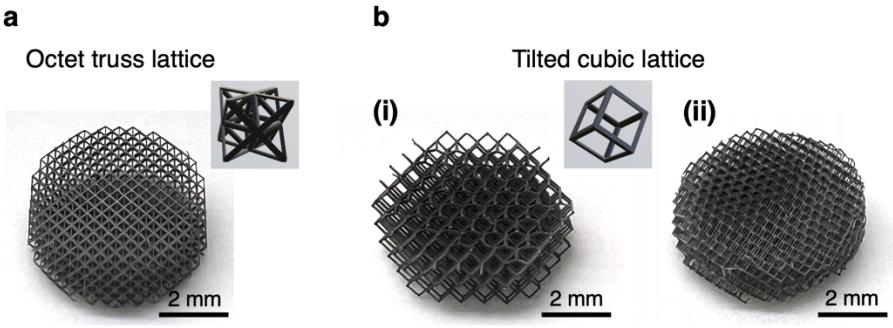

Figure 2.5 Optical images of 3D micro-architected LCO lattices with different unit cells, including a) octet truss unit cell and b) tilted cubic unit cell in varies sizes. Insets show the octet truss and tilted cubic unit cells.

2.3 Equilibrium of Ion Infusion

Infusion of metal salts into the 3D hydrogel microlattices introduces precursors for the calcination process. For LCO synthesis, the gel was immersed in aqueous solutions of lithium nitrate and cobalt nitrate. To estimate the swelling time at 80 °C for the hydrogel to reach equilibrium, identically fabricated hydrogel microlattices were immersed in solutions with Li^+ and Co^{2+} ion concentrations to be 1M, 2M and 5M for 1 day, 2 days and 5 days, and then dried in vacuum oven at 90 °C for 24 hours to remove water, leaving cross-linked PEGda polymer with lithium and cobalt nitrate salts, shown in Figure 2.6. The mass of a blank hydrogel after drying in vacuum oven is 38.1 mg, and the mass of pure polymer in all other samples were assumed to be the same. Table 2.3 summarizes the mass of all ion-infused dry samples, together with the corresponding mass and weight percentage of lithium and cobalt nitrate salts in the dry polymer. For all three concentrations of the infusion solution, the weight of dry samples swelled for 2 and 5 days are very close, but the samples swelled for only 1 day are significantly lighter, indicating the hydrogels reached equilibrium between 1 and 2 days. Therefore, in the fabrication process all samples are immersed in metal ion solutions for 2 days to ensure complete ion infusion.

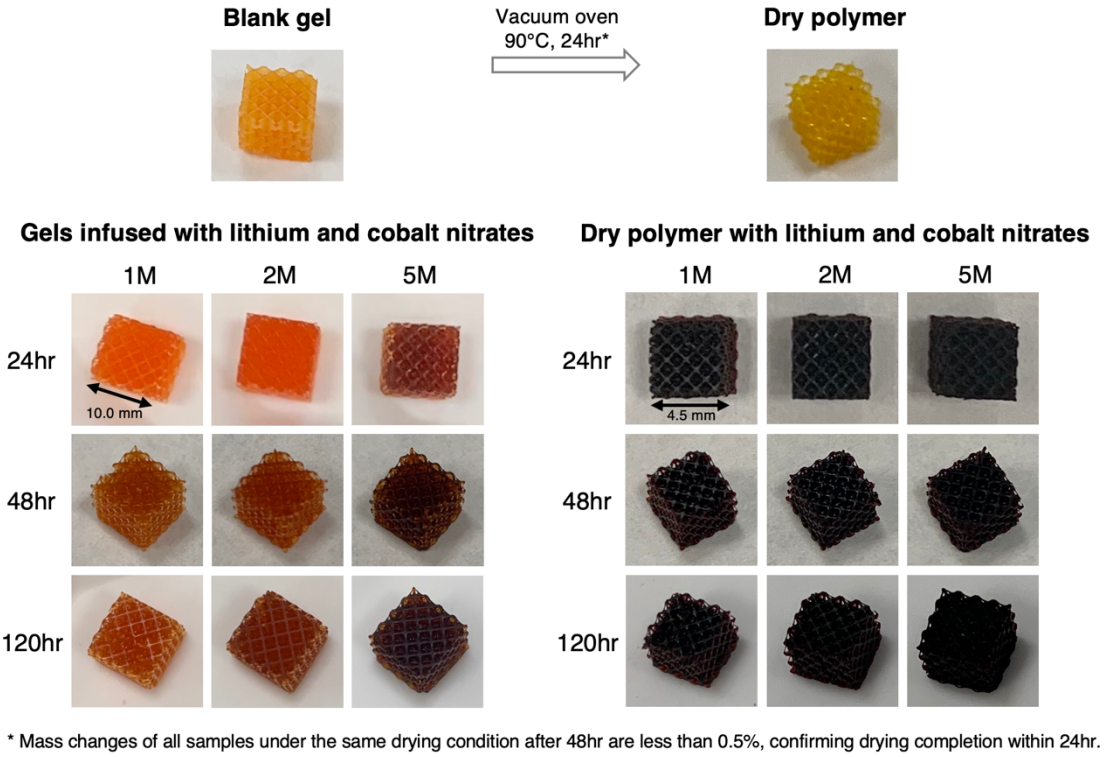

Figure 2.6 Optical images of blank and ion-infused hydrogel microlattices before and after drying in vacuum oven.

Mass of ion-infused dry polymer microlattices (mg)

	1M	**2M**	**5M**
24hr	46.1	54.1	67.9
48hr	51.2	59.5	74.0
120hr	51.3	58.5	73.7

Mass and w% of infused lithium and cobalt nitrates in dry polymer microlattices (mg)

	1M	**2M**	**5M**
24hr	8.0 (17%)	16.0 (30%)	29.8 (44%)
48hr	13.1 (26%)	21.4 (36%)	35.9 (49%)
120hr	13.2 (26%)	20.4 (35%)	35.6 (48%)

Table 2.3 Mass of ion-infused dry polymer microlattices and the corresponding mass and weight percentage of lithium and cobalt nitrates in the dry polymer.

2.4 Thermal Analysis for Calcination Process

Thermogravimetric analysis (TGA; TGA 550, TA Instruments) and differential scanning calorimetry (DSC; DSC 25, TA Instruments) analysis of the infused gel shown in Figure 2.7 reveal the endothermic dehydration followed by the exothermic decomposition and combustion reactions between polymers, metal salts and O_2 in air, which finish below 400 °C. The overall reaction is $2LiNO_3 + 2Co(NO_3)_2 + 2kC_{26}H_{46}O_{13} + (62k\text{-}7)O_2 \rightarrow 2LiCoO_2 + 52kCO_2 + 46kH_2O + 3N_2$, for which k is the molar ratio of the oligomer to Li or Co ions. The unbounded water weighs 40% of the total mass of the ion-infused gel, and the final LCO lattice retains 13% of the original mass.

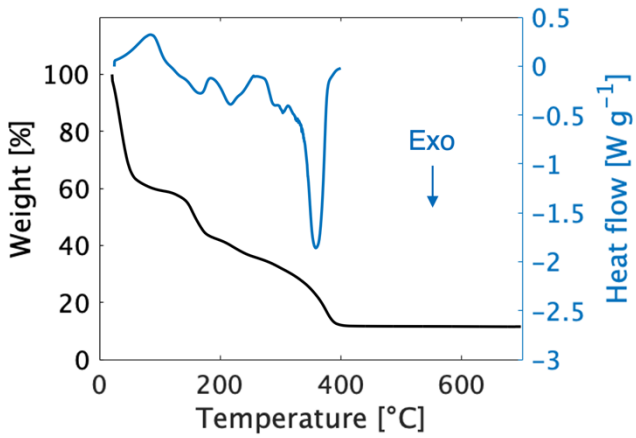

Figure 2.7 TGA and DSC profiles of hydrogel microlattices infused with lithium and cobalt nitrates, both heated in air. TGA temperature ramps at 20 °C min^{-1} from room temperature to 120 °C, followed by an isothermal hold for 60 min for complete water removal, and then ramps at 2 °C min^{-1} to 700 °C. DSC temperature ramps at 1 °C min^{-1} from 25 °C to 400 °C.

2.5 Calcination Temperature Profile and Microlattice Structural Integrity

The lithium and cobalt ion-infused hydrogel microlattices are calcined on an alumina plate inside a tube furnace (OTF-1500X, MTI) to become LCO microlattices. This calcination process consists of three steps, including the reaction to synthesize LCO under 400 °C, sintering to allow LCO grain growth, and cooling back to room temperature, as shown in Figure 2.8.

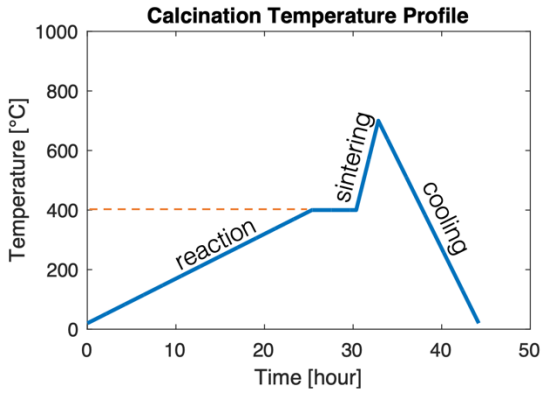

Figure 2.8 Calcination temperature profile for the synthesis of LCO microlattices from ion-infused hydrogel microlattices.

The LCO synthesis reaction takes place under reduced pressure at 0.01 atm with air flowing at 5 mL min^{-1}, using a temperature ramp at 0.25 °C min^{-1} to 400 °C followed by an isothermal hold for 5 hours. After the hold, the gas is switched to Ar which flows at 14 mL min^{-1} at 1 atm for LCO sintering, and the temperature ramps at 2 °C min^{-1} to 700 °C before cooling. Microlattices lose around 87% of their original mass due to the loss of water and the combustion of polymers during the reaction step and experience isotropic linear shrinkage of around 60%. While this significant loss of mass and volume can prevent printed geometries from surviving the thermal treatment, the challenge can be overcome by limiting the reaction rate to allow for isotropic part shrinkage throughout the entire 3D structure. The furnace tube is also connected to a rotary vane pump to reduce O_2 concentration for slower combustion. The temperature ramping rate from room temperature to 400 °C is another

deterministic parameter to control the reaction rate. Figure 2.9 shows the different calcined LCO microlattice morphologies with temperature ramping rate of 2 °C min^{-1}, 1 °C min^{-1} and 0.25 °C min^{-1}. 2 °C min^{-1} results in the complete disintegration of the entire microlattice structure due to the fast combustion and outgassing. Self-supporting LCO lattices which mainly maintained the 3D structure can be obtained with a slower rate of 1 °C min^{-1}, but broken beams are widely observed, indicating the mass loss during thermal treatment is still too fast for isotropic shrinkage. High quality LCO microlattices are obtained when the temperature ramping rate is further reduced to 0.25 °C min^{-1}, so this rate is used as the standard heating rate for the reaction step during the calcination process to fabricate micro-architected cathode materials through this gel infusion additive manufacturing technique.

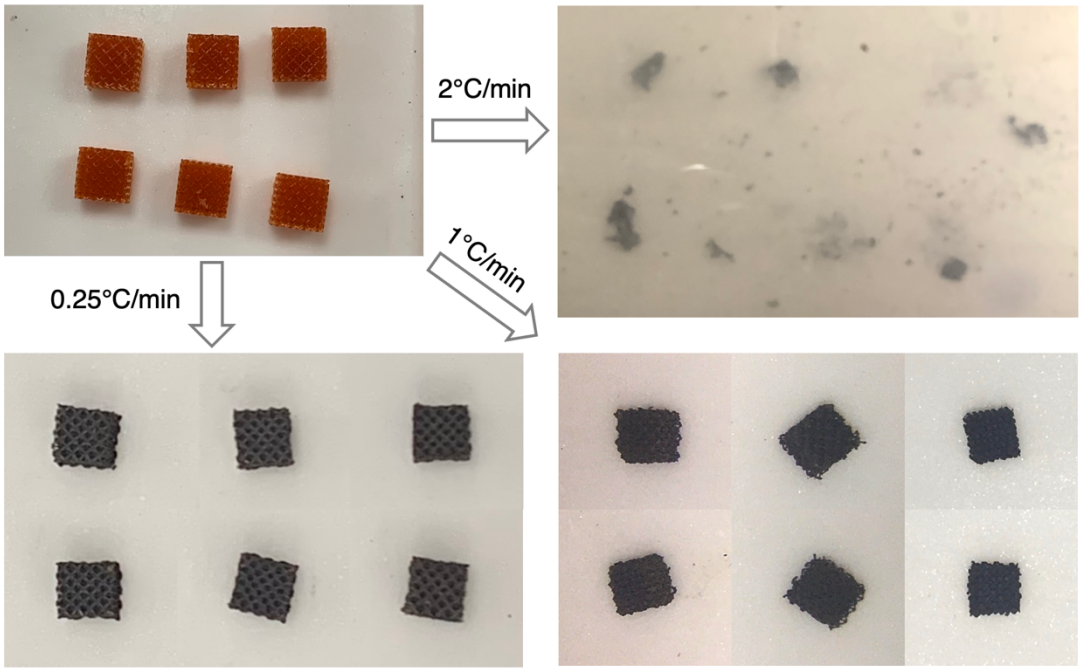

Figure 2.9 Optical images of LCO microlattices calcined from ion-infused hydrogel microlattices with different temperature ramping rates for the reaction step, including 2 °C min^{-1}, 1 °C min^{-1} and 0.25 °C min^{-1}.

2.6 Elemental Analysis and Crystal Structure

Elemental mappings from energy dispersive X-ray spectroscopy (EDS), as depicted in Figure 2.10, show a uniform distribution of cobalt, oxygen and carbon atoms on the beam of the LCO microlattice. EDS analysis was performed in SEM (Versa 3D DualBeam, Thermo Fisher) with an EDS system (Quantax 200, Bruker), using an applied voltage of 10 kV. Lithium is undetectable by this system.

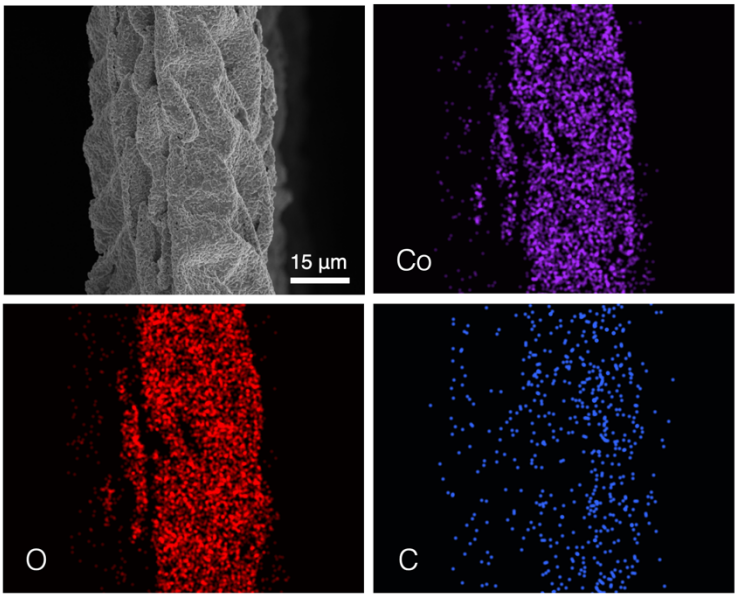

Figure 2.10 SEM image of a beam in the LCO microlattice, with EDS elemental mapping on the corresponding area.

$LiCoO_2$ as a cathode material in lithium-ion batteries should have 1:1 stoichiometric ratio between lithium and cobalt atoms when it is uncharged. Other lithium compounds may be present in the LCO microlattice as potential side products from calcination when cobalt is deficient, and cobalt compounds would occur when lithium is deficient. To quantitatively analyze the amount of lithium and cobalt atoms in the LCO microlattice and the mass percentage of residual carbon from incomplete oxidation of decomposed polymers, inductively coupled plasma mass spectroscopy (ICP-MS; 8800 Triple Quad ICP-MS, Agilent) experiments were conducted.

Figure 2.11 shows the sample and standards preparation processes for ICP-MS experiments. To prepare samples, around 25 mg of the LCO microlattice was weighed with high precision analytical balance and fully digested in about 6 mL of 70% HNO_3 at 90 °C with reflux heating for 12 hours. The overall reaction for LCO is $4LiCoO_2 + 12HNO_3 \rightarrow 4LiNO_3 + 4Co(NO_3)_2 + 6H_2O + O_2$. The obtained concentrated solution was diluted with 5% HNO_3 to 50 mL. This solution with around 50 mg sample per 50 mL was further diluted with a factor of 500 to around 0.1 mg sample per 50 mL, which is used as the final sample solution for ICP-MS analysis. Eight external standards were prepared with 1000 mg L^{-1} lithium and cobalt standard solutions for ICP through serial dilution with 5% HNO_3 into concentrations shown in Figure 2.11. The standard solution with 120 ppb Li and 1200 ppb Co, which is the closest to the sample solution, was chosen as the quality control (QC) standard, and 5% HNO_3 was used as the calibration blank. Calibration curves collected from the standards have R^2 values no less than 0.9999.

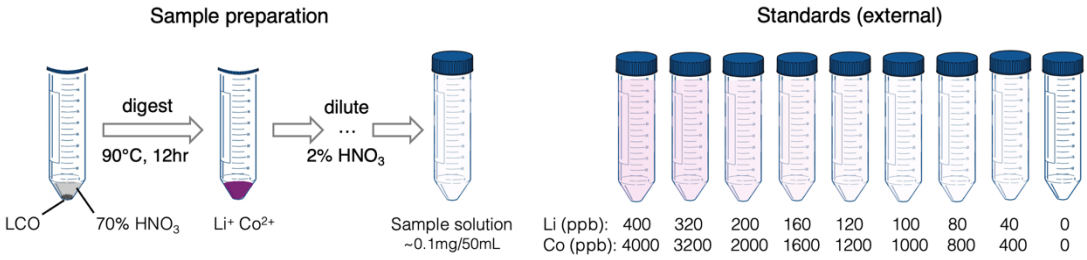

Figure 2.11 Sample preparation (left) and external standards preparation (right) processes for ICP-MS experiments on LCO microlattices.

Three sample solutions were measured for each LCO microlattice sample with two measurements for each solution, and the average lithium and cobalt ion concentrations were calculated, all with standard deviations less than 2%. The ion concentrations were then used to calculate the amount of lithium and cobalt atoms in the corresponding LCO sample. The amount of oxygen atoms was obtained by assuming charge neutrality and +3 oxidation state for Co. The mass of carbon can also be calculated, since from EDS analysis it is the only element which presents in the LCO microlattice besides lithium, cobalt and oxygen. For the

LCO microlattice sample with the standard infusion condition introduced in Chapter 2.2 and the standard calcination condition described in Chapter 2.5, ICP-MS analysis confirms a lithium to cobalt molar ratio of 1.01:1, and reveals the amount of carbon residue to be 5% in weight.

The composition of LCO microlattice samples fabricated using excess amount of lithium in the ion-infusion solution were also studied using ICP-MS. Each infusion solution has cobalt concentration of 2M, with 5%, 12%, 25% and 50% excess lithium in molarity, and the standard calcination condition introduced in Chapter 2.5 was applied. At infusion equilibrium, the higher concentration of lithium ion compared to cobalt ion in the infusion solution will lead to a similar difference in ion concentrations in the hydrogel. Figure 2.12 presents the lithium and cobalt ion calibration curves and the measured ion concentrations in sample solutions. Compositions of LCO microlattice samples are summarized in Table 2.4, showing over-stoichiometry of lithium in the synthesized sample for excess amount of infused lithium ions. In Chapter 2.8, alternative sintering conditions are discussed, where LCO microlattices may show sub-stoichiometric quantities of lithium even when infused with excess amount of lithium ions before calcination.

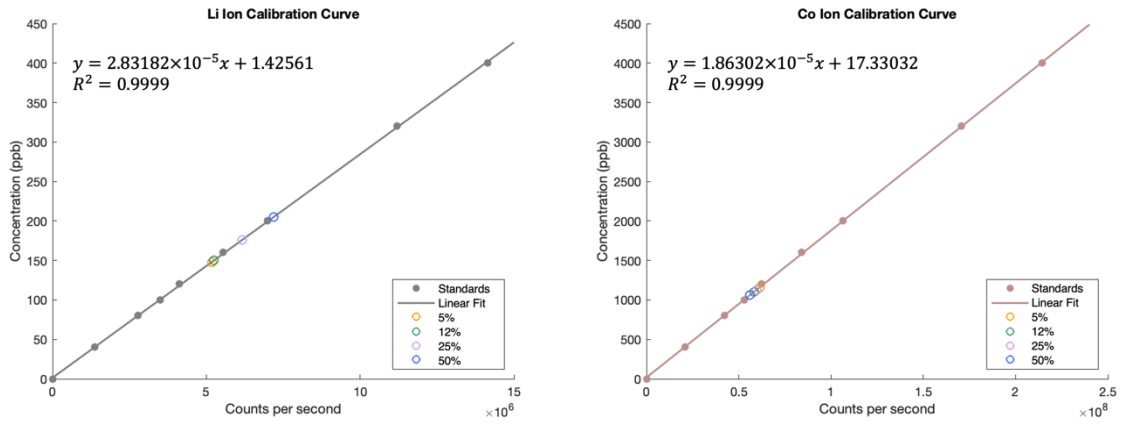

Figure 2.12 ICP-MS analysis results for LCO microlattices with excess amount of lithium. Calibration curves for lithium and cobalt ions and the measured ion concentrations for LCO microlattice samples fabricated using ion-infusion solutions with 5%, 12%, 25% and 50% excess amount of lithium in molarity.

	5% excess Li	12% excess Li	25% excess Li	50% excess Li
LCO microlattice mass (mg)	52.0	37.2	51.3	54.5
Li:Co atomic ratio	1.08:1	1.15:1	1.33:1	1.64:1
LCO stoichiometric formula	$Li_{1.08}CoO_{2.04}$	$Li_{1.15}CoO_{2.08}$	$Li_{1.33}CoO_{2.16}$	$Li_{1.64}CoO_{2.32}$

Table 2.4 The mass of LCO microlattice samples fabricated using ion-infusion solutions with 5%, 12%, 25% and 50% excess amount of lithium in molarity for ICP-MS analysis, the measured atomic ratio between lithium and cobalt atoms and the equivalent LCO stoichiometric formula.

X-ray powder diffraction (XRD) confirms the resulting crystal possesses only a single crystalline phase after the standard ion infusion and calcination conditions: the hexagonal α-$NaFeO_2$ layered structure in the trigonal $R\bar{3}m$ space group, shown in Figure 2.13 together with a reference from Inorganic Crystal Structure Database (ICSD). The data was collected using an X-ray diffractometer (SmartLab, Rigaku) with a Cu K_α source at 40 kV and 50 mA. The clear splitting of (006)/(012) and (018)/(110) peaks suggest well-layered hexagonal crystal structure.

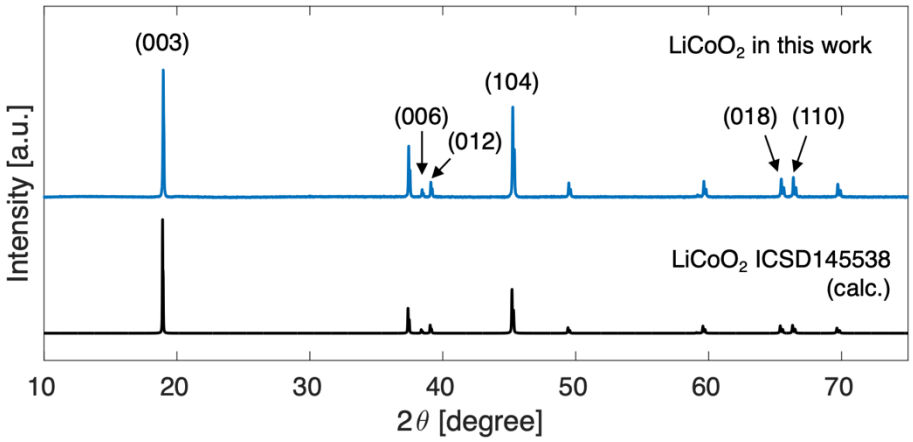

Figure 2.13 XRD pattern for the additively manufactured LCO fabricated with the standard ion-infusion and calcination conditions, and a reference from ICSD.

The residual carbon in LCO microlattices from incomplete oxidation of decomposed polymers is commonly observed at LCO grain boundaries, as shown in Figure 2.14. The carbon can be removed by a further thermal treatment of the sample in air with ambient pressure, but the 5% carbon was kept since it enhances electrical conductivity of the LCO electrode. The desired presence of carbon between LCO grains in this additively manufactured LCO mirrors the practice in conventional slurry cathodes where carbon-based materials are usually included purposefully as electron conducting additives [11].

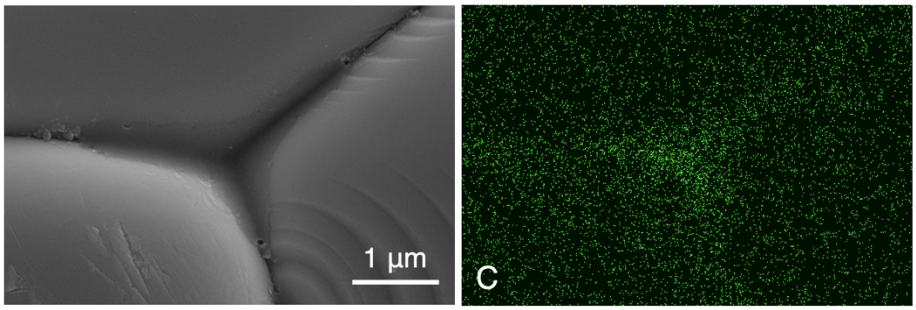

Figure 2.14 SEM image and the corresponding EDS carbon element mapping showing carbon at LCO grain boundaries, from a sample sintered up to 900 °C under 1 atm Ar.

2.7 Electrochemical Analysis

3D micro-architected LCO lattices fabricated with the standard ion infusion and calcination processes are selected as representative for electrochemical analysis. To decouple the material electrochemical properties of the additively manufactured LCO, cyclic voltammetry (CV) is performed at a scanning rate of 0.05 mV s^{-2} using a battery cycling system (BioLogic BCS-805) between 3.0 and 4.2 V on slurry electrodes fabricated from pulverized 3D LCO lattice and with a thickness of 20 μm. To make the slurry paste, 255 mg of the pulverized LCO powder was thoroughly mixed using zirconia ball milling with 15 mg of Super C65 conductive carbon black, 30 mg of polyvinylidene fluoride (PVDF) binder and 0.5 mL of *N*-methyl-2-pyrrolidone (NMP) in a plastic vial. The slurry paste was coated on a 20 μm thick sheet of aluminum foil using a micrometer film applicator (SH0335, TQC Sheen) with a 150 μm gap and then dried in a vacuum oven at 50 °C for 24 hours. An electrode film with 70 μm thick dry slurry coating was obtained and electrode disks of 9.5 mm in diameter were punched out of the film and dried in a vacuum oven at 100 °C for 24 hours. Following this, electrode disks were tested in CR2032 coin cells against Li metal, with 1M $LiPF_6$ in a 1:1 (v/v) ratio of ethylene carbonate (EC) and diethyl carbonate (DEC) liquid electrolyte. As shown in Figure 2.15, the major pair of peaks at 3.98/3.87 V correspond to the transformation of Li_xCoO_2 in the region of x = 1–0.7 through a solid state reaction process between two O3 hexagonal phases, which involves a drastic change in electronic properties [28,29]. The two pairs of peaks at 4.09/4.07 V and 4.18/4.15 V signal the distortion to a monoclinic phase near x = 0.5 and then the transformation back to an O3 hexagonal phase [30].

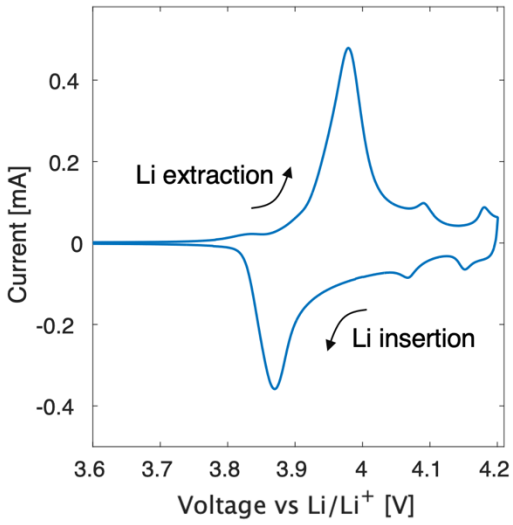

Figure 2.15 Cyclic voltammogram of a slurry electrode fabricated from pulverized LCO microlattice.

The 3D LCO lattice was assembled as a half-cell in a CR2032 coin cell against Li metal, with 1M $LiPF_6$ in 1:1 (v/v) ratio of EC/DEC liquid electrolyte. The LCO mass loading is 93 mg cm^{-2}. Compared with conventional slurry electrodes, this additively manufactured LCO electrode eliminates the polymer binders which may harm battery performance by impeding the ionic percolation while incorporating about 5% of carbon into the structure [31]. The mass of carbon is included in the reported LCO mass loading and specific capacities. The thickness of the LCO lattice is 1.80 mm. A high density polyethylene (HDPE) washer with a thickness of 1.78 mm was used to centrally position the 3D lattice and support the compressive stress from the coin cell assembly. Figure 2.16 shows the image of LCO on the aluminum foil current collector with a washer and a schematic of all coin cell components. The slightly thinner washer guarantees effective contact between the LCO lattice and the aluminum current collector (Al CC), while the LCO lattice is pre-compressed to a minor strain of 1.1%. This mechanical loading was studied using uniaxial compression experiments, as described in Chapter 2.9. Major structural failures, including layer collapse and extensive node fracturing, will not occur at this strain.

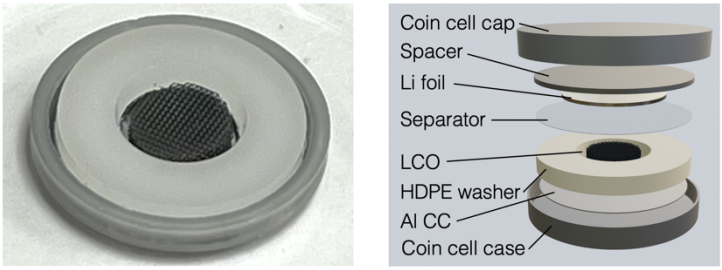

Figure 2.16 Optical image of the 3D LCO microlattice surrounded by an HDPE washer on Al CC in a CR2032 coin cell case (left) and schematic of all coin cell components (right).

Figures 2.17 and 2.18 illustrate the cycling performance of 3D LCO between 3.0 and 4.2 V at various current densities, tested using a battery cycling system (BTS4000, Neware). In Figure 2.17, the charge-discharge curves of the first two galvanostatic cycles at 3.5 mA g^{-1}, corresponding to a C-rate of C/40, give 133 and 137 mAh g^{-1} of the reversible capacity, with 82.4% and 89.9% of the Coulombic efficiency, respectively. The C-rates are calculated based on a 140 mAh g^{-1} practical capacity of LCO, which is approximately half of its theoretical capacity of 274 mAh g^{-1}. As indicated by the CV measurement, the monoclinic-hexagonal phase transformation near composition $Li_{0.5}CoO_2$ occurs at 4.2 V [30].

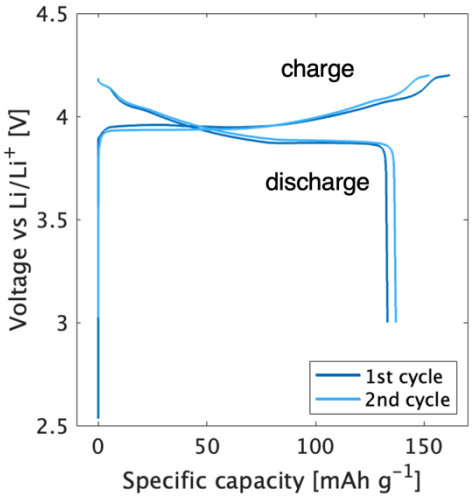

Figure 2.17 First and second charge-discharge curves from the galvanostatic cycling of the 3D LCO microlattice at C/40.

The discharge capacities and the corresponding Coulombic efficiencies at increasing C-rates from C/40 to 2C, followed by ten cycles at C/2, are summarized in Figure 2.18. C/40, C/20, C/10 and C/5 were cycled with constant current charging and discharging, giving a stable reversible capacity fluctuating in the range of 122–142 mAh g^{-1} (11.3–13.2 mAh cm^{-2}). The Coulombic efficiency gradually increases to 98.7% in the first five cycles, and remains > 99% until the current density goes above C/5. For C/2, 1C and 2C cycles, constant current constant voltage (CC-CV) charging with 0.02 mA cutoff and constant current discharging were employed. While the discharge capacity remains above 130 mAh g^{-1} during C/2, it drops abruptly to 47–64 mAh g^{-1} for 1C and 5–7 mAh g^{-1} for 2C, with Coulombic efficiencies to be 95.4%, 49.2% and 15.6% for the first cycle at each rate. The capacity immediately recovers to 125 mAh g^{-1} upon returning to C/2, and then a gradual capacity fade to 115 mAh g^{-1} occurs over the next five cycles, followed by an abrupt drop to 62 mAh g^{-1} in five more cycles.

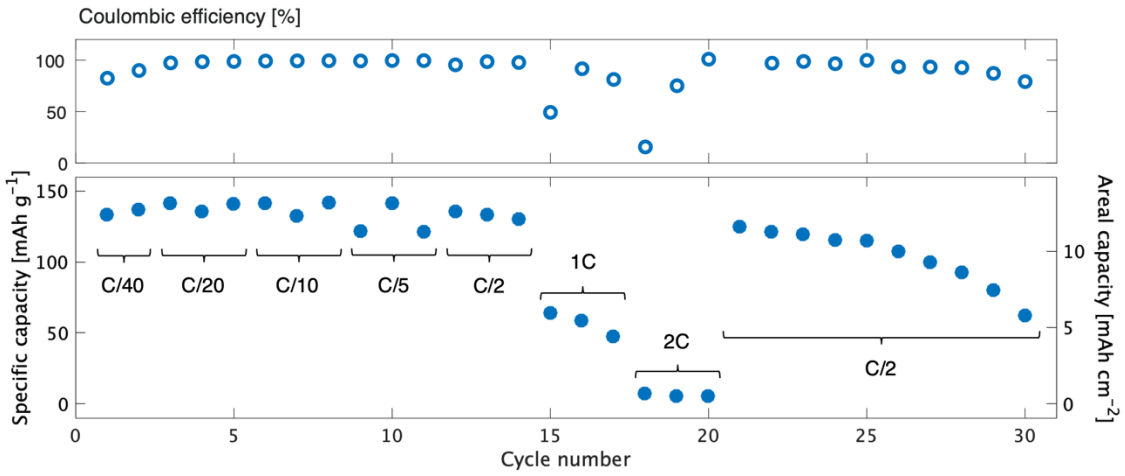

Figure 2.18 Coulombic efficiency (top) and discharge specific and areal capacities (bottom) of the 3D LCO lattice cycled between 3.0 and 4.2 V at different C-rates.

During cycling, Li is plated and stripped on and from the Li metal foil only in the area not covered by the HDPE washer, as shown in Figure 2.19. Therefore, at a rate of 2C for LCO cathode, the effective areal current density for the Li metal anode is around 10.7 mA cm^{-2},

which can rapidly lead to mossy Li surface morphology, deteriorating the full cell performance [32]. Using a high-rate anode to match the high areal capacity of the LCO 3D microlattice may further enhance the long-term cycling performance of the full cell [33].

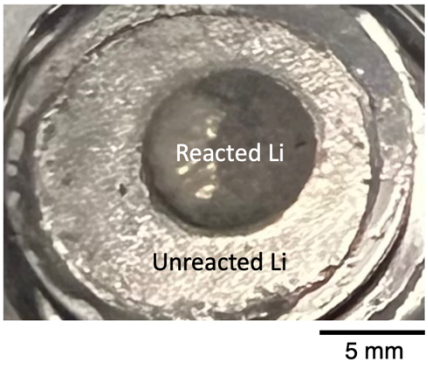

Figure 2.19 Optical image of Li metal anode after full cell cycling.

The freestanding 3D LCO electrode fabricated with our gel infusion additive manufacturing technique eliminates the polymer binder and largely improves the mass loading of active materials on the current collector. To demonstrate the significant difference in active material mass loading, the specific discharge capacity at multiple C-rates for a 3D interdigitated LCO electrode was compared to a commercial LCO slurry electrode, shown in Figure 2.20. The 3D electrode consisted of beams with 100 μm in diameter, and its detailed structure is presented in Chapter 4.2. The mass of each component in both slurry and 3D electrode is summarized in Table 2.5. With comparable capacities at low rates, the active material mass percentage in the overall electrode is 1.4 times higher in the 3D electrode (88%) than in the slurry electrode (62%). The relatively poor performance of the 3D electrode at C/5 is a result of the thick beams in the 3D structure. If the beam diameter is reduced from 100 μm to 45 μm, significantly better performance at C/5 should be achieved, as demonstrated by the specific discharge capacity of LCO microlattices shown in Figure 2.18.

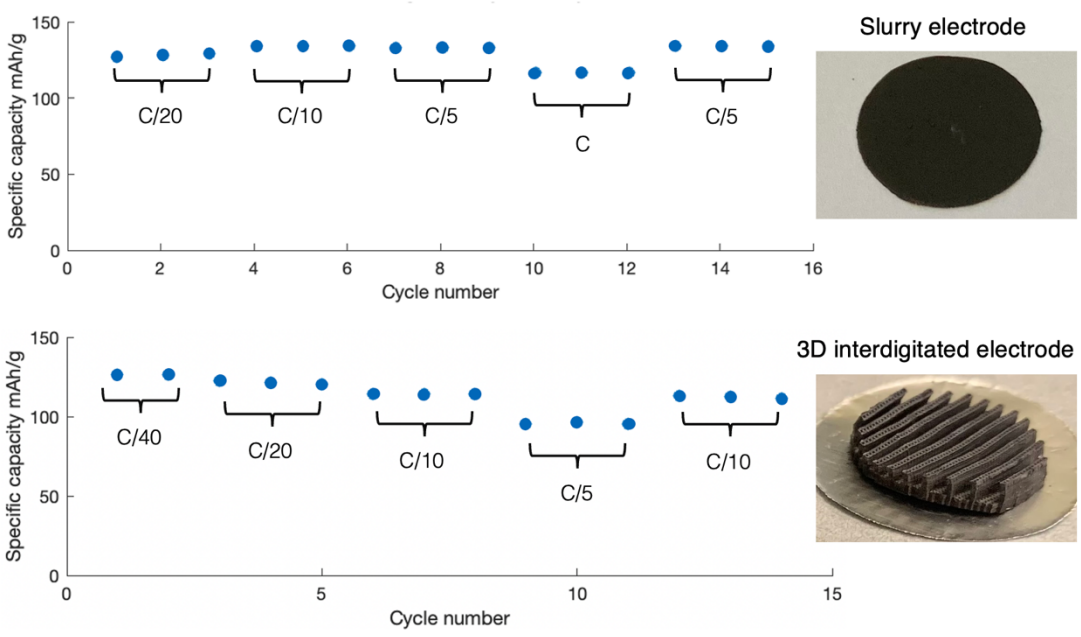

Figure 2.20 Discharge specific capacities of a slurry electrode fabricated with commercial LCO powder and an LCO interdigitated electrode fabricated with the gel infusion additive manufacturing technique, both cycled between 3.0 and 4.2 V at different C-rates.

	Slurry electrode	**3D electrode**
Mass of slurry coating (47 µm) or 3D electrode (mg)	10.28	89.76
Mass of Al current collector (20 µm) (mg)	3.80	3.80
Mass of carbon (mg)	0.51 (5%)	4.49 (5%)
Mass of PVDF (mg)	1.03 (10%)	0
Mass of LCO active material (mg)	8.75	85.27
Mass of overall electrode (Al + carbon + PVDF + LCO) (mg)	14.08	97.36
Mass percentage of LCO in the overall electrode	**62%**	**88%**

Table 2.5 Mass of components in the commercial LCO slurry electrode and the 3D interdigitated LCO electrode fabricated using gel infusion additive manufacturing technique.

The beam diameter of the 3D micro-architected LCO lattice in this work was minimized down to 45 µm within the fabrication limitations, to reduce the Li ion diffusion path within

the electrode. With 45 μm beams, we observed significantly improved discharge capacities at C/5 compared to the previous work by Yee et al., which reported 94 mAh g^{-1} for LCO cubic microlattices with 100 μm beam diameters [26]. The potential for further reducing the beam size for improving capacities at higher rates than C/5 needs to be balanced against the potential trade-off with mechanical strength and electrical conductivity. Enhancing the electrical conductivity could involve optimizing the gas composition, pressure and flow rate for LCO synthesis and sintering processes to increase carbon content in the final structure. Our choice of an octet truss lattice consisting of beams with high aspect ratio of ~5.8 demonstrates the capability of this AM technique to create 3D architected electrode materials with intricate geometries. For battery electrode applications, future designs should aim for 3D structures with higher relative densities but similar minimum feature size, which could give higher areal and volumetric energy densities and potentially further enhance the overall mechanical strength of the electrode.

2.8 Microstructural Tailoring with Various Sintering Conditions

In addition to sufficient electrochemical performance, the 3D micro-architected LCO lattices need to be mechanically strong to survive sample handling during cell assembly. Since LCO is the constituent material of the microlattice, for samples with the same architecture, the overall mechanical strength is tunable by tailoring LCO microstructure. Chapter 2.8 introduces 3D micro-architected LCO lattices with several different LCO microstructures obtained from various sintering conditions, and Chapter 2.9 probes the mechanical strength and different failure mechanisms of these LCO microlattices.

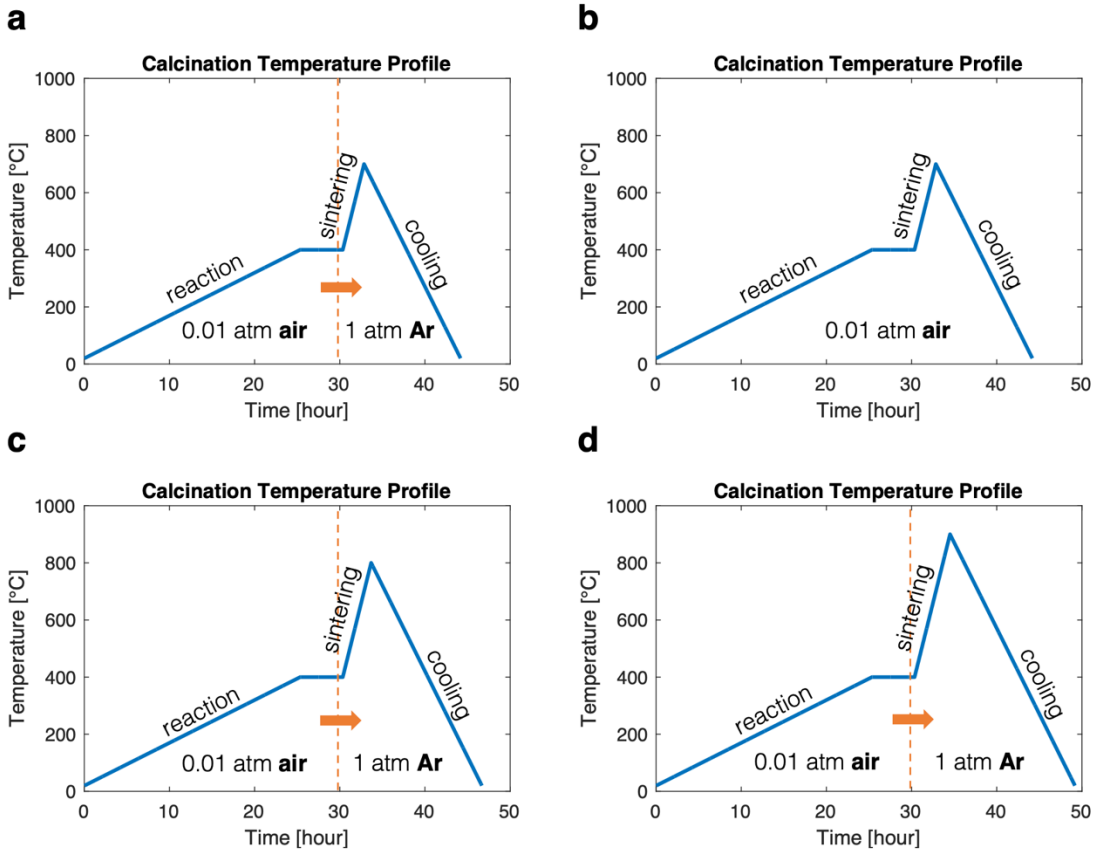

Figure 2.21 LCO calcination temperature profiles with different sintering pressures and gas species: a) under 1 atm Ar up to 700 °C; b) under 0.01 atm air up to 700 °C; c) under 1 atm Ar up to 800 °C; d) under 1 atm Ar up to 900 °C.

The rate-limited combustion of the infused gel under air with reduced pressure produces porous, nanocrystalline LCO, distributed uniformly across the 3D structure. Sintering under the standard condition, with 1 atm Ar up to 700 °C (Figure 2.21a), results in a final grain size of ~500 nm for the LCO, as illustrated in the ion channeling contrast image in Figure 2.22a, taken with gallium focused ion beam (FIB), and the SEM image of the electrode surface in Figure 2.23a. The LCO microlattice overall undergoes isotropic linear shrinkage to 40% of the printed gel, and the porosity of LCO in the microlattice is approximately 24%, estimated with the cross-section area shown in Figure 2.24a.

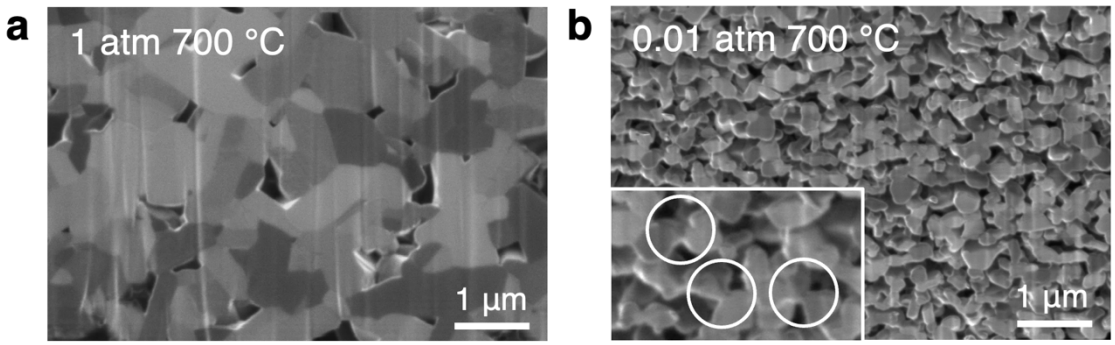

Figure 2.22 Ion channeling contrast images taken with gallium focused ion beam over the cross-sections of 3D micro-architected LCO sintered under a) 1 atm Ar up to 700 °C and b) 0.01 atm air up to 700 °C, with necking between LCO particles in the latter highlighted in the inset.

To tailor the microstructure of additively manufactured LCO, we explored different atmospheres and temperatures during the sintering stage, while keeping the same conditions during LCO synthesis below 400 °C. When the atmosphere of air under reduced pressure at 0.01 atm is maintained during sintering (Figure 2.21b), similar to Yee et al.'s method for their 3D printed hydrogels, the LCO microlattice experiences isotropic linear shrinkage to 53% of the original gel size, leading to smaller grain sizes of ~100 nm (Figure 2.22b, Figure 2.23b) and increased porosity of 33%, estimated with the four cross-section areas shown in Figure 2.24b, compared to the samples fabricated with the standard sintering condition [26]. Figure 2.25 compares the size of LCO microlattices fabricated with different sintering conditions. This reduced shrinkage in the overall dimensions of 3D lattices is due to the lower degree of

material densification and higher LCO porosity. The LCO particles exhibit more rounded geometries, more free surfaces and fewer grain boundaries, with connections between particles through necking commonly observed, as depicted in the inset of Figure 2.22b.

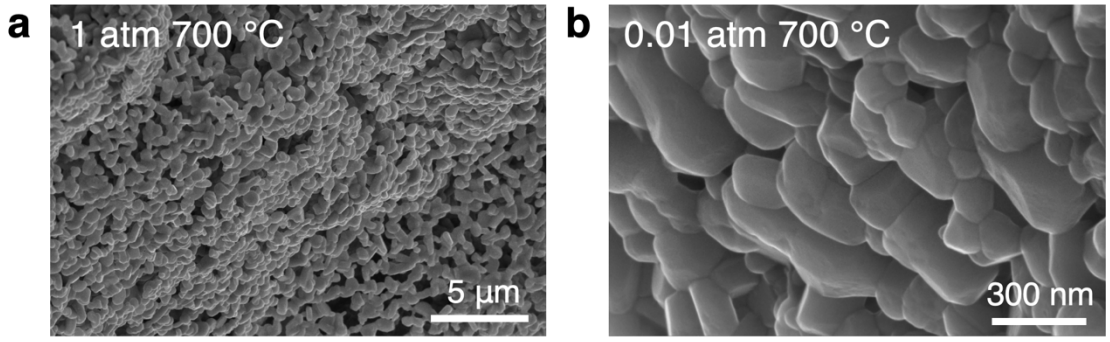

Figure 2.23 SEM images of surfaces of 3D micro-architected LCO sintered under a) 1 atm Ar up to 700 °C and b) 0.01 atm air up to 700 °C.

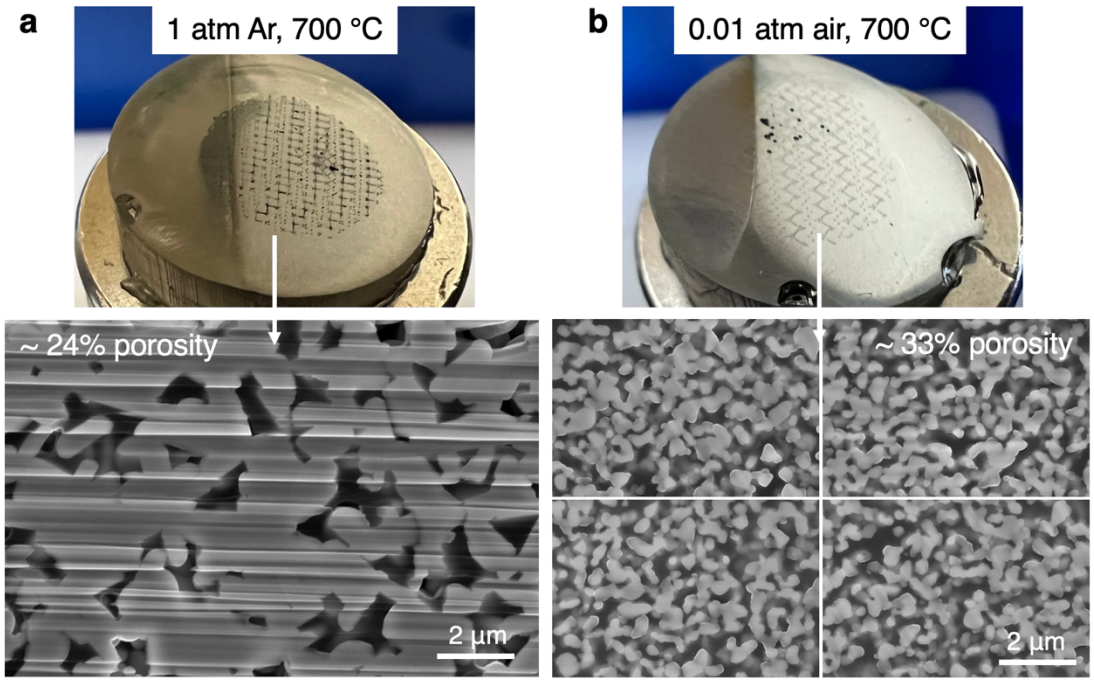

Figure 2.24 Optical images of 3D micro-architected LCO lattices mounted in epoxy and after progressive polishing to a 50 nm grit suspension, and the corresponding SEM images of the cross-sections after mechanical and FIB polishing for samples sintered a) under 1 atm Ar up to 700 °C and

b) under 0.01 atm air up to 700 °C. The thorough penetration of epoxy into the porous volume within LCO indicates interconnected pore spaces, allowing for the flow of electrolytes.

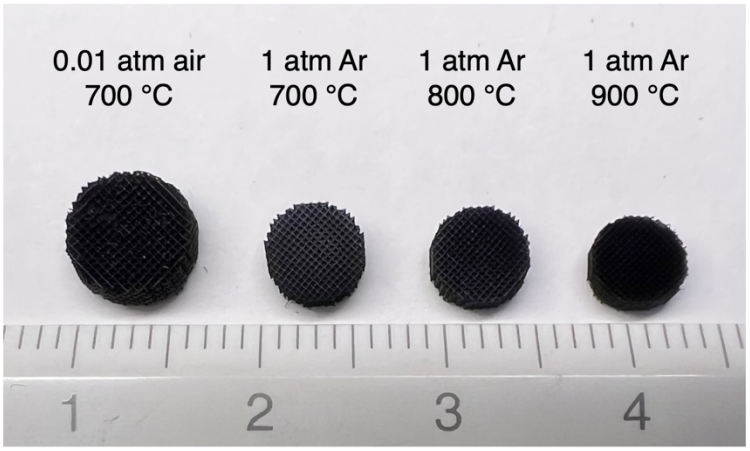

Figure 2.25 Optical image of 3D micro-architected LCO lattices sintered under different atmospheres up to various maximum temperatures.

We also explored the impact of sintering temperature on the microstructure of this additively manufactured LCO. The melting temperature of LCO is around 1100 °C [34]. Sintering at 700 °C, 800 °C and 900 °C, corresponding to approximately 0.6, 0.7 and 0.8 of its melting point, ensures it in the solid phase during the process, in line with standard practices in solid-state sintering where the material is typically heated to 0.5–0.9 of its melting point [35]. 800 °C (Figure 2.21c) and 900 °C (Figure 2.21d) sintering under 1 atm Ar results in LCO grain sizes of ~2 μm and ~4 μm, respectively, as shown in the images of sample cross-sections in Figure 2.26 and sample surfaces in Figure 2.27.

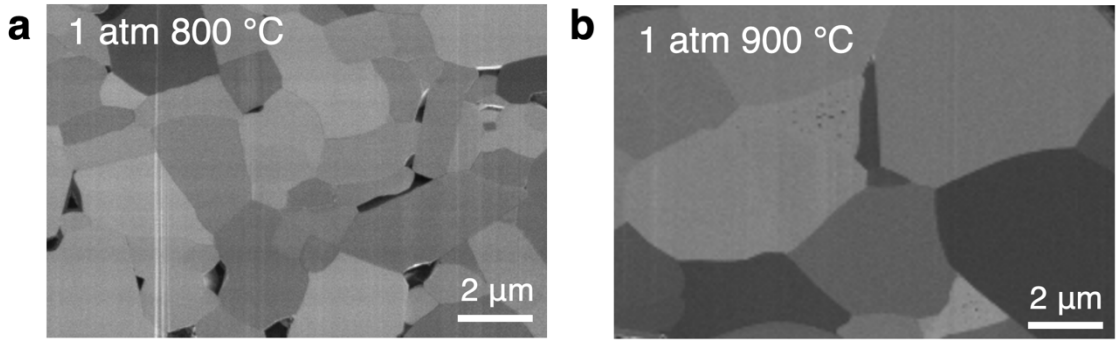

Figure 2.26 Ion channeling contrast images taken with gallium focused ion beam over the cross-sections of 3D micro-architected LCO sintered under 1 atm Ar up to a) 800 °C and b) 900 °C.

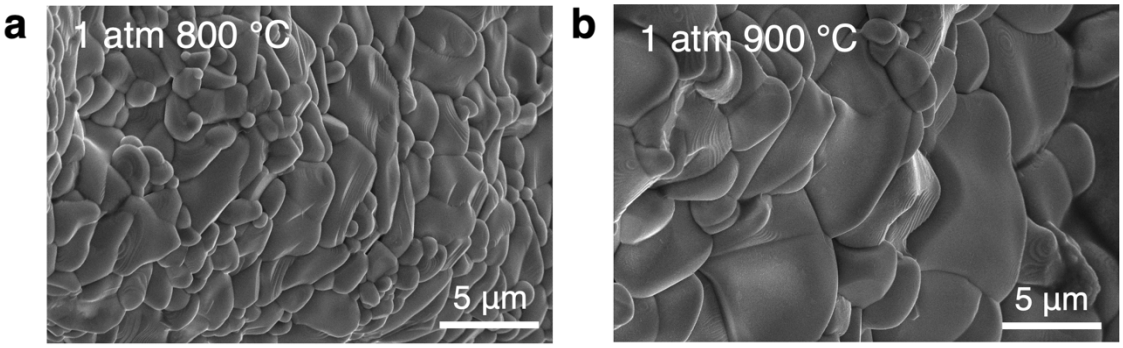

Figure 2.27 SEM images of surfaces of 3D micro-architected LCO sintered under 1 atm Ar up to a) 800 °C and b) 900 °C.

Figure 2.28 shows the XRD patterns for LCO microlattices sintered under various conditions, indicating pure LCO in the samples sintered under 1 atm Ar up to 700 °C, 0.01 atm air up to 700 °C and 1 atm Ar up to 800 °C. A small CoO peak is present in the sample sintered under 1 atm Ar up to 900 °C. An interesting finding emerged when sintering was performed at 900 °C under 0.01 atm air, with the temperature profile in Figure 2.29b. Both CoO and Co_3O_4 phases as side products from calcination occur in the synthesized LCO microlattice, indicated by its XRD pattern.

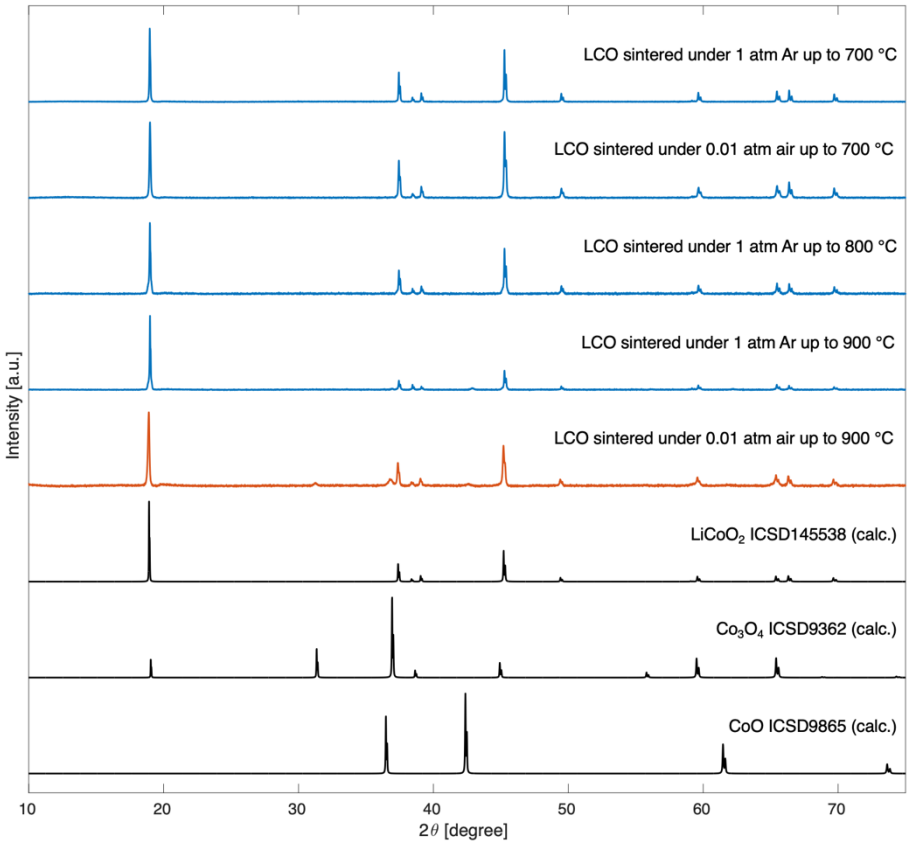

Figure 2.28 XRD patterns for the additively manufactured LCO sintered under different pressures and gas species up to various maximum temperatures, with references from ICSD.

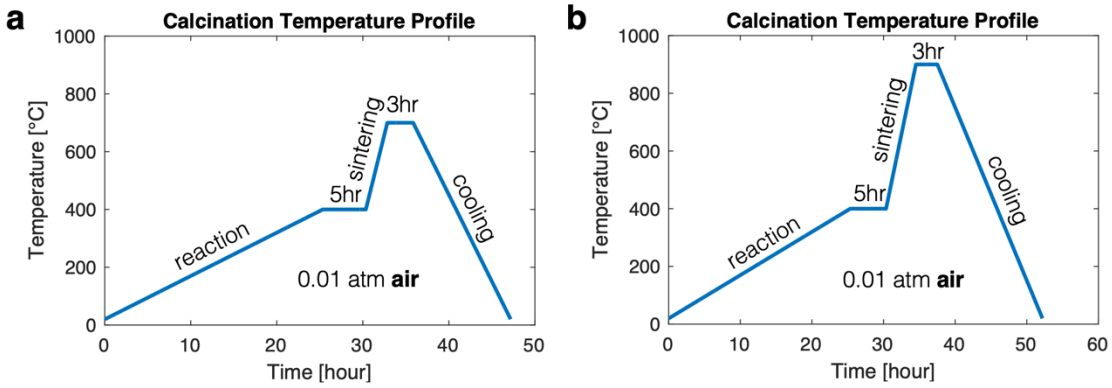

Figure 2.29 LCO calcination temperature profiles for samples sintered under 0.01 atm air up to a) 700 °C and b) 900 °C, with an additional isothermal hold for 3 hours at the peak temperature.

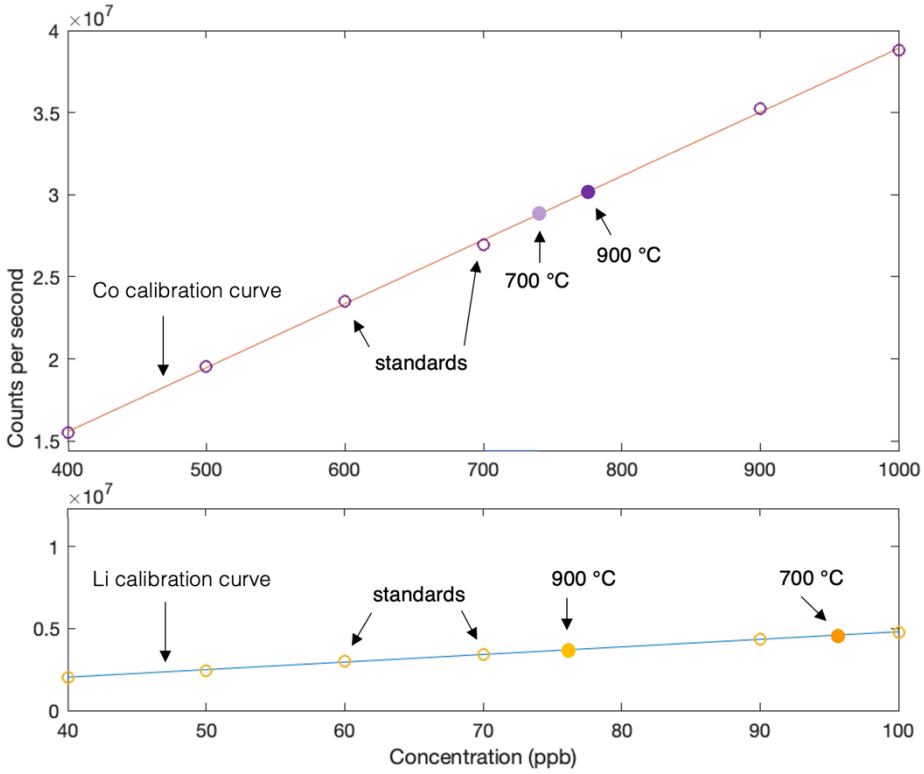

Figure 2.30 Lithium and cobalt ion calibration curves from ICP-MS analysis, and the measured ion concentrations for LCO microlattice samples sintered under 0.01 atm air up to 700 °C and 900 °C, with an additional isothermal hold for 3 hours at the peak temperature.

To investigate whether the presence of CoO and Co_3O_4 phases in the sample sintered under 0.01 atm air up to 900 °C is attributed to a substantial loss of lithium during high temperature sintering under reduced pressure, ICP-MS experiments were conducted for this sample. For comparison, a sample sintered under the same pressure and gas species, and with a similar temperature profile except for a peak temperature of 700 °C (Figure 2.29a) was also analyzed. Figure 2.30 presents the lithium and cobalt ion calibration curves and the measured ion concentrations in sample solutions. Compositions of LCO microlattice samples are summarized in Table 2.6, showing significant lithium deficient, with a lithium to cobalt molar ratio of 0.75:1, in the sample sintered under 0.01 atm air up to 900 °C. An exact 1:1 molar ratio between lithium and cobalt atoms in the sample sintered only up to 700 °C indicates the significant loss of lithium occurs between 700 °C and 900 °C for sintering under

reduced pressure. These results suggest that, unlike in this work, the sintering process introduced by Yee et al. cannot be straightforwardly generalized into higher peak temperatures for LCO grain size tailoring without changing the atmosphere [26].

	700 °C	**900 °C**
Li:Co atomic ratio	1.00:1	0.75:1

Table 2.6 The atomic ratio between lithium and cobalt atoms measured from ICP-MS analysis for LCO microlattice samples sintered under 0.01 atm air up to 700 °C and 900 °C, with an additional isothermal hold for 3 hours at the peak temperature.

In Chapter 2.6, the composition of LCO microlattices fabricated using excess amount of lithium in the ion infusion solution and with the standard calcination conditions were studied using ICP-MS, which demonstrates over-stoichiometry of lithium in the synthesized sample for excess amount of infused lithium ions. 5%, 12%, 25% and 50% excess lithium results in LCO microlattices with lithium to cobalt atomic ratios of 1.08:1, 1.15:1, 1.33:1 and 1.64:1, respectively. Here, to investigate whether the excess amount of lithium in the ion infusion solution is able to compensate for the significant loss of lithium when sintered under reduced pressure at high temperature, we fabricated LCO microlattices using ion infusion solutions with 5%, 10%, 15%, 20% and 25% excess amount of lithium in molarity, all sintered under 0.01 atm air up to 900 °C following the process in Figure 2.29b. However, from XRD patterns for all these samples shown in Figure 2.31, there are still significant peak intensities for CoO and Co_3O_4 phases, even for the one with the highest amount of infused lithium ions, which indicates the LCO microlattices still suffer from severe under-stoichiometry of lithium.

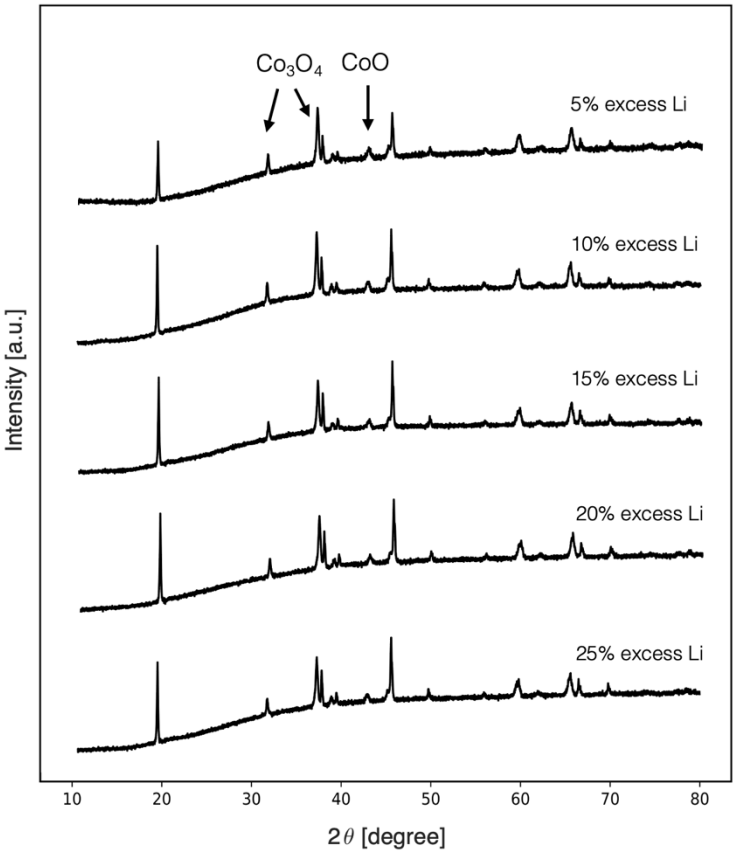

Figure 2.31 XRD patterns for the additively manufactured LCO samples fabricated using ion-infusion solutions with 5%, 10%, 15%, 20% and 25% excess amount of lithium in molarity, all sintered under 0.01 atm air up to 900 °C, with an additional isothermal hold for 3 hours at the peak temperature.

When the sintering atmosphere is switched to 1 atm Ar as in the standard sintering condition, the additional 3-hour isothermal hold at 900 °C (Figure 2.32) allows for more extensive grain growth and results in even larger LCO grains with rounded shape compared to the LCO microlattices sintered without the high-temperature hold. Figure 2.33a presents a top-view SEM image of the LCO microlattice sintered under this condition, with a closer view of an individual beam shown in Figure 2.33b and a highlight of a representative LCO grain on the surface of the microlattice shown in Figure 2.33d. The beam cross-section in the SEM image in Figure 2.33c was imaged with gallium focused ion beam, giving the ion channeling

contrast image in Figure 2.33e, which shows only two LCO grains in this cross-section area as highlighted in Figure 2.33f.

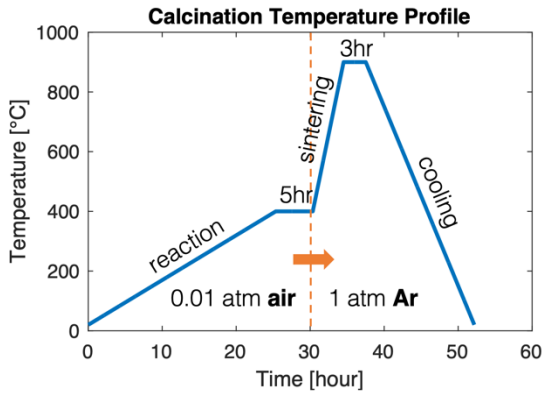

Figure 2.32 LCO calcination temperature profile for samples sintered under 1 atm Ar up to 900 °C, with an additional isothermal hold for 3 hours at the peak temperature.

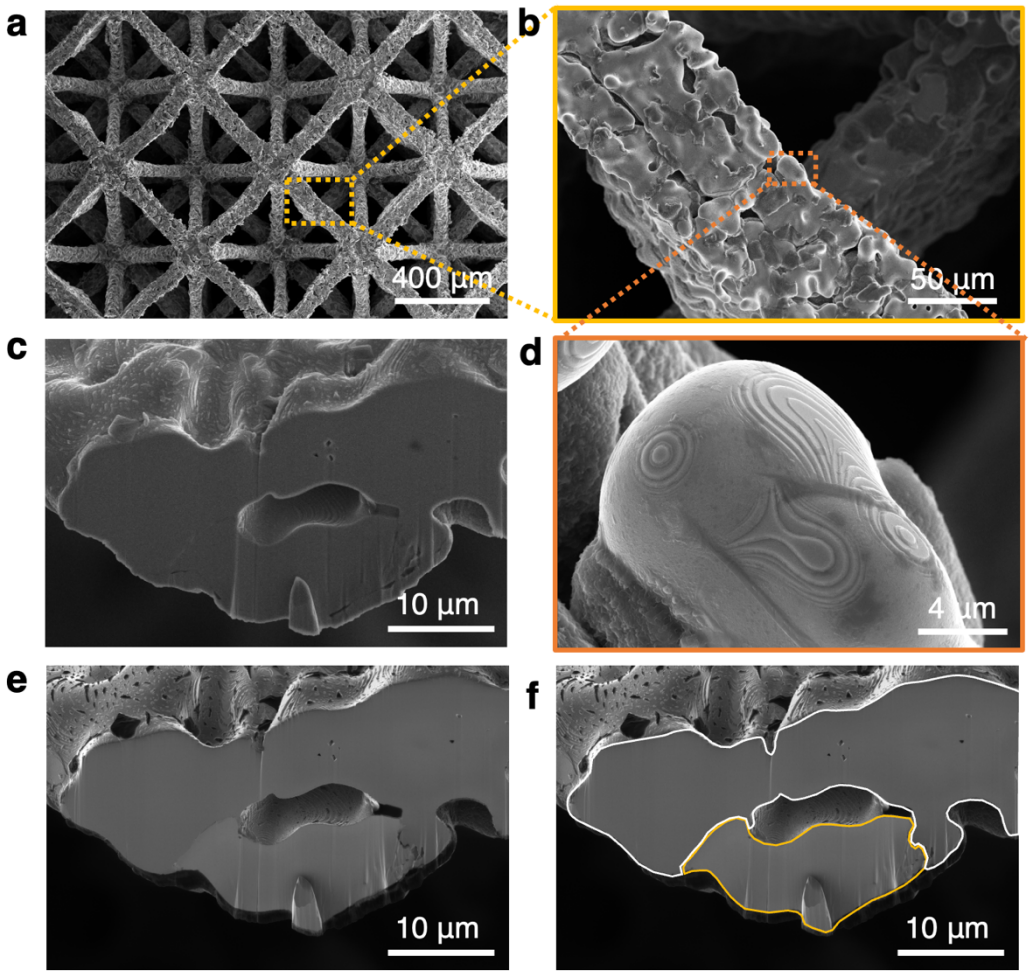

Figure 2.33 3D micro-architected LCO lattice sintered under 1 atm Ar up to 900 °C, with an additional isothermal hold for 3 hours at the peak temperature. a) SEM image of a microlattice from top-view. b) SEM image of a beam in this lattice. c) SEM image of the cross-section of a beam. d) SEM image of an LCO grain on the surface of the sample. e) Ion channeling contrast image taken with gallium FIB over the cross-section. f) Highlight of the two LCO grains in the cross-section area.

Following the sintering condition in Figure 2.32, excess amount of lithium ions in the infusion solutions again results in over-stoichiometry of lithium in the synthesized LCO microlattices, with ICP-MS analysis results summarized in Table 2.7 and their corresponding XRD patterns shown in Figure 2.34. This result confirms that for a peak temperature of 900 °C, the sintering atmosphere of air with reduced pressure in the process shown in Figure 2.29b is a key factor to cause significant loss of lithium. When the sintering atmosphere is 1

atm Ar as in the standard sintering condition, the additional 3-hour isothermal hold at 900 °C does not lead to severe lithium loss.

	5% excess Li	8% excess Li	10% excess Li	12% excess Li	15% excess Li	18% excess Li
Li:Co atomic ratio	1.01:1	1.02:1	1.03:1	1.06:1	1.11:1	1.16:1
Carbon mass percentage (%)	7.6	2.0	7.9	8.5	6.1	10.2

Table 2.7 The atomic ratio between lithium and cobalt atoms measured from ICP-MS analysis for LCO microlattice samples sintered under 1 atm Ar up to 900 °C with an additional isothermal hold for 3 hours at the peak temperature, and the calculated carbon mass percentage in each sample.

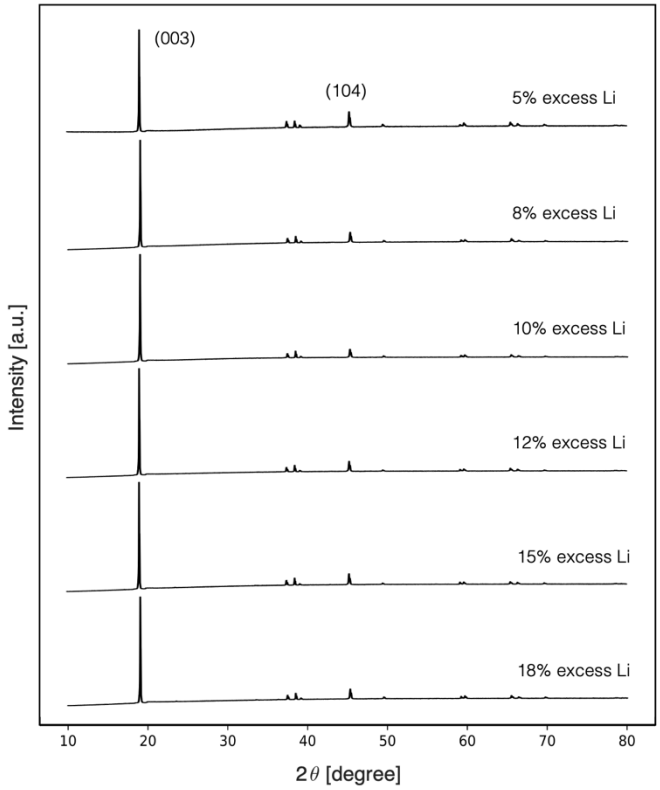

Figure 2.34 XRD patterns for the additively manufactured LCO samples fabricated using ion-infusion solutions with 5%, 8%, 10%, 12%, 15% and 18% excess amount of lithium in molarity, all sintered under 1 atm Ar up to 900 °C, with an additional isothermal hold for 3 hours at the peak temperature.

2.9 Mechanical Behaviors of 3D Micro-Architected Lithium Cobalt Oxide Lattice

The various microstructures of LCO, resulting from different sintering atmospheres, lead to distinct mechanical strengths in the 3D architected microlattices. To investigate their mechanical behaviors, uniaxial compression experiments at a quasistatic strain rate of 10^{-3} s^{-1} are performed, using a dynamic mechanical analyzer (DMA 850, TA Instruments) with a 15 mm diameter compression clamp, shown in Figure 2.35a.

Figure 2.35b shows the typical engineering stress-strain signatures of samples sintered up to 700 °C under different pressures following the conditions in Figures 2.21a and 2.21b, normalized to the overall dimensions of each microlattice. These profiles indicate the 3D architected LCO sintered under 0.01 atm exhibits over ten times weaker mechanical strength compared to the one sintered at 1 atm. The disparity in strength can be attributed to the larger number of free surface-grain boundary junctions in the 0.01 atm sintered sample, which are the weak points with concentrated stress facilitating fracture initiation and propagation [36]. Additionally, the irregular geometries of grains in the 1 atm sample, as shown in Figure 2.22a, contribute to frictional interlocking, which can further reinforce the structural integrity of LCO microlattice.

Quasistatic uniaxial compression experiments are also performed on the samples sintered up to 800 °C and 900 °C under 1 atm Ar following the conditions in Figures 2.21c and 2.21d. Similar mechanical strengths across samples were observed, as shown in Figure 2.35. Their mechanical strengths are also in a similar range as the previous sample sintered up to 700 °C under 1 atm Ar. From the investigation on the impact of sintering temperature on the microstructure of the LCO microlattices in Chapter 2.8, we have observed significant difference in the LCO grain size from 700 °C (~500 nm), 800 °C (~2 μm) and 900 °C (~4 μm) sintering. The quasistatic uniaxial compression results reveal that the grain size variation in the additively manufactured LCO within the studied range in this work is not the most important factor contributing to the overall mechanical strengths of LCO microlattices, and highlight the significant contribution of different sintering atmospheres.

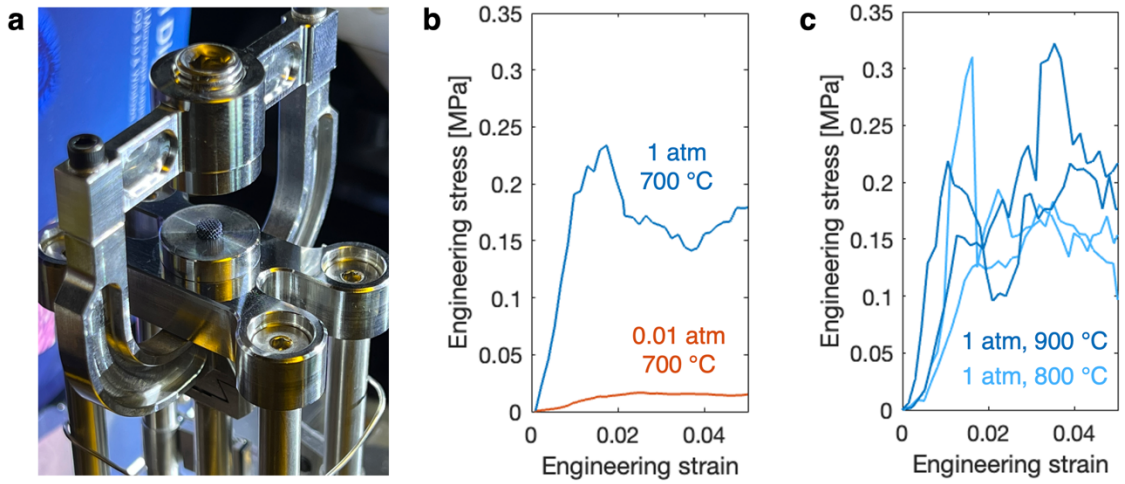

Figure 2.35 Quasistatic uniaxial compression on LCO microlattices. a) Experimental setup in the dynamic mechanical analyzer with a 15 mm diameter compression clamp. b) Engineering stress-strain curves of 3D micro-architected LCO sintered under 1 atm Ar and 0.01 atm air up to 700 °C. c) Engineering stress-strain curves of 3D micro-architected LCO sintered under 1 atm Ar up to 800 °C and 900 °C.

Figure 2.36 compares two characteristic engineering stress-strain curves up to 25% effective strain of 3D LCO lattices, paired with corresponding video frames captured at multiple strains. It reveals different failure mechanisms for samples with distinct mechanical strengths, corresponding to the two different sintering pressures. The sample sintered at 0.01 atm starts fracturing at multiple nodes on the bottom of the lattice, when the stress is below 0.01 MPa. Full contact is established near 0.5% strain, and the lattice sustains a stress around 0.02 MPa after 2% strain. Beyond 12% strain, densification due to beam collapse becomes significant, and the stress keeps increasing afterwards, reaching 0.04 MPa at 24% strain. In contrast, the sample sintered at 1 atm up to 900 °C attains full contact at about 0.5% strain, followed by elastic deformation up to 0.15 MPa. The slope gives an effective elastic modulus of 19.03 MPa. After several initial fracture events, the stress goes up to 0.32 MPa before a major lattice collapse around 3.5% strain. Throughout compression, multiple layer collapses occur, corresponding to the rapid stress drops on the curve. A notable instance is captured on the video frame at 12% strain. Random node fracturing, similar to the 0.01 atm sample, is

also present in the 1 atm sample, but the overall lattice maintains better structural integrity, as illustrated in the video frame at 24% strain.

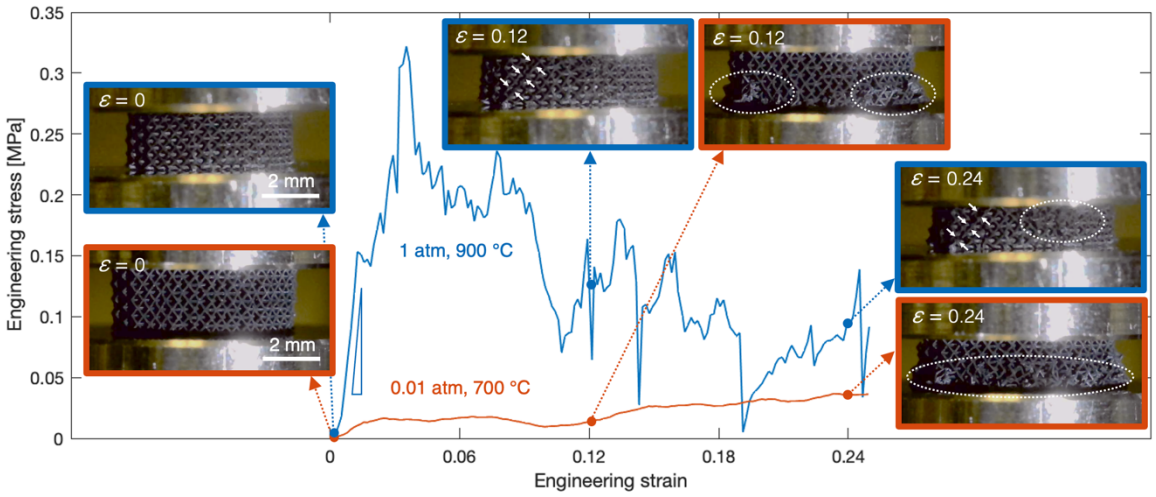

Figure 2.36 Failure mechanisms of LCO microlattices. Engineering stress-strain curves of 3D micro-architected LCO sintered under 1 atm Ar up to 900 °C and 0.01 atm air up to 700 °C, with side-view images captured at multiple strains. The triangle guides the slope of the elastic loading.

For the sample sintered at the reduced pressure, the early node fracturing before the establishment of full contact is likely due to the imperfect initial contact, as a result of structural imperfections from fabrication. The global uniaxial stress is concentrated at nodes with defects on the bottom of the lattice when individual local fractures are ready to occur. Similar structural imperfections are also present on the sample sintered at 1 atm, which does not achieve full contact until 0.5% strain as well. But in this sample, LCO, as the constituent material for the octet truss lattice, exhibits much higher mechanical resilience. Its 3D structure remains intact under the local stress concentrated at nodes with defects, while allowing the global stress to distribute across the whole lattice before layer collapses take place at much higher uniaxial stress.

2.10 Nanomechanical Analysis of Additively Manufactured Lithium Cobalt Oxide

After mechanical analysis of the 3D architected LCO lattice at macro-scale, we then zoomed into its constituent material at nano-scale by looking at the LCO grains and grain boundaries. There have been nanoindentation studies showing grain boundary softening for sintered ceramic grains due to low cohesive energy, where a significant reduction of elastic modulus has been measured at the grain boundary compared to the values measured on the grains [37]. Therefore, it will be interesting to see, whether our additively manufactured LCO, sintered at 1 atm, has this grain boundary softening effect.

To probe elastic and plastic properties of the additively manufactured LCO grains, we conducted SEM-based in situ nanoindentation experiments on 3D LCO lattice sintered up to 900 °C under 1 atm Ar following the condition in Figure 2.21d. The LCO lattice was mounted in epoxy (FibreGlast 2000) in a customized silicone mold and fully cured on a 70 °C hotplate for 24 hours. The silicone mold, shown in Figure 2.37a, was fabricated by infilling a 3D printed counterpart. The cured epoxy with LCO microlattice was then progressively polished with 320 grit, 400 grit, 600 grit, 800 grit and 1200 grit silicon carbide papers (Buehler), and subsequently 9 μm, 6 μm, 3 μm, 1 μm and 50 nm grit monocrystalline diamond suspensions (Buehler). The polished sample was shown in Figure 2.37b.

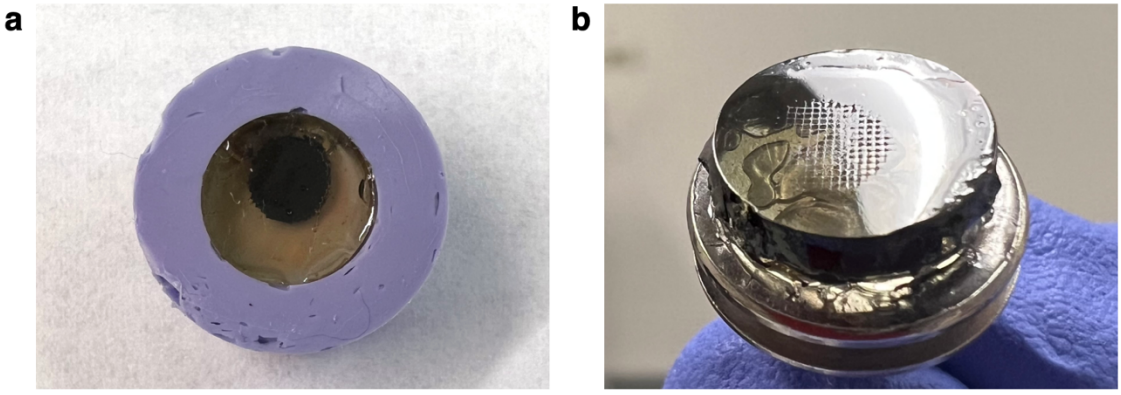

Figure 2.37 The 3D micro-architected LCO lattice mounted in epoxy for nanoindentation. a) The LCO microlattice mounted in epoxy in a customized silicone mold. b) The LCO microlattice in epoxy after progressively polished to a 50 nm grit suspension.

The nanoindentation experiments were performed in SEM (Versa 3D DualBeam, Thermo Fisher), shown in Figure 2.38a, using a nanomechanical testing system (FT-NMT04, FemtoTools AG), shown in Figure 2.38b, under displacement-controlled mode using a diamond Berkovich tip (Figure 2.39). This Berkovich tip has a micro-electromechanical system (MEMS)-based capacitive force sensor (FT-S200000), which has a force range of 200,000 μN with 0.5 μN noise floor (one sigma at 10 Hz).

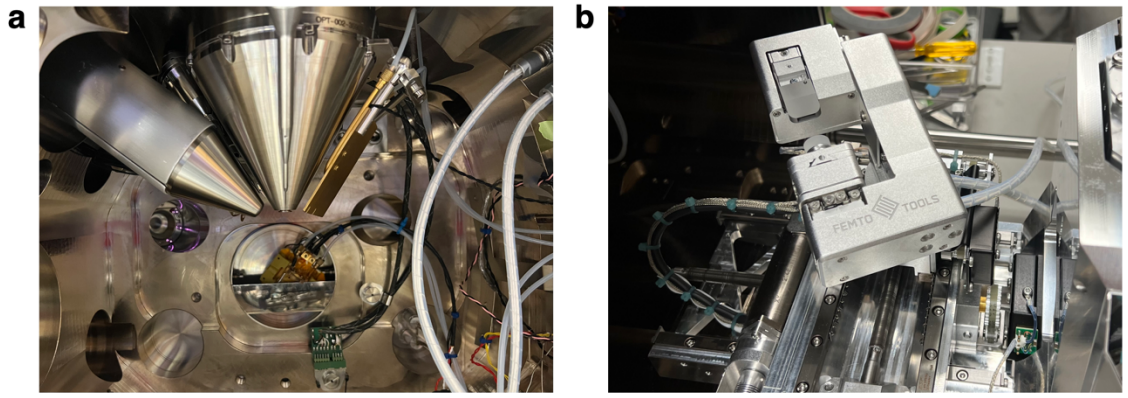

Figure 2.38 Experimental setup for in situ nanoindentation experiments on LCO microlattices. a) The SEM chamber. b) The FemtoTools nanoindentation system mounted on the SEM stage.

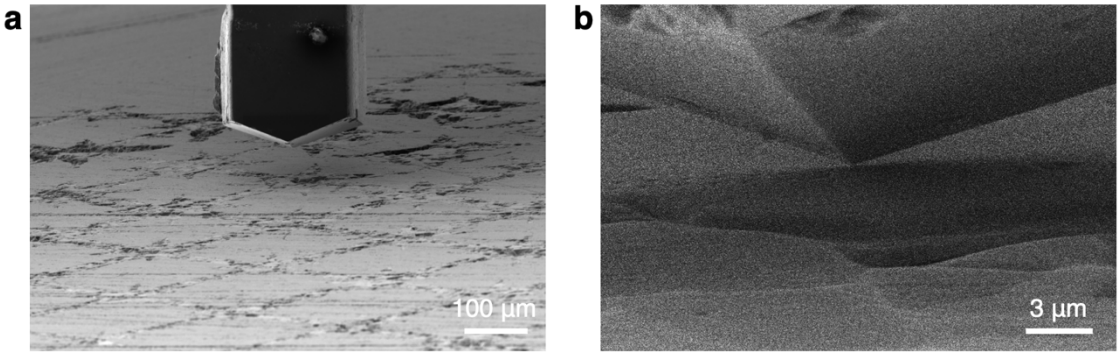

Figure 2.39 SEM images of the diamond Berkovich nanoindentation tip above a polished LCO microlattice sample.

Each indentation was executed at a displacement rate of 5 nm s^{-1} up to a maximum depth of 150 nm. The areas containing multiple LCO grains and grain boundaries were identified in SEM to be the target sites for nanoindentation mapping prior to the experiments. Indentation arrays in the mappings have a spacing of 1.5 μm between individual indents. Continuous stiffness measurement (CSM) technique was utilized, which involves superimposing a 200 Hz oscillating displacement of 3 nm in amplitude, allowing for a continuous measurement of unloading stiffness during the entire global loading process. It is important to keep a small global displacement within one CSM oscillating cycle compared to the CSM amplitude. Since the CSM method relies on the unloading during CSM cycles throughout the global loading to calculate hardness and elastic modulus over the full depth range, if the loading rate is too high for the superimposed oscillation, large systematic error will occur due to the lack of effective unloading in each CSM cycle.

Before nanoindentation experiments on LCO samples, the system was calibrated in two steps using a fused silica standard sample of 12.7 mm in diameter, as shown in Figure 2.40. The fused silica is isotropic in both elastic properties and hardness, with known modulus and hardness values [38].

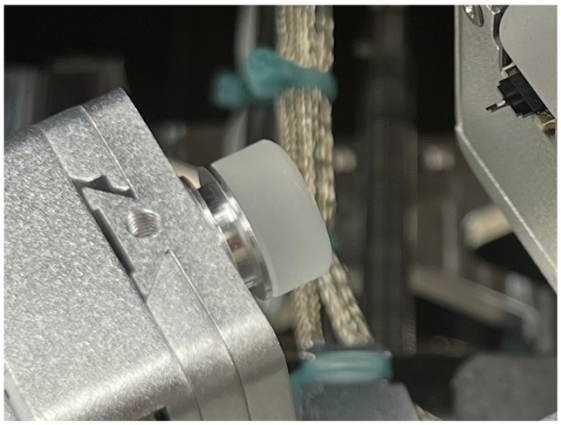

Figure 2.40 Optical image of the fused silica standard sample for calibrations, mounted on the nanoindentation system.

First, a frame compliance map calibration measurement was performed under force-controlled mode, with 5 by 5 indentation arrays centered on the sensor position, and the spacing between individual indents is 1000 μm. Each indentation was executed at a loading rate of 0.2 N s^{-1} up to a maximum depth of 12.5 μm. The measured force and displacement signals are both separated into a global part, P and h, filtered to below the CSM oscillation frequency and an oscillating part as a function of time t with the peak force amplitude a_f (not the root mean square value) and the peak displacement amplitude a_d, as well as the phase lag φ between them. The measured contact stiffness S and the corresponding measured contact compliance C can be calculated through equations

$$S = \frac{a_f}{a_d}\cos\varphi$$

$$C = \frac{1}{S}$$

The whole system is modeled as two springs in series, one representing the sample-indenter combination and the other one representing the load frame, in which case

$$C = C_{s-i} + C_f$$

where C_{s-i} is the compliance of the sample-indenter combination and C_f is the frame compliance. Therefore, to obtain the frame compliance C_f for the calibration purpose, the compliance of the sample-indenter combination C_{s-i} need to be calculated.

With known Young's modulus $E_s = 72.06$ GPa and Poisson's ratio $\nu_s = 0.17$ for the fused silica standard and Young's modulus $E_i = 1140\ GPa$ and Poisson's ratio $\nu_i = 0.07$ for the diamond indenter tip, the reduced modulus of the sample-indenter combination was calculated to be $E_r = 70.25$ GPa according to the relationship

$$\frac{1}{E_r} = \frac{1-\nu_s^2}{E_s} + \frac{1-\nu_i^2}{E_i}$$

The contact stiffness of the sample-indenter combination S_{s-i} is related to the reduce modulus of the sample-indenter combination E_r through the equation

$$\frac{1}{E_r} = \frac{\sqrt{\pi}}{2\beta}\frac{S_{s-i}}{\sqrt{A}}$$

where the geometric factor $\beta = 1.034$ was chosen here for the Berkovich tip, and A is the contact area, which is a function of contact depth h_c and need to be determined in the indenter tip area function calibration in the second calibration step.

Note that the contact depth h_c is smaller than the nominal indentation depth h_n, and is calculated with the equation

$$h_c = h_n - \varepsilon\frac{P}{S}$$

where the geometric factor $\varepsilon = 0.75$ for Berkovich tip. The nominal indentation depth h_n is defined as the displacement after the initial contact point, where the initial contact point was found by a power fit of the force-displacement curve near the initial loading between 5 μN and 100 μN.

The indenter tip area function was calibrated under displacement-controlled mode, using CSM indentation measurements of 3 by 3 arrays with 4 μm spacing. A 200 Hz oscillating displacement of 3 nm in amplitude was superimposed to the global loading. Each indentation was executed at a loading rate of 5 nm s^{-1} up to a maximum depth of 200 nm, fully covering the indentation depth of 150 nm in maximum for LCO samples. With known hardness $H = 9.434$ GPa for the fused silica standard sample, the contact area A can be determined by the measured force P for any indentation depth h_c according to the relationship

$$H = \frac{P(h_c)}{A(h_c)}$$

For an ideal Berkovich tip, $A(h_c) = 24.5h_c^2$, but for a real tip, correction terms need to be added to obtain more accurate area function. Here, we fitted to the measurement data using an area function with 7 coefficients C_1 through C_7

$$A(h_c) = 24.5h_c^2 + \sum_{n=1}^{7} C_n n^2 d h_c e^{-nh_c/d}$$

where $d = 0.3$ was chosen for the fitting.

With the indenter tip area function $A(h_c)$, the expected contact stiffness of the sample-indenter combination S_{s-i} can be obtained, which then gives the frame compliance C_f. The frame stiffness fit range was chosen to be 20% to 100% of the maximum contact depth due to the deviation from the bulk hardness of fused silica at very low indentation depths. The area function fit range was chosen to be 1% to 100% of the maximum contact depth. A fourth-order polynomial was applied to fit the measured frame compliance values at all indented locations to describe the relative spatial distribution of the frame stiffness in Y and Z system directions over the 5 mm by 5 mm calibrated area, centered on the sensor position.

The CSM nanoindentation experiments on the LCO sample generates the force and displacement signals which are separated into the global parts, force P and displacement h, and the oscillating part with peak force amplitude a_f and peak displacement amplitude a_d, as well as the phase lag φ. Similar to the analysis in calibrations, the hardness H of the LCO sample as a function of the contact depth h_c was calculated with the known Berkovich tip area function $A(h_c)$. The measured contact stiffness S was obtained from the oscillation part, which was converted to the measured contact compliance C to give the compliance of the sample-indenter combination C_{s-i} by subtracting the frame compliance C_f. The reduced modulus of the sample-indenter combination E_r as a function of the contact depth h_c was calculated with the stiffness of the sample-indenter combination S_{s-i} and the contact area A for each h_c. Assuming a Poisson's ratio $\nu_s = 0.3$ for the LCO sample and with the known Young's modulus $E_i = 1140\ GPa$ and Poisson's ratio $\nu_i = 0.07$ for the diamond indenter

tip, the indentation modulus of the LCO sample E_s as a function of the contact depth h_c was then calculated.

To identify the crystal orientations of LCO grains on which the nanoindentation experiments were conducted, an electron backscatter diffraction (EBSD) system (AZtec, Oxford Instruments) in SEM (LEO 1550 VP, Zeiss) was used, with a 120 µm aperture at 20 kV. Figure 2.41 shows SEM images of multiple areas on the polished LCO microlattice sample, together with the corresponding EBSD mappings displayed with the inverse pole figure coloring in the z-direction (IPF Z). No extrapolation or other data cleaning procedures were performed on the collected EBSD maps.

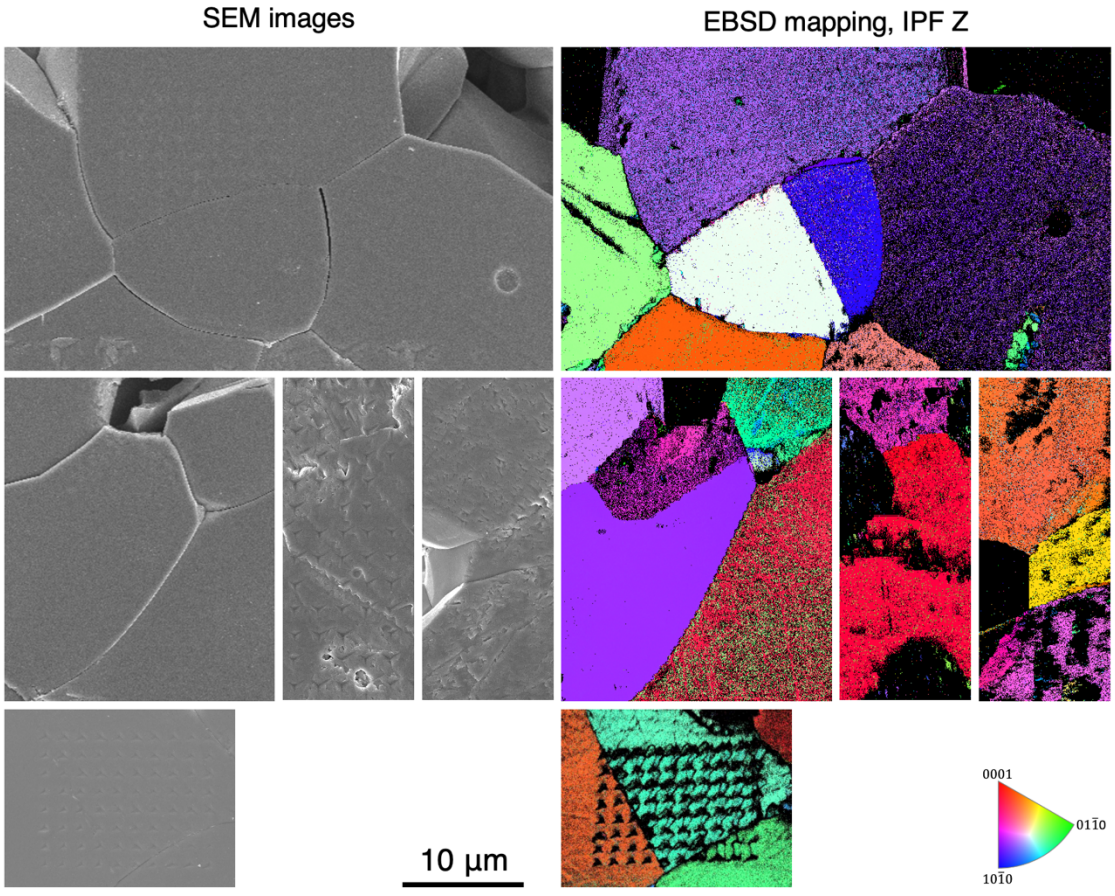

Figure 2.41 SEM images (left) of multiple areas on the polished LCO microlattice sample and the corresponding EBSD mappings displayed with the inverse pole figure coloring in the z-direction.

Figure 2.42a shows a representative nanoindentation mapping across the grain boundary of two adjacent LCO grains, with two indentations performed precisely on the grain boundary highlighted in yellow. Figure 2.42b displays the complementary post-indentation EBSD mapping of the area in the out-of-plane direction. The corresponding maps of hardness H and indentation modulus E_s are presented in Figures 2.42c–d, illustrating a clear dependency on the orientation of LCO grains. The reported values of the indentation modulus and the hardness are the average values between 40–41 nm of the contact depth h_c to eliminate surface effects below 40 nm. The values measured at large contact depths may also deviate from the true value due to the potential crack formation in LCO. Both modules and hardness values on the LCO grain boundary, colored in yellow in Figures 2.42c–d, are intermediate to those on the adjacent grains, which indicates no grain boundary weakening or softening for the sample [37].

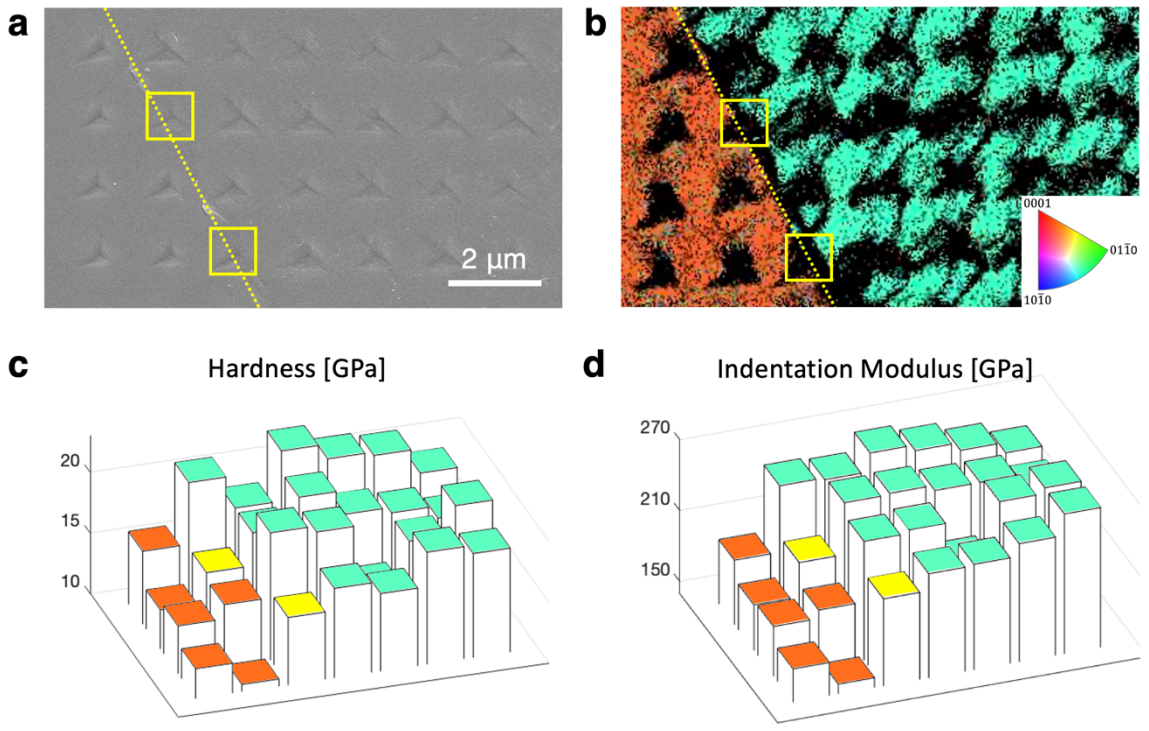

Figure 2.42 Hardness and indentation modulus maps for an area on a polished cross-section of a 3D micro-architected LCO. a) The SEM image of the nanoindentation mapping. b) The corresponding EBSD image over the indented area. c) The hardness map for the area. d) The indentation modulus map for the area.

Figure 2.43 summarizes indentation modulus across five distinct LCO crystal orientations, showing a trend of decreasing modulus as the indentation direction aligns more closely with [0001], the crystallographic c-axis of LCO. The alignment of these two orientations is quantified as the absolute value of the dot product between unit vectors in these directions, denoted as $|\hat{c}_{crystal} \cdot \hat{z}_{indentation}|$. Crystal orientations were determined using EBSD, extracted from areas away from the indentations on each grain. Table 2.8 lists the measured crystal orientation Euler angles in Bunge convention and the corresponding calculated $|\hat{c}_{crystal} \cdot \hat{z}_{indentation}|$ for the five LCO crystals. Figure 2.44 demonstrates the crystal orientations in detail for the five studied grains from top and side views along the indentation direction. Across all individual nanoindentation measurements, the indentation modulus varies between 148.4 GPa and 286.6 GPa.

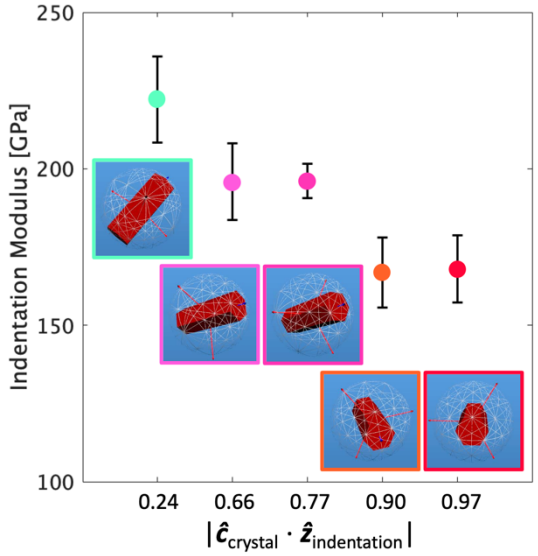

Figure 2.43 LCO indentation modulus as a function of the crystal orientation, quantified by $|\hat{c}_{crystal} \cdot \hat{z}_{indentation}|$. The inset images are the crystal orientation for each grain in the out-of-plane direction for indentations.

	Crystal orientation Euler angles in Bunge convention			$\lvert\hat{c}_{\text{crystal}} \cdot \hat{z}_{\text{indentation}}\rvert$
	φ_1	ϕ	φ_2	
Orientation 1	139.3°	103.8°	115.8°	0.24
Orientation 2	106.8°	49.0°	72.5°	0.66
Orientation 3	107.8°	39.9°	103.2°	0.77
Orientation 4	27.9°	26.3°	13.5°	0.90
Orientation 5	173.0°	165.9°	24.4°	0.97

Table 2.8 Crystal orientation Euler angles in Bunge convention measured from EBSD for five indented LCO grains and the corresponding calculated $|\hat{c}_{\text{crystal}} \cdot \hat{z}_{\text{indentation}}|$ values.

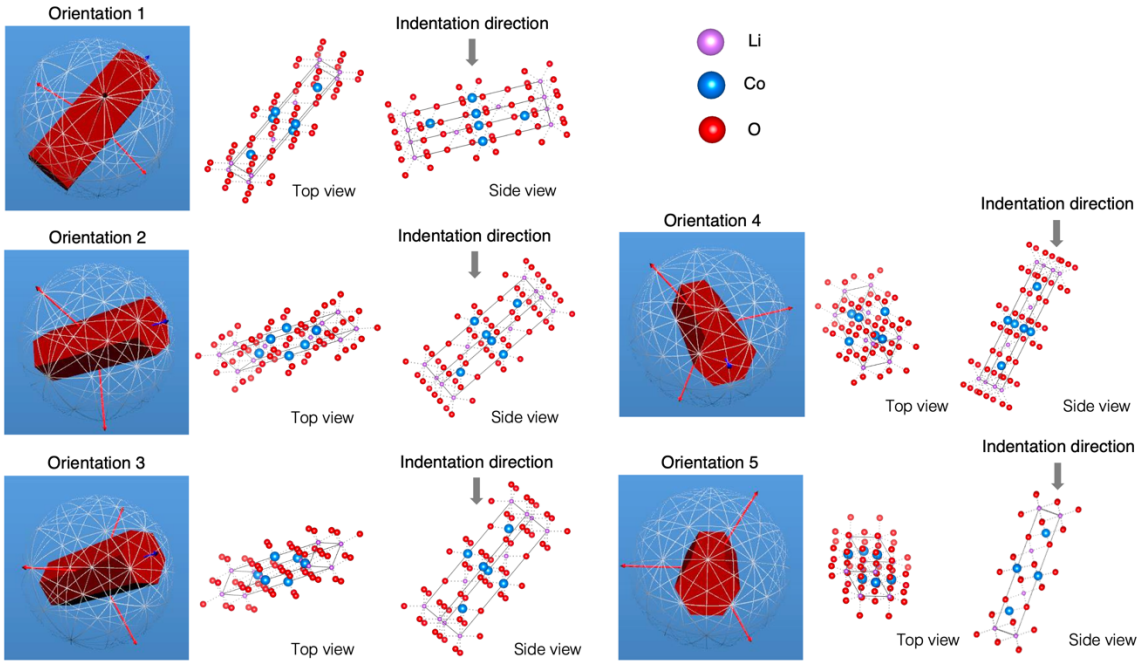

Figure 2.44 Illustration of LCO crystal orientations from top and side views along the indentation direction for the five studied LCO grains.

Figure 2.45a shows a representative indentation impression with the corresponding LCO crystal orientation. The load-displacement curve of this indentation experiment is in Figure 2.45b, with the calculated hardness and indentation modulus as functions of contact depth

during loading shown in Figures 2.45 c–d. In this case, the indentation direction is nearly perpendicular to [0001] ($|\hat{c}\cdot\hat{z}| = 0.24$), and the load-displacement curve shows multiple load drops, highlighted by arrows. Cracks are observed along the LCO basal plane from the image of impression. Its hardness as a function of contact depth exhibits notable discontinuities, with a significant decrease around 140 nm depth, corresponding to a large pop-in event on the load-displacement curve. The indentation modulus shows a significant decrease with depth, resulting in ~60 GPa difference between 40 nm and 150 nm.

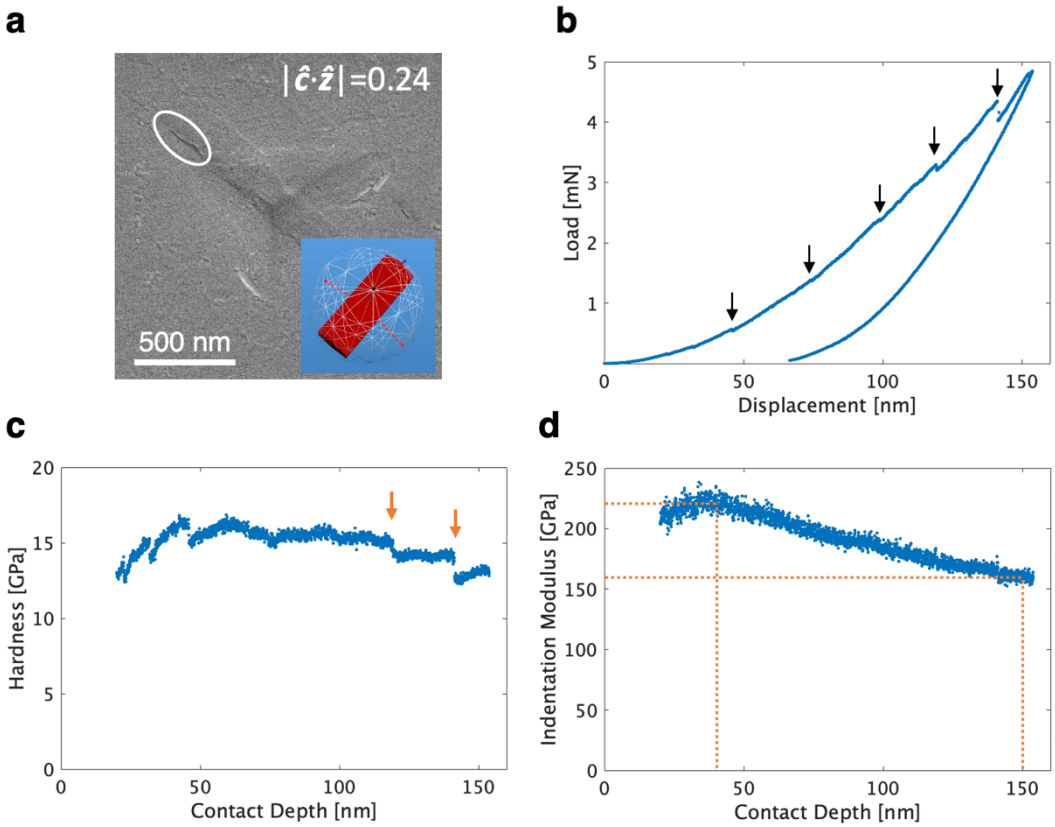

Figure 2.45 A representative nanoindentation experiment for an LCO grain with an orientation of $|\hat{c}\cdot\hat{z}| = 0.24$. a) The indentation impression. The inset is a schematic of its crystal orientation. b) The load-displacement curve obtained from this indentation experiment and the calculated c) hardness and d) indentation modulus, both as functions of the contact depth.

In contrast, the experiment on an LCO grain with the indentation direction nearly aligned along [0001] ($|\hat{c}\cdot\hat{z}|$ = 0.90), with a representative indentation impression and the corresponding crystal orientation shown in Figure 2.46a, gives a steadier load-displacement curve as demonstrated in Figure 2.46b. No apparent load drops are observed within the 150 nm maximum depth. This orientation exhibits only a minor decrease in hardness (Figure 2.46c) and a relatively stable indentation modulus which leads to a smaller difference of ~30 GPa between 40 nm and 150 nm depths (Figure 2.46d).

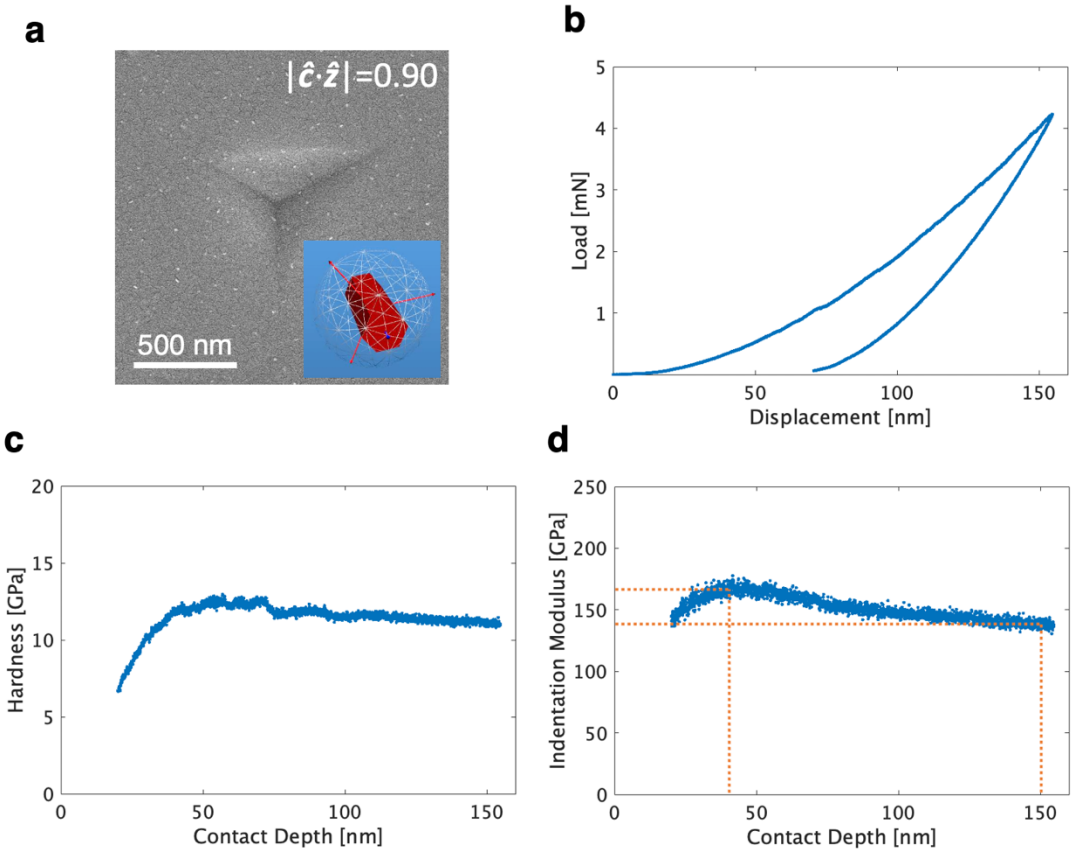

Figure 2.46 A representative nanoindentation experiment for an LCO grain with an orientation of $|\hat{c}\cdot\hat{z}|$ = 0.90. a) The indentation impression. The inset is a schematic of its crystal orientation. b) The load-displacement curve obtained from this indentation experiment and the calculated c) hardness and d) indentation modulus, both as functions of the contact depth.

Anisotropic mechanical properties are expected for LCO as a result of its crystallographic anisotropy. Wu et al. calculated Young's modulus for LCO with the energy-strain approach utilizing two different packages [39]. Vienna ab intio Simulation Package (VASP) gave EX = 321.05 GPa / EZ = 212.83 GPa and Cambridge Serial Total Energy Package (CASTEP) gave EX = 290.06 GPa / EZ = 177.25 GPa, where X and Z correspond to $[11\bar{2}0]$ and [0001] directions, respectively.

Qu et al. employed simple nanoindentation experiments on 21 LCO grains following the Oliver-Pharr method, reporting Young's modulus ranging from 151–236 GPa [40]. Their method, without a superimposed oscillation to the global loading and unloading, calculates the contact stiffness from the unloading curve after reaching a maximum indentation load of 2 mN, corresponding to a typical indentation depth of around 100 nm. The Oliver-Pharr method calculates Young's modulus using contact stiffness independent of indenter shape, under the assumption of isotropic elasticity [37]. For highly anisotropic materials like LCO, the relation between contact stiffness and Young's modulus is not as straightforward due to the dependency on indenter geometry [41,42]. Moreover, the method's accuracy requires the absence of fracturing during loading, as crack closure will contribute to unloading displacement, thus affecting the measured indentation modulus. This is particularly relevant for LCO, where nanoindentation instability varies with the crystal orientation, as demonstrated in our discussion of two representative indentation experiments in which we observed significantly different contact depths for the occurrence of the initial failure. Failures can occur at as early as ~50 nm depth for orientations with $|\hat{\boldsymbol{c}}\cdot\hat{\boldsymbol{z}}|$ close to 0, while more stable behaviors are observed for $|\hat{\boldsymbol{c}}\cdot\hat{\boldsymbol{z}}|$ near 1. The commonly observed early failures in certain orientations suggest a potential underestimation of LCO's modulus calculated from unloading curves in simple nanoindentation experiments, especially for maximum depths above 50 nm. This underestimation is directly demonstrated by the measurements for LCO grains in these orientations using CSM technique, which shows a significant decrease in indentation modulus with depth as in Figure 2.45d.

2.11 Gel Infusion Additive Manufacturing for Other Cathode Materials

This gel infusion AM technique simplifies the creation of 3D micro-architected battery materials by eliminating the need for extensive photoresin design and printing parameter optimization typically required in VP 3D printing. The LCO fabrication process showcased here is adaptable for a large variety of Li-ion battery cathode materials. It is especially suitable for the two main categories: (1) lithium transition metal oxides, where the transition metals are mainly cobalt, nickel and manganese, including $LiMO_2$ (M = Co, Ni, Mn, etc.) or LiM_2O_4 (M = Mn, etc.) type compounds, and (2) lithium metal phosphates of the form $LiMPO_4$ (M = Fe, Mn, Ni, Co, etc.) [43]. This method also holds promise for mixed lithium metal oxides, such as $LiNi_xMn_yCo_{1-x-y}O_2$ with tunable transition metal stoichiometry [44].

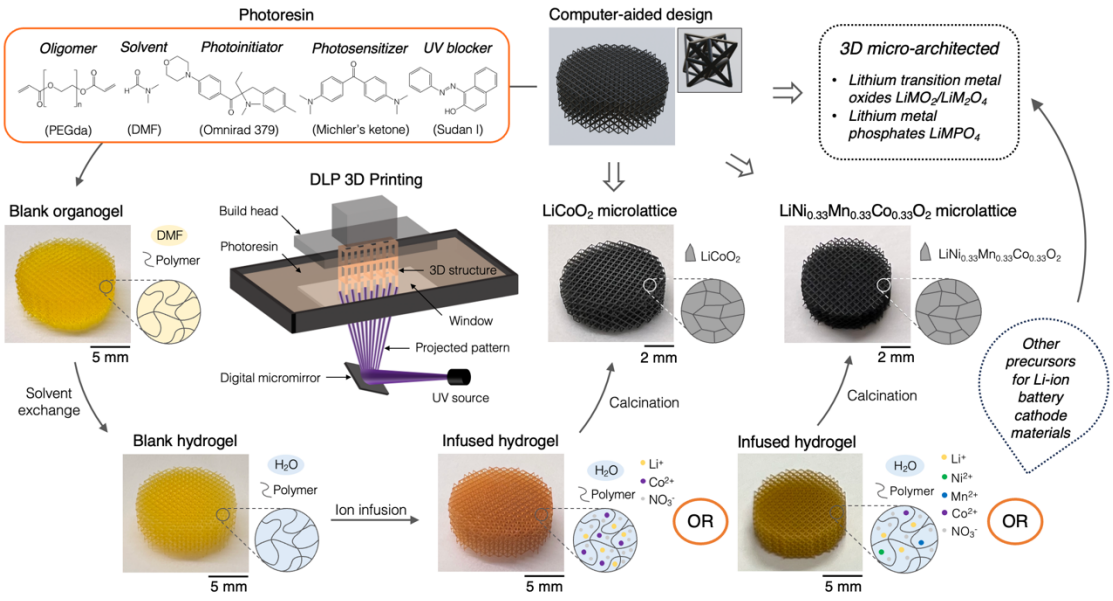

Figure 2.47 Generalization of the gel infusion additive manufacturing process for 3D micro-architected cathodes from LCO to other types of cathode materials for lithium-ion batteries.

Figure 2.47 highlights the versatility of this AM technique by comparing the fabrication processes of micro-architected LCO and $LiNi_{0.33}Mn_{0.33}Co_{0.33}O_2$ (NMC111). They both follow a similar initial process involving computer-aided 3D structure design, high resolution VP 3D printing of the blank organogel and solvent exchange into the blank hydrogel. The

divergence in the target materials for synthesis arises with the infusion of distinct metal precursors, followed by the synthesis of each target material through a similar calcination process. Switching the infusion solution to 2M $LiNO_3$ with 0.67M $Ni(NO_3)_2$, $Mn(NO_3)_2$ and $Co(NO_3)_2$, we demonstrated a straightforward fabrication of 3D architected NMC111 microlattice with 45 μm beam diameters (Figure 2.48a). The sample was sintered under the standard condition of 1 atm Ar up to 700 °C, as in Figure 2.21a. Figure 2.48b shows an SEM image of its beam cross-section and an ion channeling contrast image for an area near the center which shows ~100 nm of the grain size. EDS element mapping reveals a uniform distribution of O, Ni, Mn and Co atoms, as demonstrated in Figure 2.49. Sample crystal structure was confirmed with XRD, with the pattern shown in Figure 2.50.

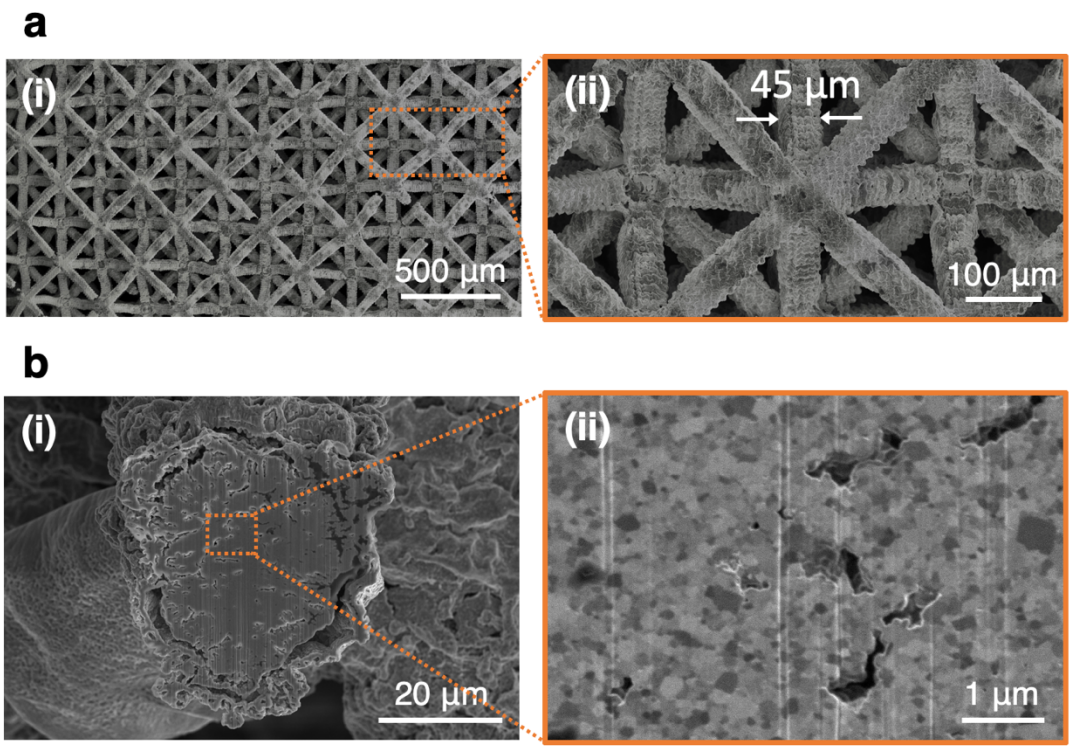

Figure 2.48 The NMC111 microlattice and its beam cross-section. a) SEM images of a 3D micro-architected NMC111 octet truss lattice in top view. b) (i) SEM and (ii) ion channeling contrast images of its beam cross-section.

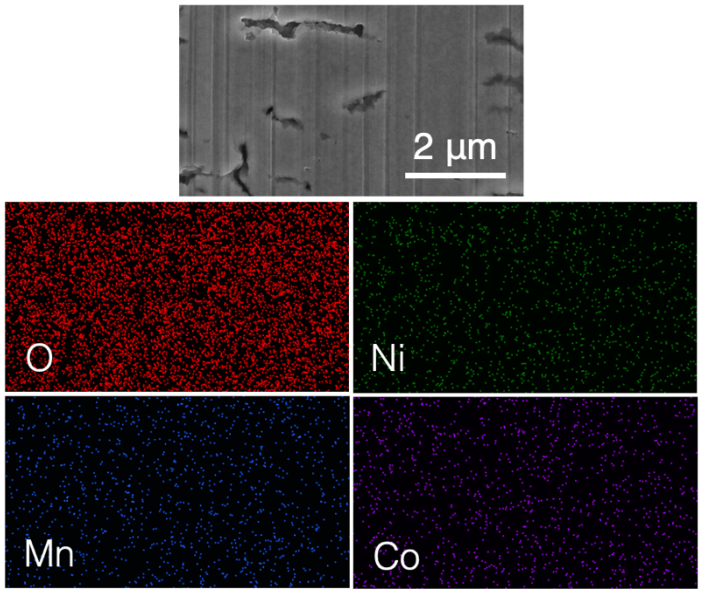

Figure 2.49 EDS element mapping of the beam cross-section of an NMC111 microlattice.

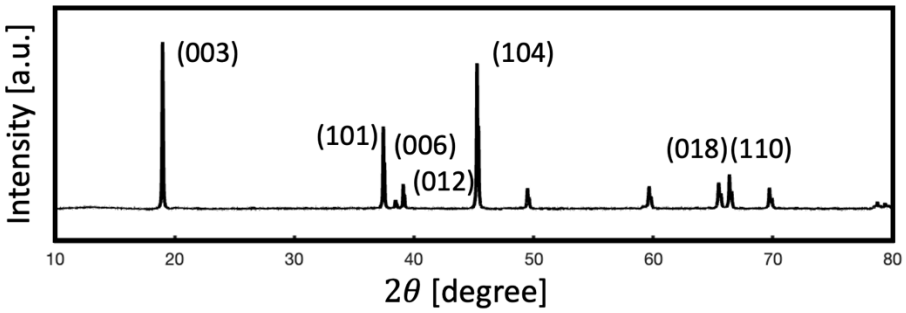

Figure 2.50 XRD pattern for the additively manufactured NMC111 microlattice.

To apply this gel infusion additive manufacturing technique across a more diverse range of other oxide and phosphate-type cathode materials for lithium-ion batteries, as shown on the right side of Figure 2.47, the extensively studied sol-gel methods can often provide a robust starting point, as they could guide the selection of suitable precursors for infusion and help in determining the optimal conditions for the thermal synthesis reactions [45–47].

Chapter 3

3D LITHIUM ANODE WITH MICRO-ARCHITECTED CARBON SCAFFOLD

3.1 Overview

3D micro-architected carbon lattices can be additively manufactured through a straightforward conversion via pyrolysis from 3D printed polymer microlattices, as mentioned in Chapter 1.3. Narita et al. developed a fabrication method to create 3D glassy carbon microlattice as the anode for lithium-ion batteries, achieving the smallest feature size (diameter of microlattice beams) of 28 μm [24]. This carbon electrode is mechanically robust, with a maximum pre-collapse stress of 27 MPa for a 45° tilted square lattice of 1 mm in thickness with a porosity of 90%. It is glassy carbon with the microstructure mostly composed of differently oriented graphitic layers, and it has been demonstrated as the carbon anode for lithium-ion batteries which stores lithium ions by intercalation. Beyond directly serving as an anode, this carbon microlattice also has a great potential to be used as a 3D scaffold for the lithium-metal anode due to its small feature size and the ability to contain independently controlled structural factors in both unit cells and the bulk lattice.

Safe and durable lithium metal electrodes will bring about a revolutionary increase in battery energy density due to their ultrahigh theoretical specific capacity of 3860 mAh g^{-1} and the low electrochemical potential of -3.04 V versus the standard hydrogen electrode [48]. Although lithium metal anodes were often used in battery research since the very early stages in the 1970s [6], they were gradually omitted from the commercialization of lithium-ion batteries due to the safety concerns. The dendrites commonly formed during lithium plating may cause shorting between the cathode and anode, which risks thermal runaway and even explosion of the battery [49]. The morphology of the lithium deposited during plating is closely related to the current density and the ionic distribution near the electrode surface. To lower the effective current density, in order to mitigate lithium dendrite growth, host materials have been widely studied, among which porous carbon-based materials, usually

made of carbon fiber, carbon nanotube, graphene or biomass-derived carbon, are most promising due to their outstanding chemical resilience and light weight [50].

As shown in Figure 3.1, Zhang et al. demonstrated a carbon fiber network film prepared by vacuum filtration, which suppressed the formation of dendritic lithium as on a copper foil current collector during plating, giving a generally flatter anode surface and achieving an average Coulombic efficiency of 99.9% for 300 cycles at a current density of 2.0 mA cm^{-2} with 1 mAh cm^{-2} lithium loading [51].

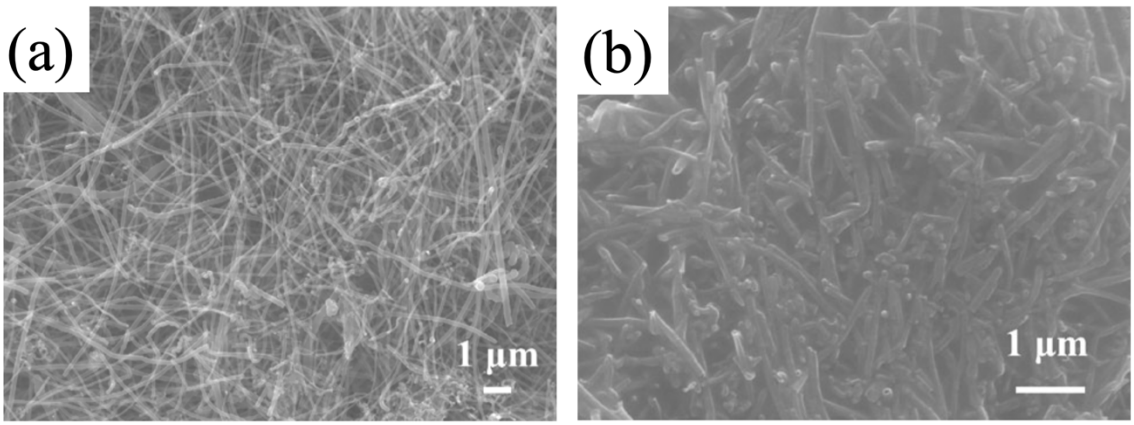

Figure 3.1 Carbon fibers as the host material for lithium anodes. SEM images a) before and b) after lithium deposition. Adapted with permission from reference [51]. Copyright 2016 Tsinghua Press, co-published with Springer.

Want et al. utilized a biomass-derived carbon material as lithium metal host which achieved an average Coulombic efficiency of 99.1% with the areal capacity of 2.2 mAh cm^{-2} [52]. Prepared by carbonizing an eggplant, this material has channel-like structures as shown in Figure 3.2. The carbon sample was coated with zinc oxide using atomic layer deposition and then infused with lithium through a melt infusion process, followed by a surface coating of lithium fluoride through the reaction with commercial Freon R134a under 0.5 atm and 120 °C for 24 hours.

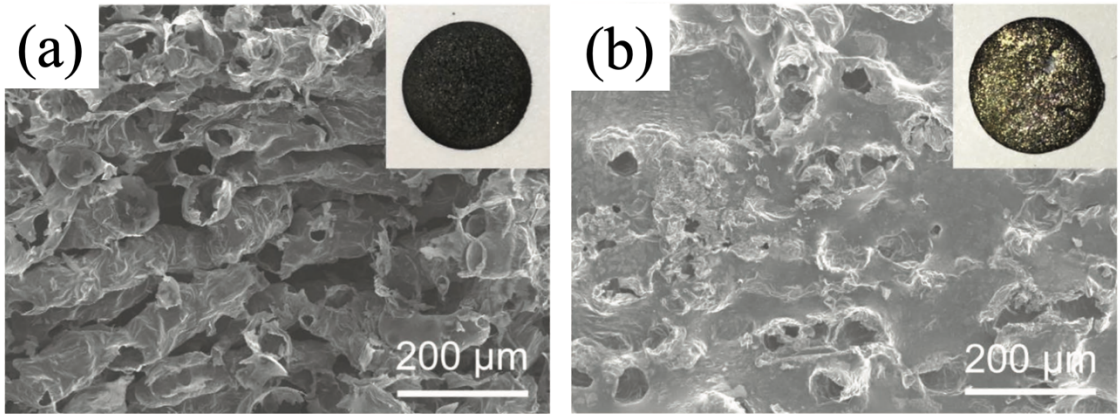

Figure 3.2 Carbonized eggplants as the host material for lithium anodes. SEM and optical (inset) images a) before and b) after zinc oxide coating using atomic layer deposition and melt infusion of lithium. Adapted with permission from reference [52]. Copyright 2019 Wiley.

Unlike the stochastic 3D structure in the porous carbon-based materials made of carbon fiber, carbon nanotube, graphene or biomass-derived carbon, additive manufacturing techniques enable the creation of 3D porous carbon materials with periodic structures and well-defined form factors. We utilized VP 3D printing and pyrolysis to fabricate 3D architected porous carbon scaffolds with flexibly designed micron-to-centimeter form-factors and outstanding mechanical strength. We investigated surface functionalization and studied lithium electrodeposition conditions to achieve dense lithium nucleation and uniform epitaxial growth on the surface of the carbon scaffold. The fabricated free-standing 3D architected lithium metal electrode was able to accommodate the large volume change of lithium during cycling and the resulting mechanical stress built up in the battery compared to the lithium foil electrode. Smooth lithium morphology was observed after 200 cycles of symmetric cycling at current density of 1.0 mA cm^{-2} with 1 mAh cm^{-2} lithium loading.

3.2 Fabrication of 3D Micro-Architected Carbon Scaffold

The fabrication process for 3D carbon scaffolds mainly follows the method developed by Narita et al. [24]. A commercially available photoresin, PR-48 (Arkema) with the composition listed in Table 3.1, was used to print 3D architected polymer microlattices with a DLP 3D printer (Titan 3, MicroSLA). The printing parameters shown in Table 3.2.

Component	Amount
Allnex Ebecryl 8210	39.776%
Sartomer SR 494	39.776%
2,4,6-Trimethylbenzoyl-diphenylphosphineoxide	0.400%
Rahn Genomer 1122	19.888%
2.2'-(2,5-thiophenediyl)bis(5-tertbutylbenzoxazole)	0.160%

Table 3.1 Composition of the commercially available photoresin PR-48 for 3D printing.

Slice thickness (mm)	0.025	**LED Current (5.86 mA per unit)**	200	
	Exposure Time (s)	**Lift Height (mm)**	**Lift Speed (mm min^{-1})**	**Down Speed (mm min^{-1})**	**Delay Time (s)**
First layer	2	4	25	150	1
Remaining layers	0.8	4	25	150	1

Table 3.2 Printing parameters for the PR-48 photoresin using the Titan 3 DLP printer (MicroSLA).

The printed polymer samples were soaked in propylene glycol methyl ether acetate (PGMEA) for 2 hours to fully remove the unreacted photoresin, then rinsed with isopropanol and dried. As illustrated in Figure 3.3, the printed polymer microlattices were pyrolyzed in a tube furnace (OTF-1500X, MTI) under vacuum with a pressure around 0.001 atm up to 1000 °C, following the temperature profile in Figure 3.4, to give 3D micro-architected carbon lattices. The decomposition of polymer during pyrolysis generates CO_2 and H_2O which are released from the structure, and the obtained carbon microlattices undergoes isotropic linear shrinkage to around 30% of the polymer microlattices.

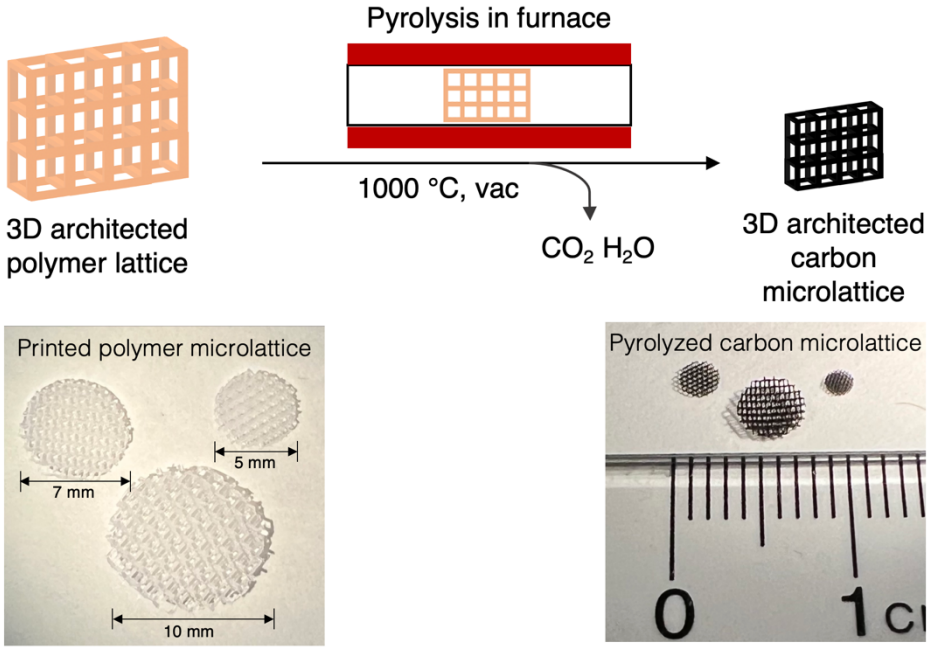

Figure 3.3 Schematic of the pyrolysis process and optical images of printed polymer microlattices and pyrolyzed carbon microlattices.

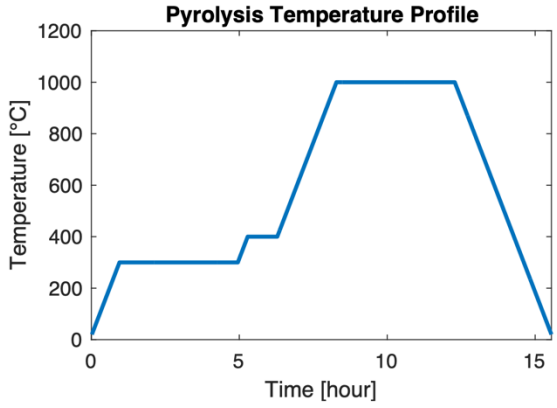

Figure 3.4 Pyrolysis temperature profile for the synthesis of carbon microlattice from PR-48 polymer microlattice.

The low pressure around 0.001 atm is important for this pyrolysis process, which helps to prevent gas bubbles from being trapped inside the structure during decomposition and

shrinkage. A pyrolyzed 3D micro-architected carbon sample with severe structural deformation due to the trapped gas bubbles is shown in Figure 3.5.

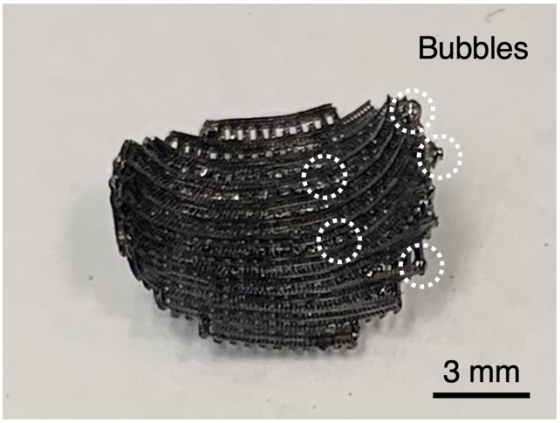

Figure 3.5 A 3D micro-architected carbon sample severely deformed due to the trapped gas bubbles formed during pyrolysis.

The overall geometry of the sample was designed to be a cylindrical disk with a handle, and the lattice was composed of tilted cubic unit cells. Samples with two different sizes were fabricated, and the corresponding dimensions of their CAD models are shown in Figure 3.6. The smaller samples were used for investigating lithium electrodeposition conditions, as discussed in Chapter 3.3, and various surface coatings applied to the 3D carbon scaffold, as described in Chapter 3.4. The larger samples were fabricated for symmetric cycling experiments in coin cells, which will be discussed in Chapter 3.6. The purpose of adding a handle structure on the 3D microlattice will be illustrated during the discussion of the lithium electrodeposition and surface coating processes.

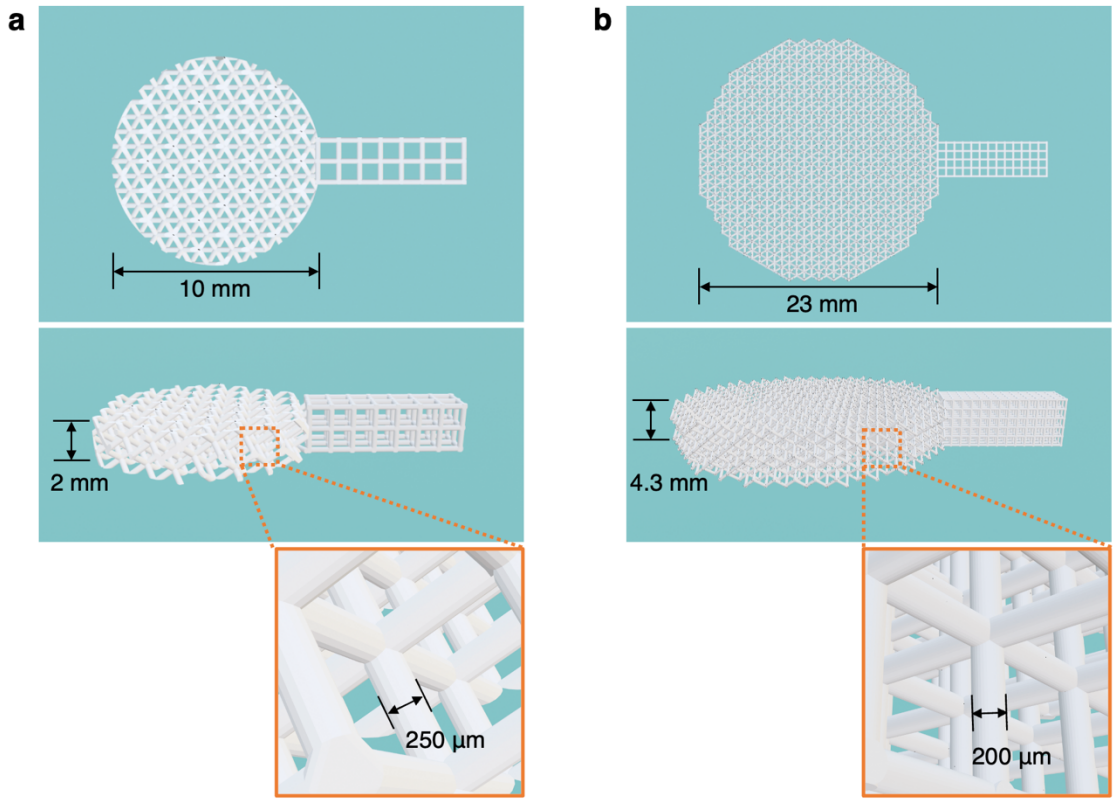

Figure 3.6 Computer-aided design (CAD) models for 3D printed polymer microlattices with a) small and b) large overall dimensions.

Figures 3.7a–b present a small polymer microlattice as printed and the corresponding pyrolyzed carbon microlattice. During pyrolysis, the overall dimensions of the sample experience isotropic linear shrinkage of approximately 73%, and the lattice beam diameter shrinks approximately 76% from 250 µm to 60 µm, as shown in the SEM images of the carbon sample in Figure 3.8. Surface roughness with a layered-geometry is observed on the lattice beams, which is intrinsically related to the layered-curing mechanism of DLP 3D printing, illustrated by the schematic in the inset of Figure 3.8b. Figures 3.9a–b demonstrate a large polymer microlattice as printed and the corresponding pyrolyzed carbon microlattice sample. The large sample exhibits isotropic linear shrinkage of approximately 74% for the overall geometry and the beam diameter shrinkage of approximately 77% from 200 µm to 46 µm, as shown in Figure 3.9c. The relative density of the 3D micro-architected carbon lattice is around 13% (87% porosity).

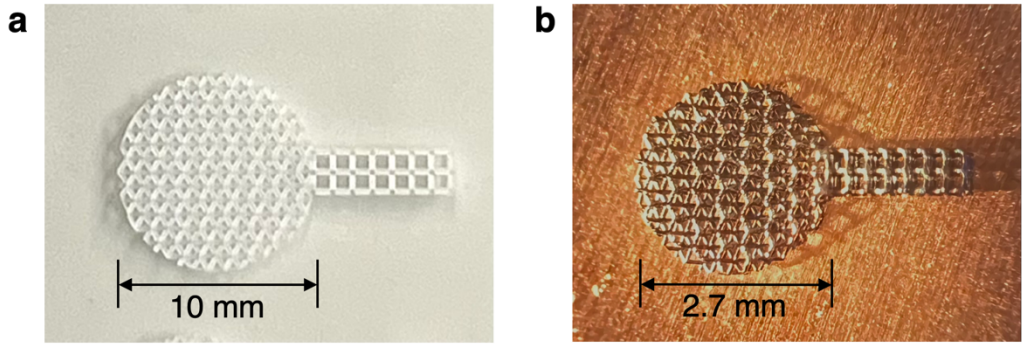

Figure 3.7 Optical images of a small a) polymer microlattice as printed and b) its corresponding pyrolyzed carbon microlattice.

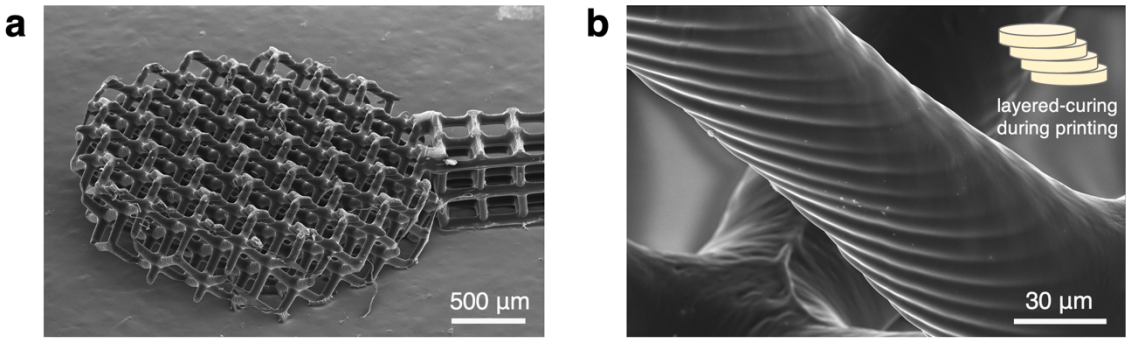

Figure 3.8 SEM images of a) a small carbon microlattice and b) a beam of this lattice, showing surface roughness with a layered-geometry intrinsically related to the layered-curing mechanism (inset) of 3D printing.

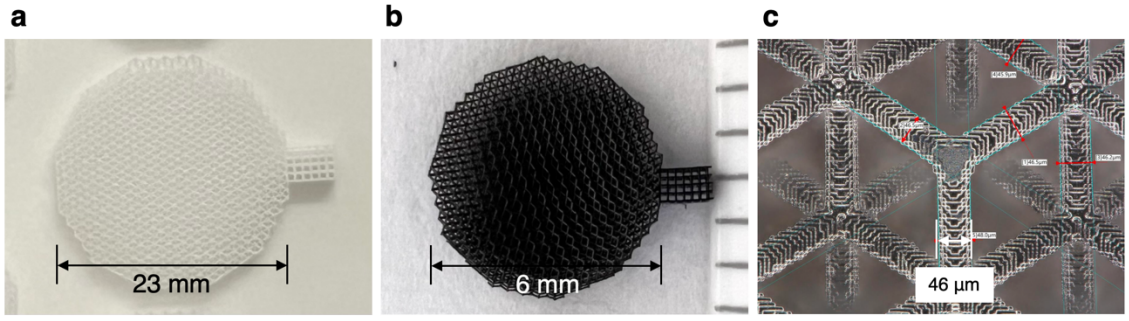

Figure 3.9 Optical images of a large a) polymer microlattice as printed and b) its corresponding pyrolyzed carbon microlattice. c) Optical microscope image of the carbon microlattice from top-view.

3.3 Electrodeposition of Lithium on 3D Carbon Scaffold

We plan to use the micro-architected carbon lattice as a scaffold for lithium metal anode and store lithium in the free volume of the lattice, which accounts for 87% of the overall volume, instead of intercalating lithium ions into the glassy carbon as demonstrated by Narita et al. [24]. A conformal layer of lithium needs to be electrodeposited on the surface of the carbon microlattice before the electrode is assembled as the anode in a full battery. This is done to compensate for the loss of lithium inventory during cycling. The experimental setup for the lithium electrodeposition reaction is placed in an Ar glovebox, demonstrated in Figure 3.10, and the electrodes are connected to a potentiostat (SP200, BioLogic) outside the glovebox.

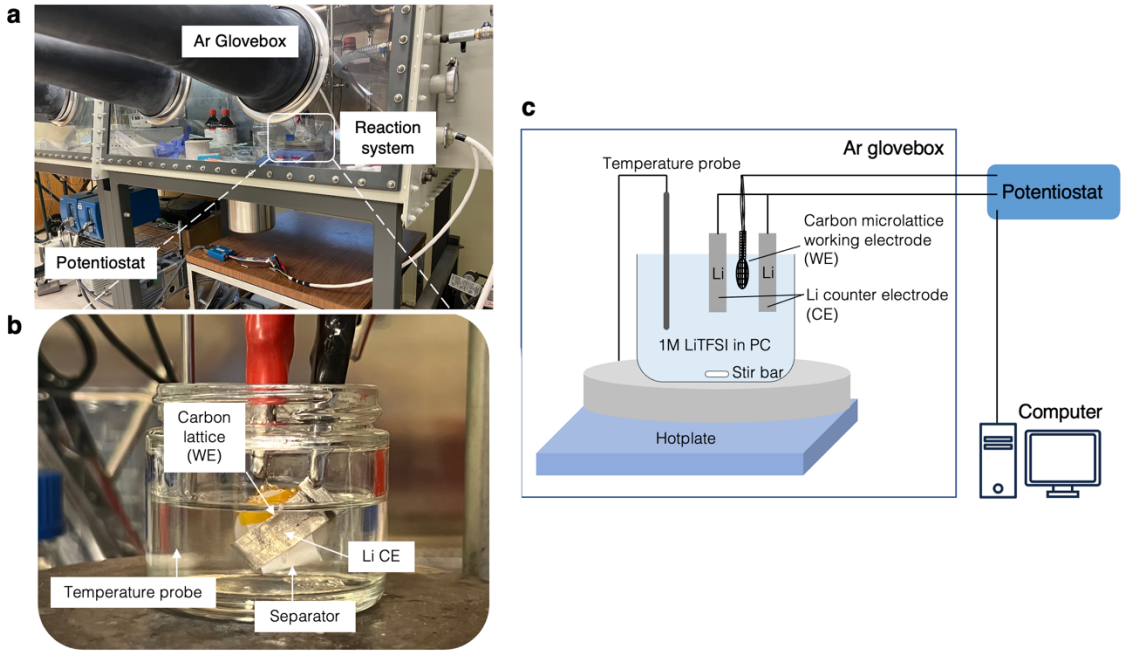

Figure 3.10 Optical images of a) the experimental setup for lithium electrodeposition in an Ar glovebox connected to a potentiostat outside the glovebox and b) a close view of the reaction system. c) Schematic of the experimental setup.

The electrodeposition reaction took place in 1M lithium bis(trifluoromethane)sulfonimide (LiTFSI) solution at 60 °C with stirring, and lithium foil was used as the counter electrode. Conductive wires to connect the carbon lattice to a metal clip were attached to it via the

handle structure that helps prevent the physical contact between wires and the lattice disk. We used the Cu/Ni wire of 130 µm in diameter, which can be inserted into the pores on the handle, as shown in Figure 3.11.

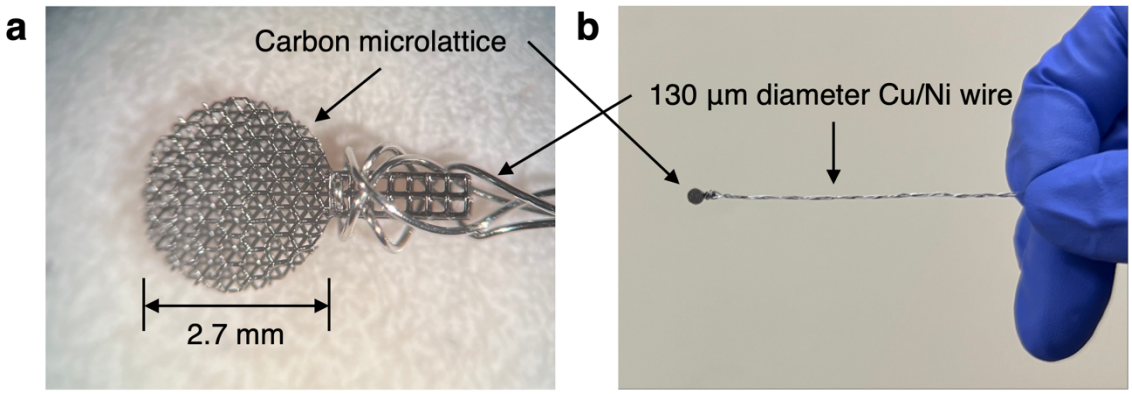

Figure 3.11 Optical images 3D micro-architected carbon lattices with the attached Cu/Ni wire.

The sample is fixed in the center of an HDPE washer with 2 mm in thickness (Figure 3.12a), and covered by a separator film (Celgard 2325) with Kapton tape (Figure 3.12b) before being sandwiched between two sheets of lithium foil, used as the counter electrode (Figure 3.12c). The separator prevents the potential contact between the working and counter electrodes during the electrodeposition reaction (Figure 3.12d).

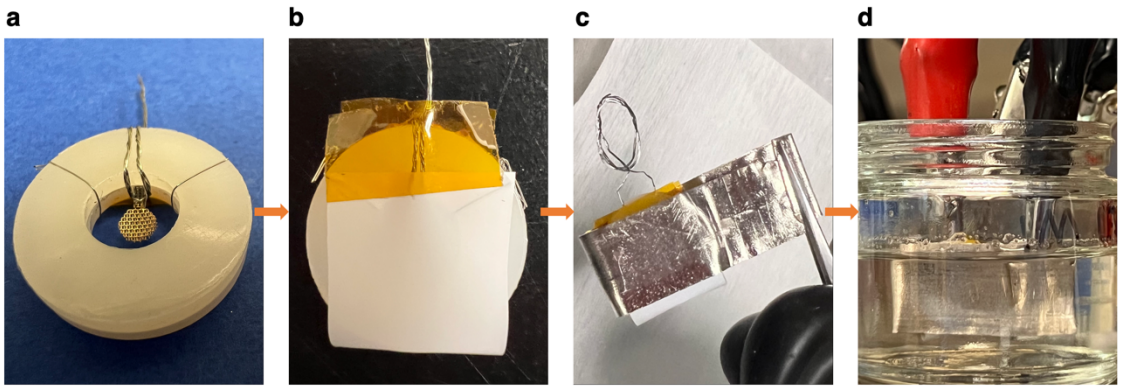

Figure 3.12 Optical images of the process to prepare a small 3D carbon microlattice for lithium electrodeposition.

After electrodeposition, the sample was air sensitive, as lithium will rapidly react with the moisture in ambient conditions. To image the sample in SEM (Versa 3D DualBeam, Thermo Fisher), an air-free transfer tool (Vacushut, Figure 3.13a) was used to transfer the sample from the Ar glovebox to the SEM chamber. The Vacushut was also sealed in a secondary container during transfer (Figure 3.13b). Figure 3.13c shows how the Vacushut lid opens to expose the sample due to the expansion of a gas-filled bag when the vacuum level in the SEM chamber goes up.

Figure 3.13 Optical images of a) Vacushut, a tool for air-free sample transfer from glovebox to SEM chamber, and b) Vacushut sealed in a secondary container. c) Vacushut lid opens in SEM chamber.

When the small carbon lattice was electrodeposited with 5 mA direct current (32 mA cm^{-2} for surface area of the cylindrical disk with 2.7 mm diameter and 0.5 mm thickness) for 30 minutes, a significant amount of lithium was non-uniformly deposited, partially covering the lattice and mainly staying on the outer surface of the cylindrical disk (Figure 3.14).

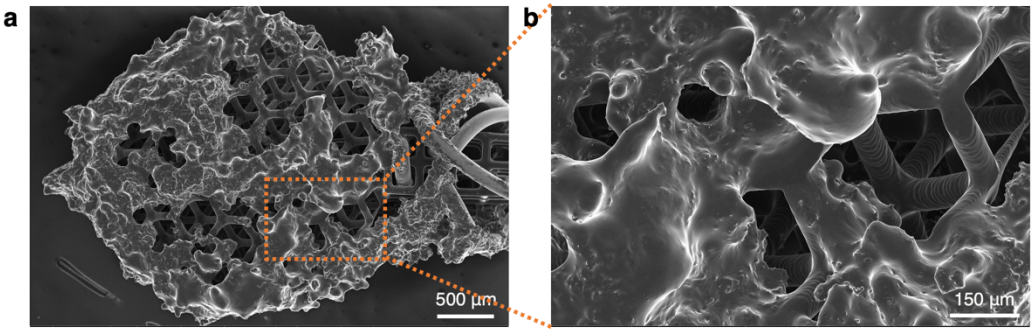

Figure 3.14 SEM images of a 3D micro-architected carbon lattice after lithium electrodeposition with 5 mA direct current for 30 minutes.

Compared to direct current, pulse current allows for the ion diffusion in the electrolyte solution to replenish at the electrode surface during the off periods, which helps maintain a consistent ion concentration across the surface and often gives better uniformity in metal electroplating, which has also been observed to improve lithium morphology [53]. However, when the sample is electrodeposited with 5 mA pulse current, with 1 second on and 1 second off, for 30 minutes of the total pulse-on time, only small amount of highly mossy lithium was observed on the carbon microlattice, as shown in Figure 3.15.

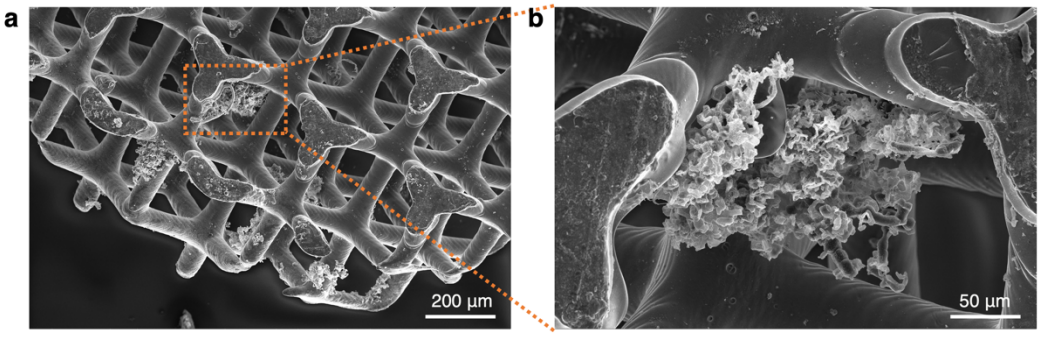

Figure 3.15 SEM images a 3D micro-architected carbon lattice after lithium electrodeposition with 5 mA pulse current (1s on, 1s off) for 30 minutes of the total pulse-on time.

The non-uniform lithium plating is mainly due to the carbon substrate. There is a high interfacial energy between carbon and lithium, which leads to an overpotential for lithium nucleation to overcome the heterogeneous nucleation barrier on the carbon substrate [54]. Therefore, the surface of carbon microlattice needs to be engineered, for example by coating a lithiophilic material which gives small or zero lithium nucleation overpotential, to achieve conformal lithium electrodeposition.

3.4 Lithium Morphology Tailoring with Various Surface Coatings on 3D Carbon Scaffold

Au is known to be lithiophilic as a substrate for heterogeneous lithium nucleation [54]. When Li is plated on Au, two alloy phases of Li_xAu form before the formation of the pure Li phase. In addition, the binary phase diagram between Au and Li (Figure 3.16) indicates there exists a region where a very small amount of Au dissolves in Li at room temperature, allowing Au atoms on the surface layers of Li_xAu to dissolve into Li to form a buffer layer. This solid solution buffer layer has the same crystal structure as pure Li, and can significantly reduce Li nucleation energy, resulting in a near zero overpotential for Li electroplating on Au. Therefore, coating Au on the surface of the 3D micro-architected carbon lattice will in turn create a lithiophilic substrate for Li electrodeposition.

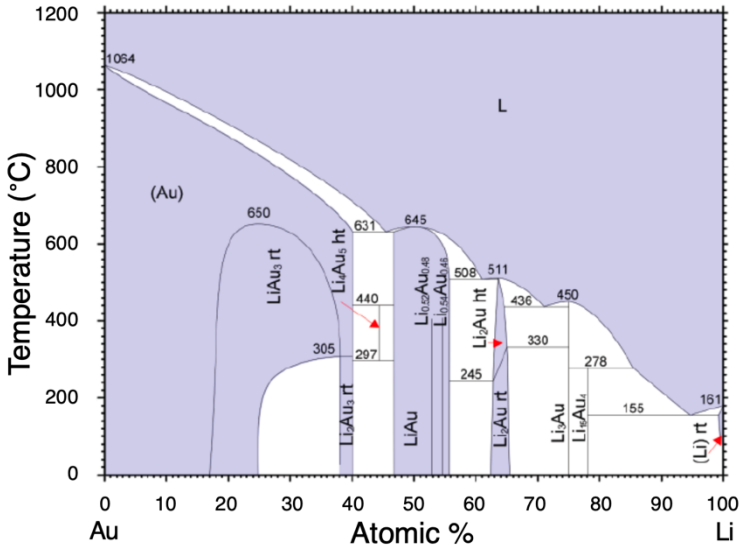

Figure 3.16 Phase diagram between Au and Li. Adapted with permission from reference [54]. Copyright 2016 Springer Nature.

An ultra-high vacuum (UHV) dielectric sputtering system (Orion-8, AJA) shown in Figure 3.17a was used to uniformly coat ~50 nm of Au on the surface of carbon microlattices. However, this system is designed for thin film coatings on flat substrates. To coat our 3D

samples, a customized sample holder was designed and printed using a DLP 3D printer (Titan 3, MicroSLA) with a commercially available photoresin (UHR, MicroSLA). Figure 3.18 shows a small size carbon lattice mounted on the sample holder with the Cu/Ni wires. The samples with holder were taped onto a silicon wafer for sputter coating. The schematic in Figure 3.17b demonstrates the configuration of sample, substrate, and sputter targets in the chamber. A 2 inch Au target was placed in one of the side guns in the chamber, from which the Au plasma is shot at an angle to the sample. The rotating stage allows uniform coating on all surfaces of the lattice. Figure 3.19 shows the small 3D micro-architected carbon samples after Au coating.

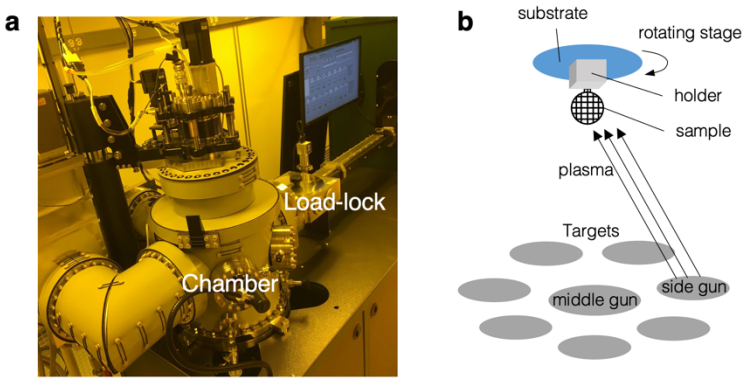

Figure 3.17 a) Optical image of the Orion-8 UHV sputtering system. b) Schematic of sample and target configurations of this system.

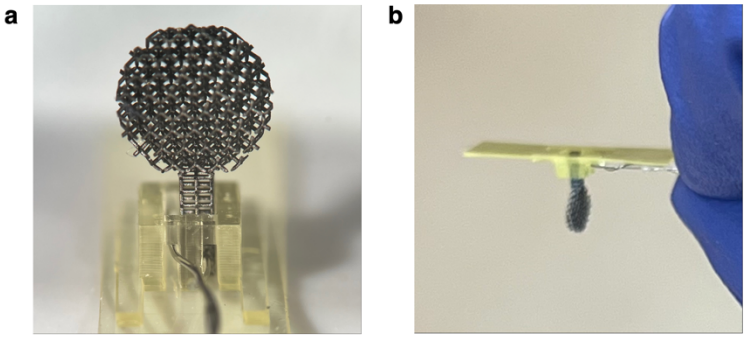

Figure 3.18 Optical images of a small 3D micro-architected carbon sample mounted on the 3D printed sample holder for sputter coating.

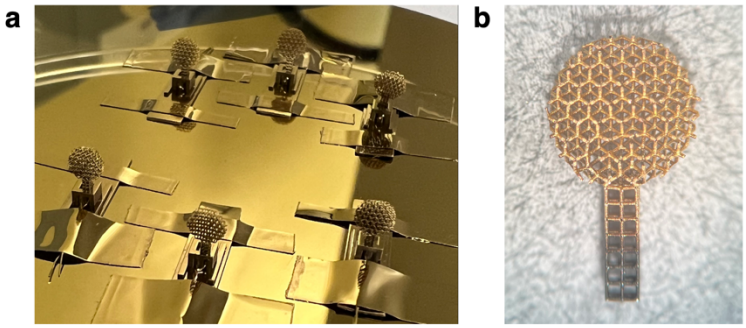

Figure 3.19 Optical images of small 3D micro-architected carbon samples a) mounted on the 3D printed sample holder and taped on a silicon wafer, and b) after removed from the holder.

A higher Ar pressure compared to normal Au sputtering procedures for thin film depositions in this system was used. This can cause more collisions between Au and Ar atoms within the Au plasma, resulting in highly randomized Au atom trajectories at the sample surface. For 3D structures, a highly directional plasma will result in thicker coatings on certain sample surfaces and insufficient coatings on the surfaces facing other directions. The key parameters for the Au sputtering process are listed in Table 3.3.

	DC Mode	**RF Mode**
Reaction gas	Ar	Ar
Gas flow rate	30 sccm	30 sccm
Strike pressure	30 mTorr	30 mTorr
Strike power	30 W	30 W
Running pressure	30 mTorr	30 mTorr
Running power	100 W	120 W
Running time	720 s	900 s

Table 3.3 Key parameters for the Au sputtering process.

Around 500 nm of Au was uniformly coated on the surface of 3D micro-architected carbon lattices. Afterwards, the sample was electrodeposited with 5 mA direct current for 30 minutes. Compared to the sample without Au coating shown in Figure 3.14, lithium on this sample shows a more uniform overall distribution, indicating more lithium nucleation sites

throughout the lattice. However, the lithium grew in a highly mossy morphology as shown in Figure 3.20, which is still far from the dense lithium layer we desire.

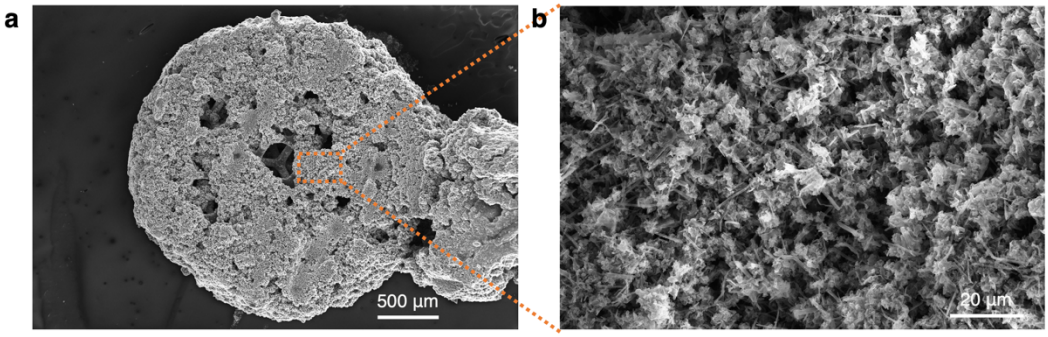

Figure 3.20 SEM images of a 3D micro-architected carbon lattice with Au coating after Li electrodeposition with 5 mA direct current for 30 minutes.

Potentially, the mossy lithium plating is due to the loose Au coating on the surface of carbon. When the sample is immersed into the electrodeposition solution, a large amount of Au floats away from the sample surface, with only scattered Au pieces or nanoparticles remaining on the carbon lattice. These Au particles trigger the heterogeneous nucleation of Li at many scattered sites when the current is applied, and as a result, Li grows into loose and highly mossy clusters.

First principles calculations of the interfaces between a metallic layer and two representative carbon substrates, in this case graphite and diamond, show significantly smaller work of separation for Au compared to Ti and Cr on both carbon substrates, as shown in Figure 3.21 [55]. The work of separation between two materials is calculated as

$$W_{sep}^{1-2} = \sigma_1 + \sigma_2 - \sigma_{12}$$

where σ_1 and σ_2 are surface energies of materials 1 and 2, and σ_{12} is the interface energy between them. The small work of separation for Au-carbon interface indicates low adhesion of Au on carbon substrates. Therefore, to maintain a uniform Au coating on the surface of

3D micro-architected carbon samples during the entire electrodeposition reaction, an additional adhesion layer of Ti or Cr between Au and carbon is necessary.

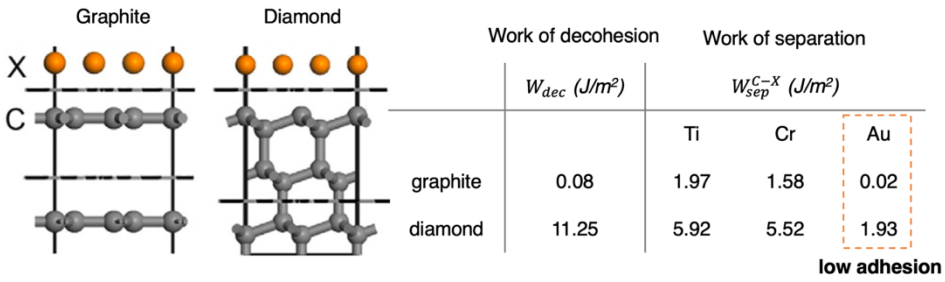

Figure 3.21 The adhesion strength of Ti, Cr and Au against graphite and diamond, from first principles calculations. Adapted with permission from reference [55]. Copyright 2010 Elsevier.

Figure 3.22 compares Ti and Cr as the adhesion layer between Au and SiO_2 substrate, which shows a clear Ti layer below Au but highly overlapping Cr and Au layers due to a strong interdiffusion between the two [56]. Since Ti has a higher work of separation than Cr for both graphite and diamond substrates and limited interdiffusion with Au, a ~5 nm Ti layer was sputtered as an adhesion layer to improve the stability of Au coating on carbon microlattices. The key parameters for the Ti sputtering process are listed in Table 3.4. Au is sputtered after Ti without breaking the vacuum to avoid oxidation of Ti.

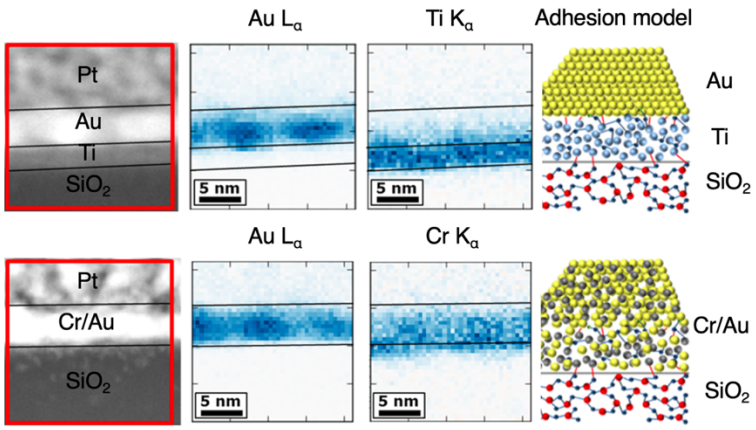

Figure 3.22 STEM-EDX maps of the Au layer on SiO_2 with Ti or Cr as the adhesion layer, with corresponding adhesion layer models. Adapted with permission from reference [56]. Copyright 2017 American Chemical Society.

	DC Mode	RF Mode
Reaction gas	Ar	Ar
Gas flow rate	30 sccm	30 sccm
Strike pressure	30 mTorr	30 mTorr
Strike power	30 W	30 W
Running pressure	20 mTorr	20 mTorr
Running power	150 W	150 W
Running time	1800 s	3000 s

Table 3.4 Key parameters for the Ti sputtering process.

After Ti/Au coating, the carbon microlattices show significantly different behaviors after Li electrodeposition. With 5 mA direct current for 30 minutes, Li was deposited on the lattice beams and also filled most of the empty volume in the lattice, as shown in Figure 3.23a, instead of only on the outer surface of the cylindrical disk as shown in Figure 3.14. For the electrode to start with lower initial mass and larger empty volume for Li storage in a battery before charging, the 5 mA direct current deposition was reduced from 30 minutes to 15 minutes, which allowed Li to be deposited only on the lattice beams without filling the pores (Figure 3.23b). A deposition of 10 minutes, as shown in Figure 3.24, achieved an even thinner Li layer, with smooth surface on most areas but a rougher morphology on some lattice beams (Figure 3.24).

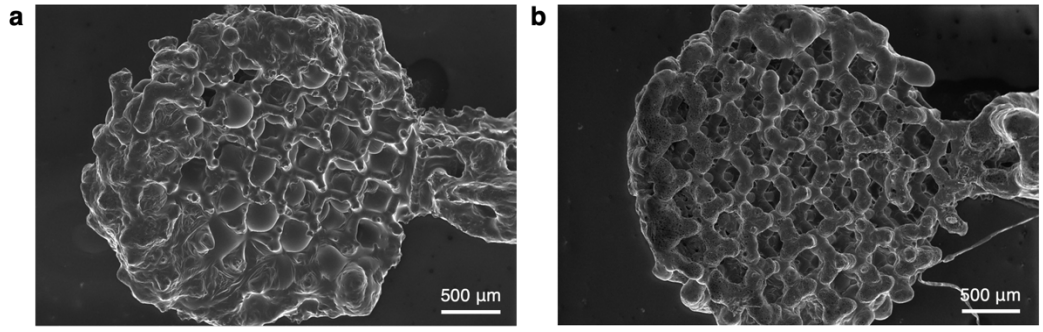

Figure 3.23 SEM images of a 3D micro-architected carbon lattice with Ti/Au coating after Li electrodeposition with 5 mA direct current a) for 30 minutes and b) for 15 minutes.

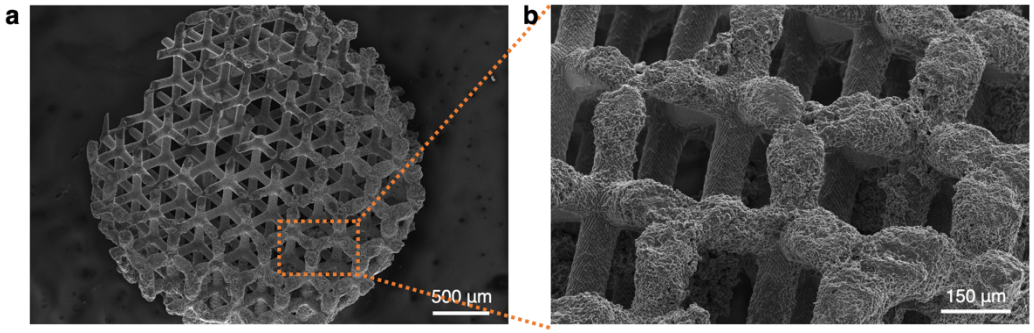

Figure 3.24 SEM images of a 3D micro-architected carbon lattice with Ti/Au coating after Li electrodeposition with 5 mA direct current for 10 minutes.

To further improve the surface morphology of electrodeposited Li, the carbon microlattice with Ti/Au coating was applied with 5 mA pulse current, with 1 second on and 1 second off, for 30 minutes of the total pulse-on time. The pulse current allows for Li ion diffusion during the off periods to replenish at the electrode surface and helps maintain a consistent ion concentration across the surface. As shown in Figure 3.25, a thin and conformal layer of Li on the surface of the 3D lattice was achieved.

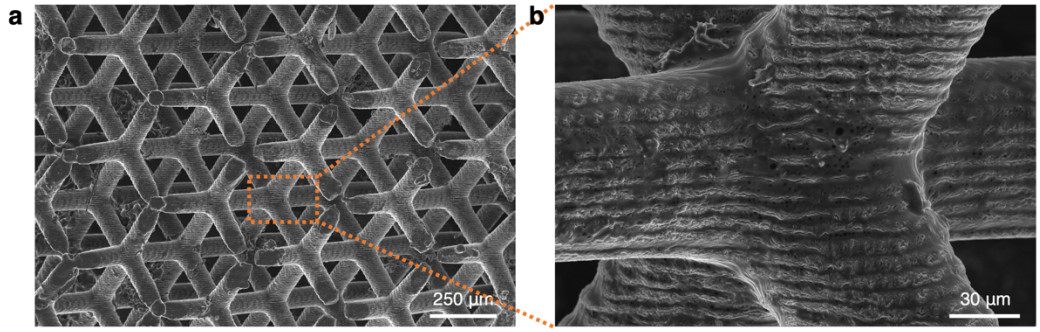

Figure 3.25 SEM images of a 3D micro-architected carbon lattice with Ti/Au coating after Li electrodeposition with 5 mA pulse current (on 1s, off 1s) for 30 minutes of the total pulse-on time.

For easier assembly of the 3D anode into a CR2032 coin cell for cycling experiments, larger 3D micro-architected carbon samples were fabricated and sputtered with Ti/Au following the same recipe. The large sample also has an overall shape of a cylindrical disk (Figure

3.6b), but is 6 mm in diameter. The maximum overall sample dimensions are limited by the size of the sputter's load-lock. Sputtering on even larger samples in this system can be achieved using alternative sample-loading methods. Figure 3.26 shows the large samples threaded with the Cu/Ni wires and taped onto a silicon wafer, and the results after Ti/Au sputtering. The coated large samples were prepared for Li electrodeposition similarly to the small samples, as summarized in Figure 3.27.

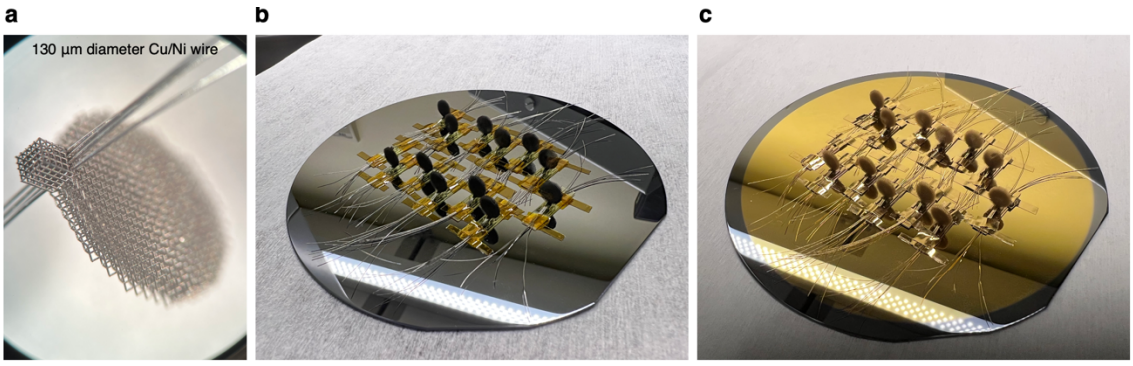

Figure 3.26 Optical images of a) a large 3D micro-architected carbon lattice with Cu/Ni wire threaded through the handle structure, and several large samples mounted in the 3D printed holders and taped on a silicon wafer b) before and c) after Ti/Au sputtering.

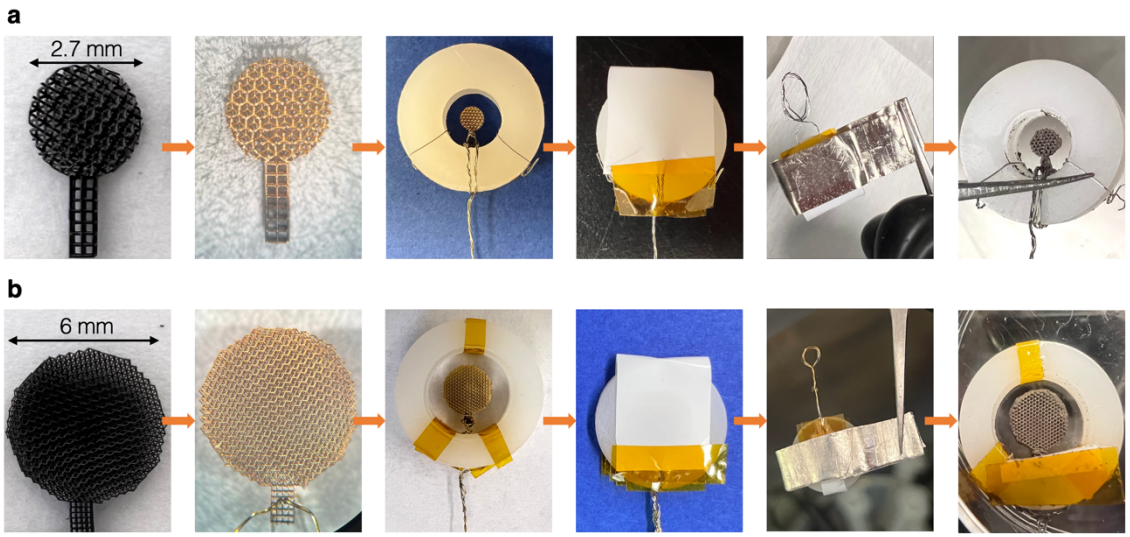

Figure 3.27 The fabrication process for small and large 3D micro-architected carbon/Li lattices.

The current for Li electrodeposition on the large samples was modified due to its different overall dimensions. 20 mA pulse current (26 mA cm^{-2} for surface area of the cylindrical disk with 6.0 mm diameter and 1.1 mm thickness), with 1 second on and 1 second off, for 30 minutes of the total pulse-on time was applied. The electrodeposited Li forms a uniform layer on the surface of the microlattice, as shown in Figure 3.28a. The beam diameter of the carbon lattice is 46 µm (Figure 3.9c), and after Li deposition, the beam diameter increases to around 50 µm. The thickness of Li layer is 4–5 µm, confirmed by measurements on a beam cross-section milled using Ga focused ion beam (Figure 3.28c). EDS mapping (Ga signal removed) in Figure 3.28d of the same cross-sectional area shows a clear interface between Au coating and carbon beam.

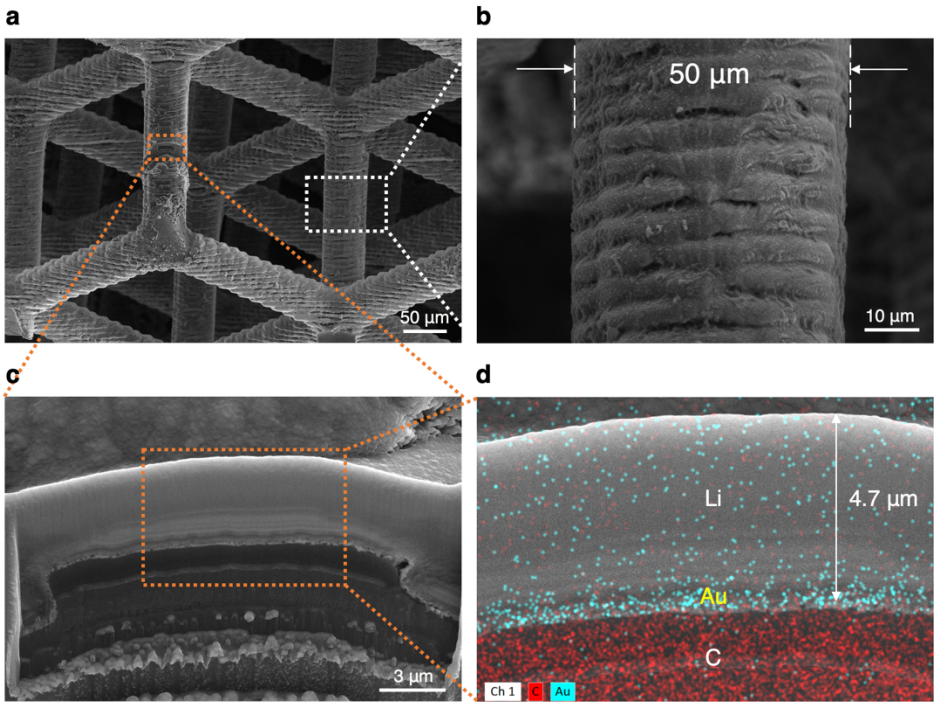

Figure 3.28 SEM images of a large 3D micro-architected carbon lattice with Ti/Au coating after Li electrodeposition with 20 mA pulse current (on 1s, off 1s) for 30 minutes of the total pulse-on time. a) A top-down view of the lattice. b) A close view of the beam. c) An area on the cross-section of a lattice beam cut with Ga FIB and d) a corresponding EDS mapping.

3.5 Cycling of 3D Micro-Architected Lithium/Carbon Electrode

The large 3D micro-architected lithium/carbon electrodes were assembled in the CR2032 coin cell against Li metal, with 1M $LiPF_6$ in 1:1 (v/v) ratio of ethylene carbonate (EC) and ethyl methyl carbonate (EMC) liquid electrolyte (battery grade; Sigma-Aldrich). The overall diameter of the microlattice is 6 mm and the thickness is 1.1 mm. An HDPE washer with a thickness of 1 mm was used to centrally position the 3D lattice and support the compressive stress from coin cell assembly. Other components of the coin cell are shown in Figure 3.29. For comparison, a coin cell with the 3D electrode replaced by a Li electrode with 6 mm in diameter and 0.75 mm in thickness, with all other components the same, was also assembled and tested.

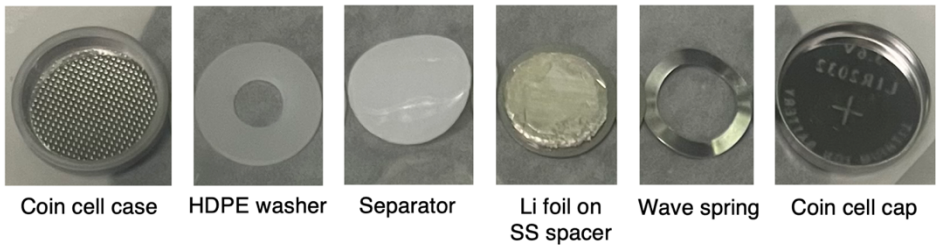

Figure 3.29 Optical images of CR2032 coin cell components for symmetric cycling experiments of 3D micro-architected lithium/carbon electrode.

Figure 3.30 displays the galvanostatic charge/discharge cycling performances of a 3D micro-architected lithium/carbon electrode and a Li metal electrode with 6 mm diameter, in symmetric batteries against Li foil, for 200 cycles. The corresponding Coulombic efficiency is shown on the bottom of the same figure. The electrodes were cycled to a capacity of 1 mAh cm^{-2} with a current density of 1.0 mA cm^{-2}, and the cutoff voltage is 2 V. The battery voltage decreases during the plating of lithium on the tested 3D lithium/carbon or Li metal electrode, and increases during the stripping. The counter Li metal electrode is much larger than the tested electrodes, therefore experiences a much smaller current density, which leads to the highly asymmetric voltage above and below zero during cycling. The 3D electrode has a voltage hysteresis of around 0.5 V for its lithium stripping throughout 200 cycles. The Li

metal electrode with 6 mm diameter shows a lower voltage hysteresis of around 0.2–0.3V, slowly increasing with longer cycling, before cycle number 163. However, around cycle 163, the Li electrode experienced a rapid increase in voltage hysteresis, and kept hitting the cutoff voltage of 2 V in the rest cycles. Due to the termination of cycling step at the cutoff voltage, less lithium was stripped from the Li electrode than the amount plated in the previous step, giving <100% Coulombic efficiencies in the cycles after 163, which fluctuated around 10%–50%.

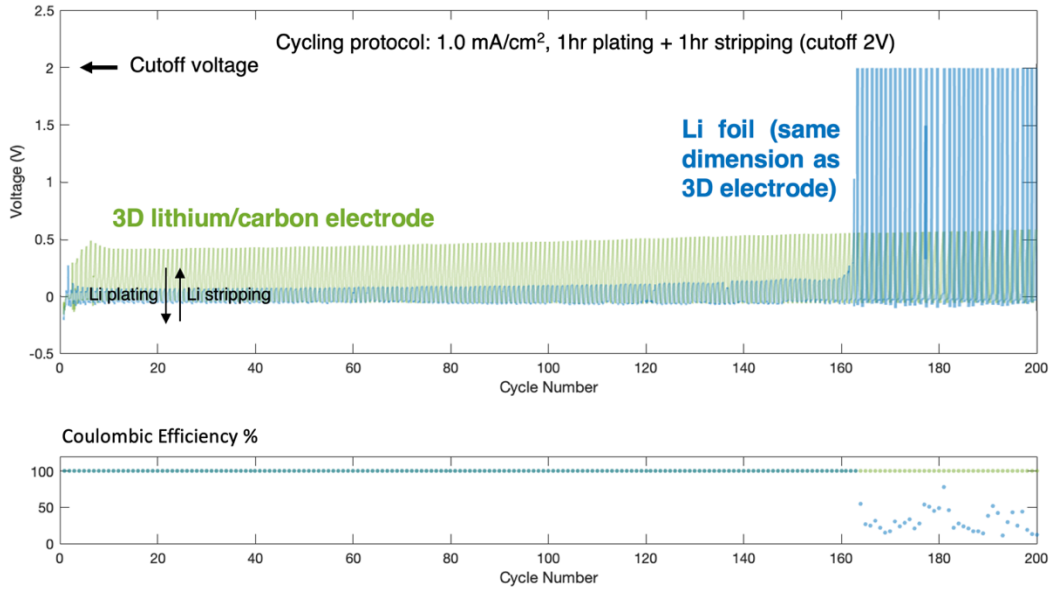

Figure 3.30 Cycling performance of 3D micro-architected Li/carbon electrode and Li electrode with the same 6 mm diameter as 3D electrode, in symmetric batteries against Li foil, with a capacity of 1 mAh cm^{-2} and a current density of 1.0 mA cm^{-2}.

To characterize the morphology of the electrodes after 200 cycles and to investigate the main cause for the abrupt failure of the Li electrode around cycle 163, the cycled coin cells were opened in an Ar glovebox, and the electrodes were transferred to SEM for imaging using the Vacushut (Figure 3.13). From the optical images of the Li electrode before and after 200 cycles (Figure 3.31a), a significant change in color was observed. SEM images (Figure 3.31c) show many cracks and partial detachment at the edge from the stainless steel spacer substrate, with mossy lithium morphology throughout the whole electrode. The rapid

increase in voltage hysteresis after 163 cycles may potentially be caused by the extensive formation of mossy lithium on the bottom of the lithium metal when it became partially detached from the substrate due to the cracking and deformation. Such failures would result in a significant increase of interface resistance between the electrode and substrate.

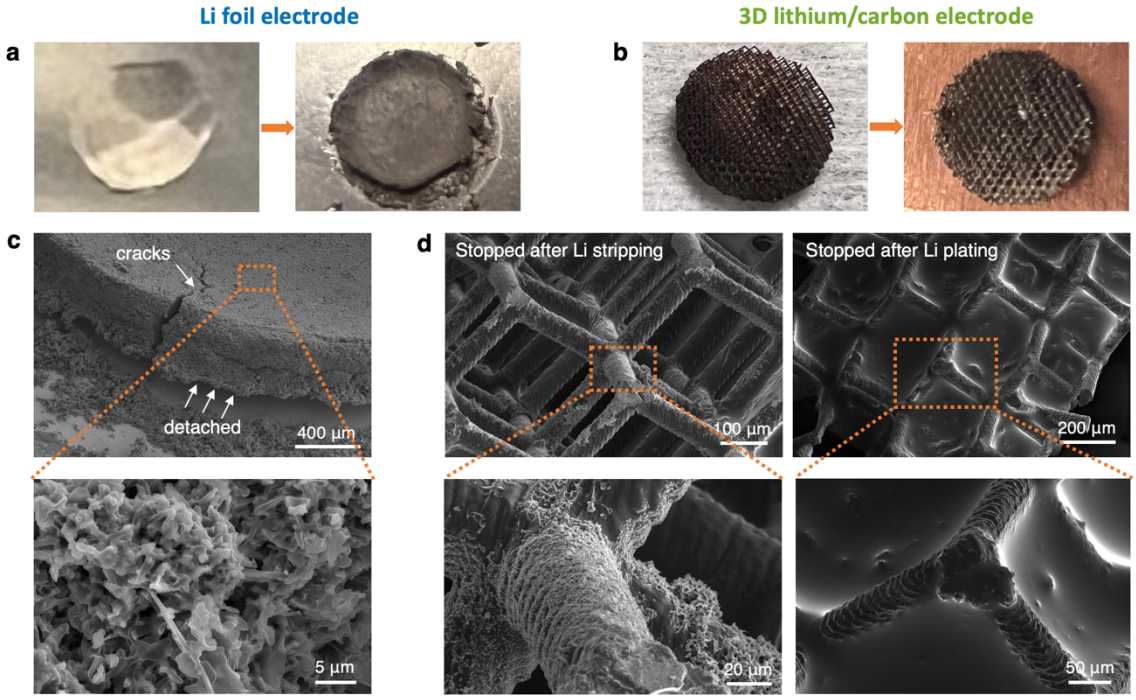

Figure 3.31 Optical images of a) Li foil electrode (6 mm diameter) and b) 3D micro-architected lithium/carbon electrode before and after 200 cycles. SEM images of c) Li foil electrode and d) 3D micro-architected lithium/carbon electrode after 200 cycles.

The 3D lithium/carbon electrode mainly appeared the same after 200 cycles, as shown in Figure 3.31b, with a small amount of mossy Li remaining on the surfaces of lattice beams (Figure 3.31d). In a sample that received one additional plating step (200 cycles plus a plating step), some of the cubic unit cells were filled with lithium, while others remained empty. The lithiation capacity of 1 mAh cm^{-2} during cycling was much smaller than the theoretical capacity of the 3D electrode. Assuming all empty volume in the lattice is utilized for lithium storage during cycling, with 50 µm beam diameter, 250 µm unit cell and 1.1 mm thickness, the theoretical capacity of this electrode is around 150 mAh cm^{-2}.

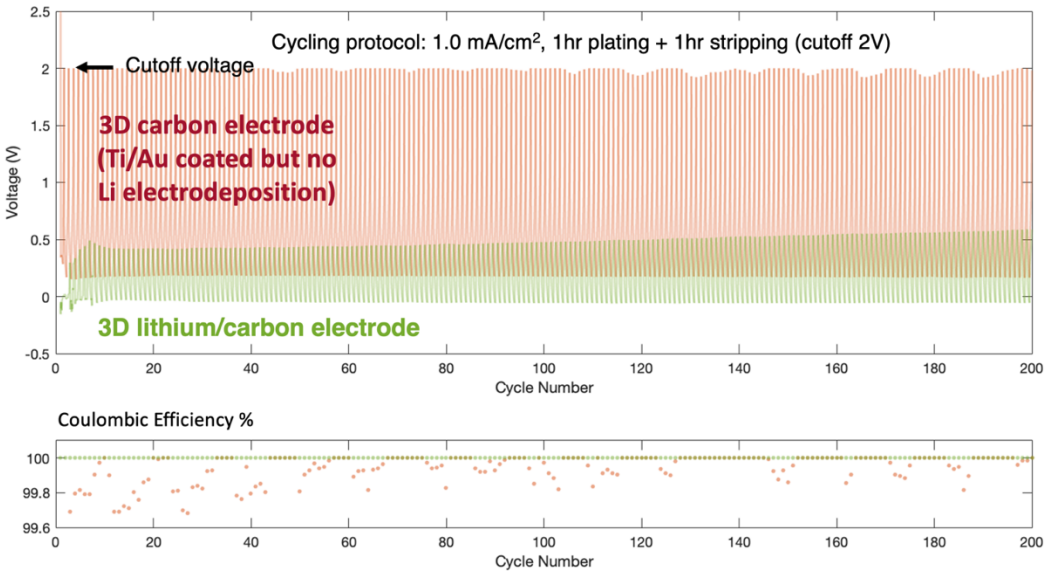

Figure 3.32 Cycling performance of 3D micro-architected carbon electrode with Ti/Au coating in comparison with 3D micro-architected Li/carbon electrode, in symmetric batteries against Li foil, with a capacity of 1 mAh cm^{-2} and a current density of 1.0 mA cm^{-2}.

To highlight the necessity of Li electrodeposition on the carbon microlattice prior to cycling, a 3D micro-architected carbon electrode with Ti-Au coating was assembled in a coin cell for cycling in the same way as the 3D micro-architected Li/carbon electrode. Figure 3.32 displays the galvanostatic charge/discharge cycling performances and the corresponding Coulombic efficiency, in comparison with the Li/carbon electrode. The Ti-Au coated carbon electrode without Li electrodeposition started hitting the cutoff voltage of 2 V from the first cycle, giving a <100% Coulombic efficiency, and its voltage hysteresis maintained at around 2 V throughout 200 cycles. The significantly higher voltage hysteresis of the carbon electrode compared to the Li/carbon electrode is due to the lack of lithium on the electrode before cycling to compensate for the irreversible lithium loss as a result of solid electrolyte interface (SEI) or "dead" lithium formation during cycling.

The 3D micro-architected lithium/carbon electrode was assembled in a CR2032 coin cell against a $LiCoO_2$ (LCO) slurry electrode (94% wt% BTR LCO, 2 wt% Timcal C45, 4 wt% Solvay 5130 PVDF; CAMP Facility), with 1M $LiPF_6$ in a 1:1 (v/v) ratio of EC:EMC liquid electrolyte. The LCO slurry coating has a porosity of 32.4%, a thickness of 47 μm and LCO

loading of 13.6 mg cm^{-2}. The total mass of LCO on the 5.56 mm diameter disk electrode is 3.30 mg. Figure 3.33 shows all coin cell components. For comparison, a coin cell with the 3D electrode replaced by a Li foil electrode with 6 mm in diameter and 0.75 mm in thickness, with all other components the same, was also assembled and tested.

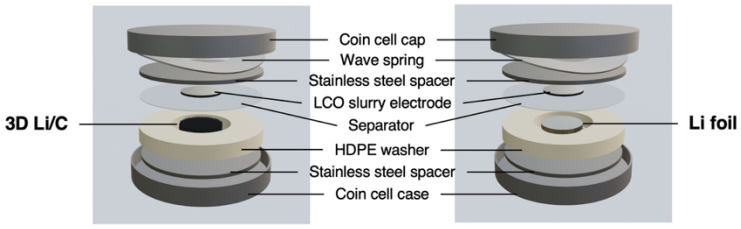

Figure 3.33 Schematics coin cell components for cycling experiments of 3D micro-architected lithium/carbon electrode and lithium foil electrode against LCO slurry cathode.

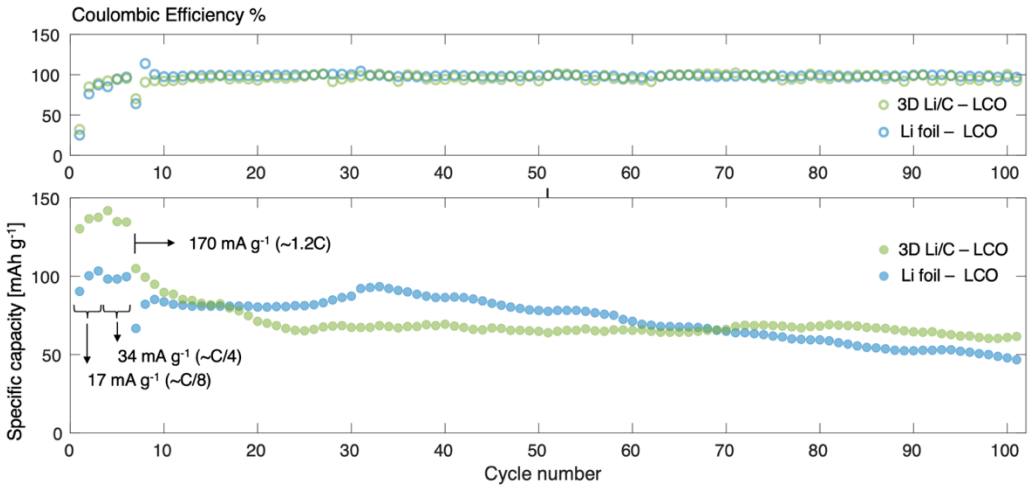

Figure 3.34 Coulombic efficiency (top) and discharge specific capacities (bottom) of 3D Li/C anode and Li foil anode against LCO cathodes cycled between 3.0 and 4.2 V at different current densities.

The discharge capacities and the corresponding Coulombic efficiencies at 17 mA g^{-1} (~C/8), 34 mA g^{-1} (~C/4) and 170 mA g^{-1} (~1.2C) for the two cells are shown in Figure 3.34. All current densities and C-rates are based on LCO mass, assuming a practical capacity of 140 mAh g^{-1}. CCCV charging with 0.02 mA cutoff current and CC discharging were employed. The 3D anode outperformed the Li foil anode at C/8 and C/4. When the current density was

switched to 1.2C, capacities of both cells experienced a rapid drop due to Li ion diffusion limitations. Capacity of the cell with 3D anode decreased within 20 cycles at the high current and became lower than the Li foil cell, but then stayed consistent for the rest 80 cycles. The cell with Li foil anode, in contrast, showed a stable capacity in the first 30 cycles, but then experienced a continuous capacity fade afterwards until the end of the cycling experiment.

The mechanically robust 3D micro-architected carbon scaffolds support lithium plating and maintain good contact with the coin cell case during long-term cycling experiments. While mossy and dendric lithium morphologies were observed on the surface of Li metal foil electrodes, a smooth lithium surface morphology was observed to fill free space in the architected lattice. This difference is potentially due to a distinct lithium growth mechanism when interacting with the carbon scaffold with Ti/Au coating, as a result of a different electric field near the electrode, and a smaller effective areal current density on the surface of the microlattice. In situ observation of the lithium plating and stripping mechanisms on this 3D micro-architected carbon lattice, using optical microscopy and customized in situ cells (Figure 3.33), will be interesting for future studies.

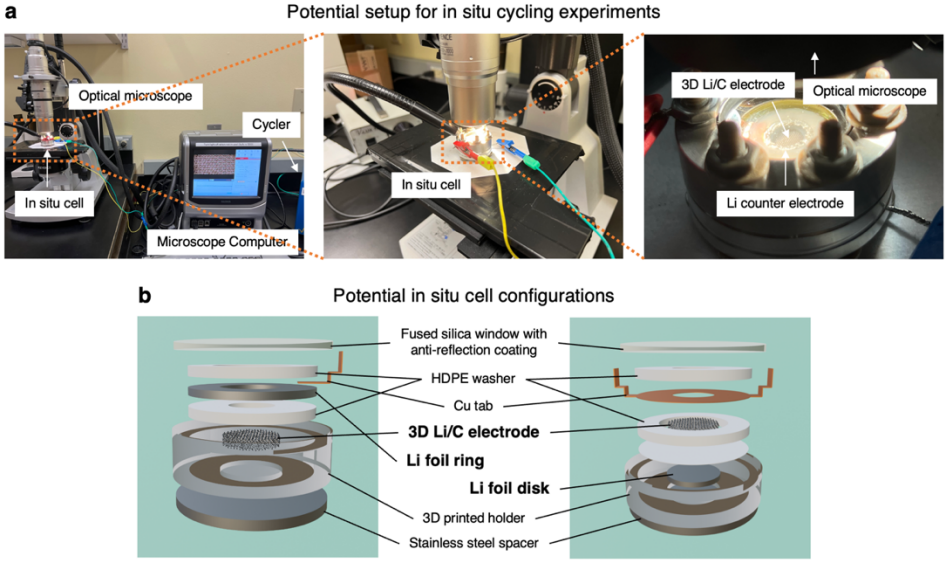

Figure 3.35 Potential designs for in situ optical study of lithium platting and stripping on the 3D micro-architected lithium/carbon electrode. a) Experimental setup. b) Potential cell configurations for in situ cycling experiments.

Chapter 4

SUMMARY AND OUTLOOK

4.1 Summary

This thesis introduces two new methodologies to fabricate 3D micro-architected electrode materials for lithium-ion batteries. The first highlights an innovative technique to fabricate 3D micro-architected LCO through gel infusion additive manufacturing, which combines VP 3D printing with a gel infusion and calcination process. This process utilizes a customized acrylate-based photoresin and a DLP 3D printer to print a blank organogel microlattice, which is transformed into a hydrogel through solvent exchange and then infused with lithium and cobalt precursors. The infused gel undergoes calcination to synthesize the 3D LCO microlattice. This technique achieves 3D LCO microlattices with beam diameters of 45 μm and maintains the designed architecture with tunable microstructures. Thermal, mechanical and electrochemical analysis demonstrate the method's effectiveness in producing LCO microlattices with promising mechanical and electrochemical properties. By fabricating 3D micro-architected NMC111 through a very similar process, we demonstrate the potentials to apply this gel infusion additive manufacturing method in a variety of cathode materials for lithium-ion batteries in 3D.

The second methodology introduces the fabrication of a 3D lithium anode using a micro-architected carbon scaffold. The additive manufacturing of 3D micro-architected carbon lattices via pyrolysis from 3D printed polymer microlattices enables the creation of mechanically robust carbon electrodes with micro-scale feature sizes and flexible structural control, making them suitable as scaffolds for lithium-metal anodes. Surface functionalization and lithium electrodeposition conditions are explored for dense lithium nucleation and uniform epitaxial growth on the carbon microlattice. Symmetric cycling experiments of 3D micro-architected lithium/carbon electrodes reveal promising

performance, with the 3D electrode demonstrating a consistent voltage hysteresis across 200 cycles.

The development of these fabrication techniques for micro-architected electrode materials unlocks new possibilities for fully three-dimensional batteries, such as the 3D interdigitated battery and the 3D interpenetrated battery designs proposed in the outlook. In addition to constructing 3D batteries, the micro-architected electrodes also open new pathways for the exploration of micro-architected flow systems in many applications, such as the water filtration system for lithium ion recycling and the flow cells for electrocatalytic CO_2 reduction.

4.2 Outlook: Future Applications of 3D Micro-Architected Electrode Materials

4.2.1 3D Interdigitated Lithium-Ion Batteries

As introduced in Chapter 1, 3D batteries with the interdigitated-plate configuration have been successfully created through DIW, with both cathode and anode inks extruded onto a substrate to form stacked filaments, achieving up to 16 layers and giving a maximum height-to-thickness ratio of 8:1 for the electrode plates [16,17]. Higher stackings remain challenging due to the viscoelastic nature of the inks. Advancements in VP-based AM techniques now offer significantly enhanced design flexibility for 3D electrodes, allowing for more intricate micro-scale structures, such as horizontally oriented beams, to be precisely fabricated.

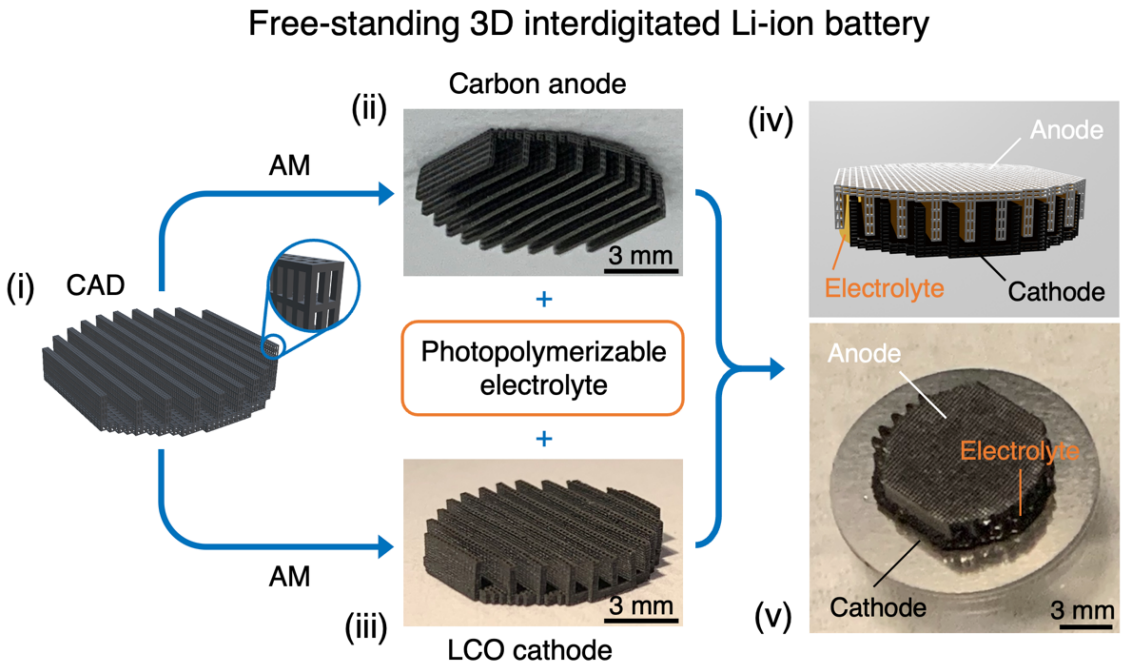

Figure 4.1 Free-standing 3D interdigitated lithium-ion battery with additively manufactured LCO cathode and carbon anode. (i) CAD of a 3D electrode with interdigitated-plate configuration. Optical images of (ii) carbon anode and (iii) LCO cathode fabricated into the corresponding structure. (iv) Schematic and (v) optical image of the assembled 3D battery.

We propose a novel free-standing 3D interdigitated Li-ion battery design where both electrodes are structured as interdigitated plates, composed of beams ranging from 50 to 70 µm in diameter, as depicted in Figure 6b. The carbon anode is produced following a VP 3D printing and pyrolysis method introduced in Chapter 3.2, while the LCO cathode was fabricated through the AM technique demonstrated in Chapter 2 [24]. The designs of these electrodes are similar and complementary (Figure 4.1(i-iii)). Figure 4.2 shows the anode and cathode in each stage of their fabrication. The surface of the LCO cathode is coated with a photopolymerizable gel polymer electrolyte resin, which also fills the free volume in each plate via capillary action, followed by UV curing. Subsequently, the carbon anode is integrated, with additional electrolyte resin filling any remaining gap space between electrodes before final curing. Figure 4.1b(iv) illustrates a schematic of the assembled fully 3D battery, with Figure 4.1b(v) providing an optical image of the actual sample. A significant challenge in this design is ensuring the resin thoroughly permeates the empty volumes in the plates and forms a uniform layer on their surfaces, without overfilling the interspace between adjacent LCO electrode plates, requiring precise viscosity control of the electrolyte resin. Despite this challenge, the free-standing 3D interdigitated batteries display high active material mass loading and minimized ion transport distances, and thus show promise in breaking the conventional compromise between energy density and power density in energy storage technologies [57,58].

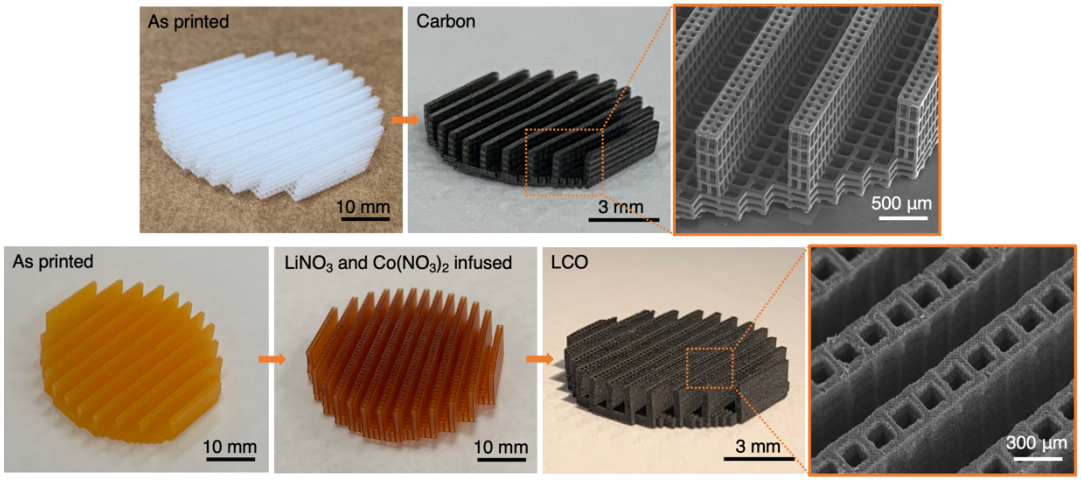

Figure 4.2 Fabrication of 3D interdigitated carbon anode and LCO cathode.

4.2.2 3D Interpenetrated Lithium-Ion Batteries

Additive manufacturing enables the fabrication of interpenetrated microlattices, which are very challenging to fabricate with techniques other than additive manufacturing due to their high structural complexity. We propose a method to create 3D lithium-ion batteries with interpenetrated cathode and anode lattices using VP 3D printing of a nonconductive ceramic material, followed by sputter coating of conductive layers and electrodeposition of cathode and anode active materials. 3D cathode and anode in this design are fixed for their relative positions, making for easier cell assembly compared to the previous interdigitated batteries with free-standing cathodes and anodes separately.

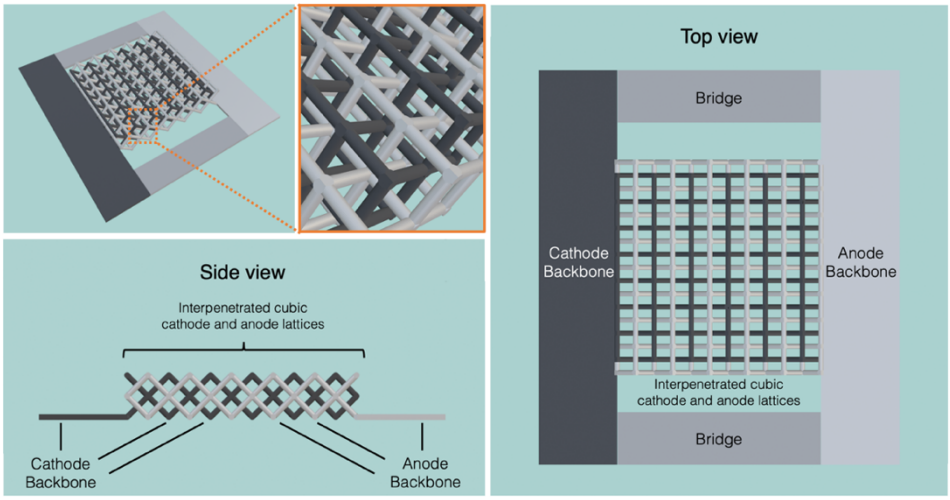

Figure 4.3 Schematic of a 3D interpenetrated lattice as the backbone of 3D interpenetrated lithium-ion battery.

Schematics in Figure 4.3 show the design for a 3D interpenetrated lattice as the backbone of 3D interpenetrated battery, using cubic lattices for demonstration. The dark and light grey parts are two cubic lattices which are interpenetrated into each other without contact. They are each connected to a thin plate on two opposite sides of the lattice, shown with the same color, and the two plates are connected to each other with bridging plates on the rest two sides. By VP 3D printing using a ceramic resin containing ceramic nanoparticles such as SiO_2 and Al_2O_3, followed by a high-temperature process to remove organic components in

the 3D structure and sinter the ceramic nanoparticles, a nonconductive and mechanically robust ceramic interpenetrated structure should be obtained. The two bridges on the structure are covered before sputtering of a conductive metal layer such as Au, potentially with a Ti adhesion layer, to give a conformal coating on the surface of the lattices. Each lattice becomes electrically conductive due to the metal coating, while the two interpenetrated lattices are insulated from each other due to the absence of coating on the bridges. Afterwards, one lattice will be electrodeposited with a cathode material such as LCO [59], while the other lattice would be electrodeposited with an anode material such as lithium. The two interpenetrated electrode microlattices are connected by the insulating bridge so their relative positions are fixed, and therefore the two electrodes will not be in contact during the entire fabrication process. A solid-state electrolyte should then be filled into the empty space between lattices. The electrolyte will provide ionic conductivity and serve as an electronically insulating barrier between electrodes. By carrying out the aforementioned process, one would fabricate a full solid-state battery with interpenetrated electrodes.

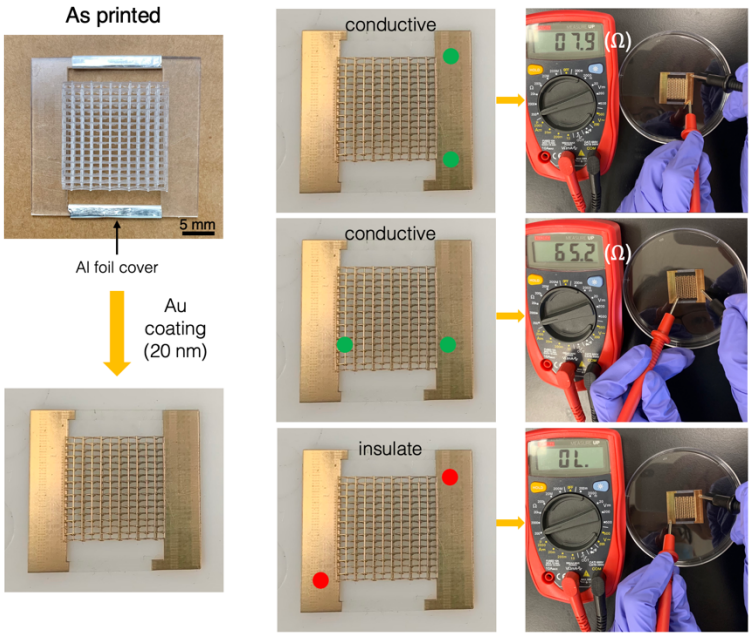

Figure 4.4 A printed polymer interpenetrated lattice before and after Au sputtering, and the results of conductivity measurements between different parts.

We demonstrated the feasibility of this design using a 3D interpenetrated polymer structure printed with PR-48 photoresin, as shown in Figure 4.4. The bridges were covered with aluminum foil and then the sample was sputtered with 20 nm Au. After removing the foil covers, the conductivity for a single lattice and the conductivity between the two interpenetrated lattices were measured, giving a finite resistance for the former and an out-of-range resistance for the latter. One lattice of the Au-coated sample was electroplated with Ni in a Watts bath [60] while the other lattice remained unchanged, as shown in Figure 4.5. The deposition of Ni on only one of the interpenetrated lattices indicates each electrode can be individually electrodeposited to achieve a full 3D interpenetrated battery.

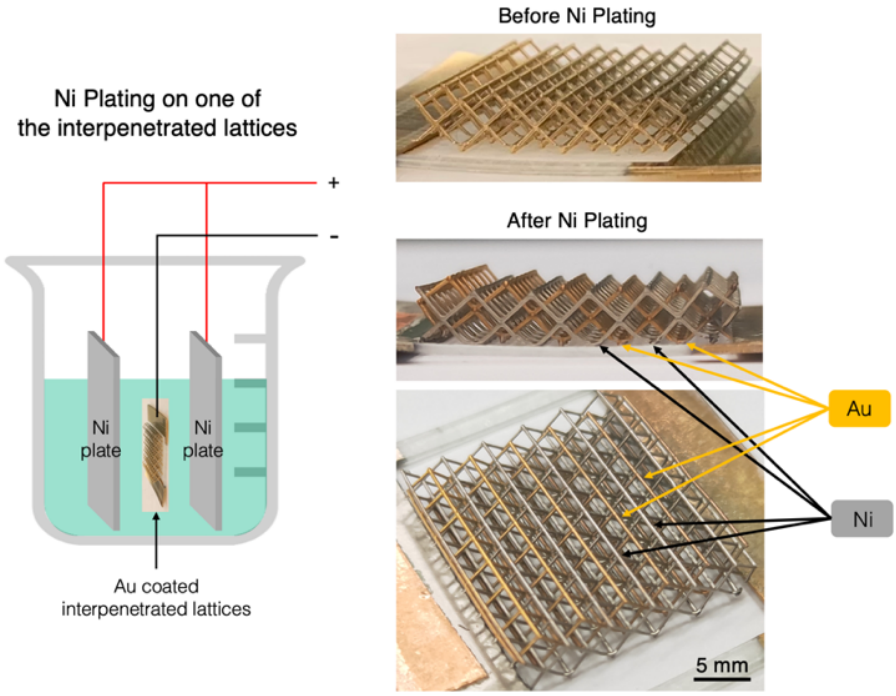

Figure 4.5 Ni plating on one of the interpenetrated lattices after Au coating.

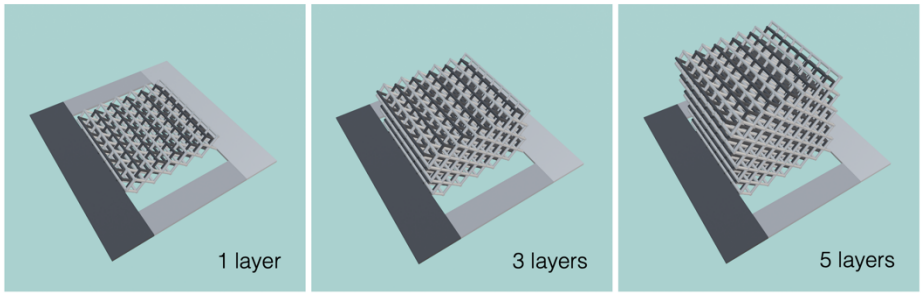

Figure 4.6 Scaling up of the interpenetrated battery design by adding layers in the additively manufactured microlattice backbones.

The layer-by-layer printing mechanism for the fabrication of interpenetrated microlattice backbones in this design enables straightforward scaling up of the 3D battery, simply by adding layers to the lattices in the CAD model, as demonstrated in Figure 4.6. With further advancements in high-resolution additive manufacturing techniques in the future, 3D batteries with micro-scale or even nano-scale architected features to achieve both higher energy and power densities will be interesting to pursue.

4.2.3 3D Micro-Architected Electrode Materials for Lithium Ion Recycling and Electrocatalytic CO_2 Reduction

In addition to constructing fully three-dimensional batteries, the techniques to architect electrode materials in 3D with micro-scale form factors open new pathways for the exploration of micro-architected flow systems for many applications. The gel infusion additive manufacturing technique to fabricate 3D architected cathode materials for lithium-ion batteries, for example, can be used to build 3D filtering systems for lithium ion recycling from wastewater or seawater. There are pioneering studies on selective electrochemical extraction of lithium ions from water with a high concentration of sodium ions, which is the major ion in competition with lithium, using delithiated $LiCoO_2$ or $LiFePO_4$ slurry electrodes [61,62]. By replacing the 2D slurry electrodes with 3D micro-architected electrodes, the electrode surface area can be maximized to achieve higher lithium ion extraction efficiency for the recycling system.

Additive manufacturing enables the fabrication of 3D architected carbon electrodes with flexible form factors and well-defined geometries, as shown in Figure 4.7, and these carbon electrodes can be potentially used to construct flow cells for electrocatalytic CO_2 reduction.

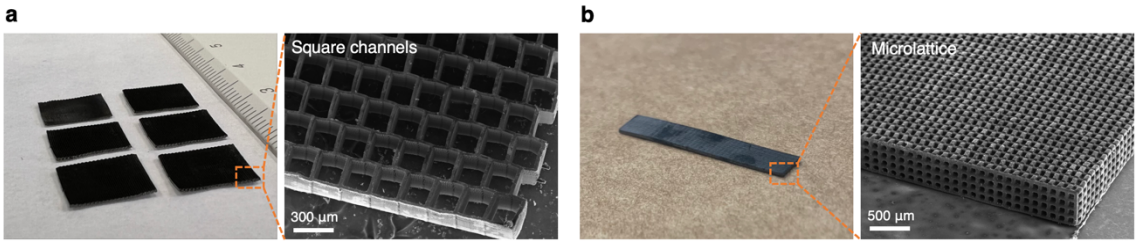

Figure 4.7 Potential designs of 3D micro-architected carbon electrodes for electrocatalytic CO_2 reduction with a) square channels and b) cubic unit cells.

Copper, one of the most promising catalysts for the reduction of CO_2 to products beyond CO [63], can be deposited on the surface of the architected carbon electrodes. Figure 4.8a shows the micro-architected carbon electrodes with square channels mounted on a silicon wafer before and after sputter coating. A Ti/Au/Cu trilayer was sputtered on the carbon electrodes for demonstration, with ~5 nm Ti as an adhesion layer, ~10 nm Au as a substrate layer, and ~30 nm Cu as the catalyst layer. The hydrodynamics of the system and the transport of the dissolved species through the architected electrodes can be modeled using multiphysics simulation to achieve rational designs, for example by optimizing the pore size, varying the electrode thickness, or adding turbulence-enhancing structures to alter the retention time of the reaction intermediates on the electrode (Figure 4.8b) [64]. Such simulation-guided structural optimization can be realized by the additively manufactured carbon electrodes in a much easier way than the porous carbon paper with stochastic 3D structures, commonly used in electrocatalytic CO_2 reduction experiments. Using rational electrode designs, it will be possible to tune the selectivity of CO_2 reduction towards multi-carbon products such as ethylene and ethanol. The rigid nature of these additively manufactured carbon electrodes is a challenge for incorporating them into the typical flow cells, which usually contain flexible carbon paper electrodes (Figure 4.8c(iii)) [65]. This issue can be solved by mounting the 3D electrode between two flexible polypropylene (PP) sheets with hollow rectangle windows,

as shown in Figure 4.8c, for it become compatible with typical flow cell designs. It will be interesting to explore the selective CO_2 reduction using 3D micro-architected carbon electrodes with the guidance from simulations.

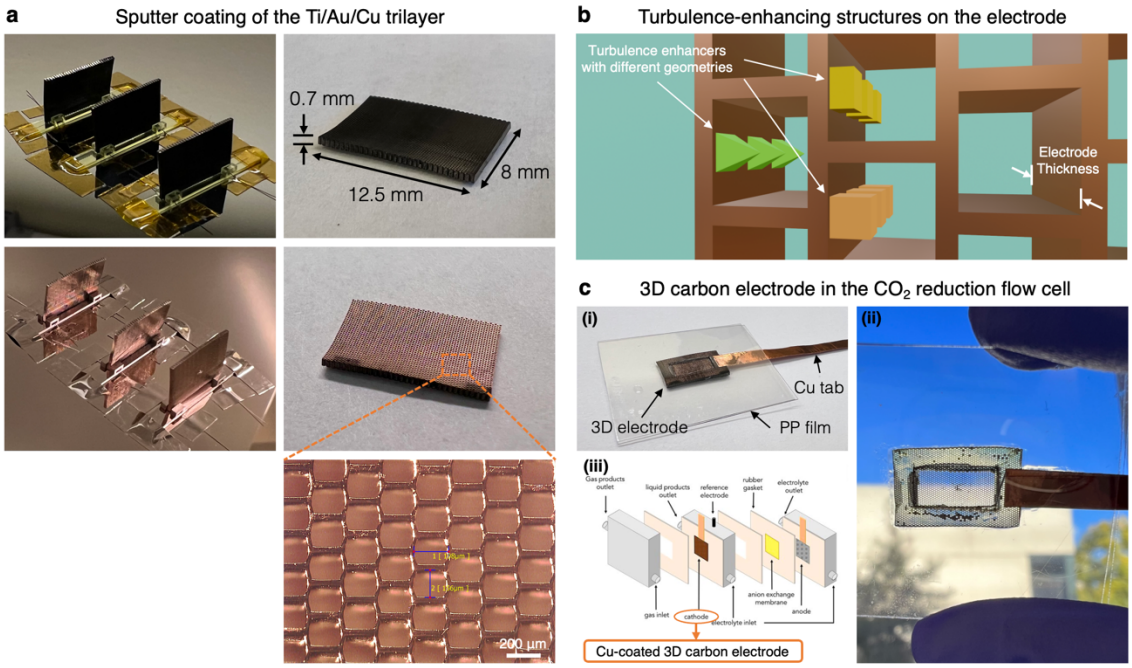

Figure 4.8 3D micro-architected carbon electrodes for electrocatalytic CO_2 reduction experiments. a) Carbon electrodes with square channels mounted on a silicon wafer before and after sputter coating. b) Schematic of potential turbulencc enhancing structures on the architected carbon electrode. c)(i)–(ii) Preparation of the architected carbon electrode for (iii) a typical flow cell design. c(iii) in this figure is adapted with permission from reference [65] under open-access CC-BY license.

BIBLIOGRAPHY

[1] Y. Liang, C. Zhao, H. Yuan, Y. Chen, W. Zhang, J. Huang, D. Yu, Y. Liu, M. Titirici, Y. Chueh, H. Yu, Q. Zhang, *InfoMat* **2019**, *1*, 6-32.

[2] N. Wassiliadis, J. Schneider, A. Frank, L. Wildfeuer, X. Lin, A. Jossen, M. Lienkamp, *J. Energy Storage* **2021**, *44*, 103306.

[3] T. Kim, W. Song, D. Son, L. K. Ono, Y. Qi, *J. Mater. Chem.* **2019**, *7*, 2942.

[4] B. Dunn, H. Kamath, J. Tarascon, *Science* **2011**, *334*, 928.

[5] F. C. Krause, J. P. Ruiz, S. C. Jones, E. J. Brandon, E. C. Darcy, C. J. Iannello, R. V. Bugga, *J. Electrochem. Soc.* **2021**, *168*, 040504.

[6] M. S. Whittingham, *Science* **1976**, *192*, 1126.

[7] K. Mizushima, P. C. Jones, P. J. Wiseman, J. B. Goodenough, *Mater. Res. Bull.* **1980**, *15*, 783.

[8] N. Sick, O. Kratzig, G. G. Eshetu, E. Figgemeier, *J. Energy Storage* **2021**, *43*, 103231.

[9] A. K. Shukla, S. Venugopalan, B. Hariprakash, *J. Power Sources* **2001**, *100*, 125.

[10] M. Li, J. Lu, Z. Chen, K. Amine, *Adv. Mater.* **2018**, *30*, 1800561.

[11] J. Kim, X. Zhang, J. Zhang, A. Manthiram, Y. S. Meng, W. Xu, *Mater. Today* **2021**, *46*, 155.

[12] A. Manthiram, *Nat. Commun.* **2020**, *11*, 1550.

[13] A. Kraytsberg, Y. Ein-Eli, *Adv. Energy Mater.* **2016**, *6*, 1600655.

[14] P. Zhu, P. R. Slater, E. Kendrick, *Mater, Des.* **2022**, *223*, 111208.

[15] J. W. Long, B. Dunn, D. R. Rolison, H. S. White, *Chem. Rev.* **2004**, *104*, 4463.

[16] K. Sun, T. Wei, B. Y. Ahn, J. Y. Seo, S. J. Dillon, J. A. Lewis, *Adv. Mater.* **2013**, *25*, 4539.

[17] K. Fu, Y. Wang, C. Yan, Y. Yao, Y. Chen, J. Dai, S. Lacey, Y. Wang, J. Wan, T. Li, Z. Wang, Y. Xu, L. Hu, *Adv. Mater.* **2016**, *28*, 2587.

[18] J. I. Hur, L. C. Smith, B. Dunn, *Joule* **2018**, *2*, 1187.

[19] Y. Li, B. Tan, Y. Wu, *Nano Lett.* **2008**, *8*, 265.

[20] F. Grote, R. Kuhnel, A. Balducci, Y. Lei, *Appl. Phys. Lett.* **2014**, *104*, 053904.

[21] L. Xue, S. V. Savilov, V. V. Lunin, H. Xia, *Adv. Funct. Mater.* **2018**, *28*, 1705836.

[22] S. D. Lacey, D. J. Kirsch, Y. Li, J. T. Morgenstern, B. C. Zarket, Y. Yao, J. Dai, L. Q. Garcia, B. Liu, T. Gao, S. Xu, S. R. Raghavan, J. W. Connell, Y. Lin, L. Hu, *Adv. Mater.* **2018**, *30*, 1705651.

[23] X. Gao, Q. Sun, X. Yang, J. Liang, A. Koo, W. Li, J. Liang, J. Wang, R. Li, F. B. Holness, A. D. Price, S. Yang, T. Sham, X. Sun, *Nano Energy* **2019**, *56*, 595.

[24] K. Narita, M. A. Citrin, H. Yang, X. Xia, J. R. Greer, *Adv. Energy Mater.* **2021**, *11*, 2002637.

[25] S. Zakeri, M. Vippola, E. Levanen, *Addit. Manuf.* **2020**, *35*, 101177.

[26] D. W. Yee, M. A. Citrin, Z. W. Taylor, M. A. Saccone, V. L. Tovmasyan, J. R. Greer, *Adv. Mater. Technol.* **2020**, *6*, 2000791.

[27] A. C. Martinez, A. Maurel, A. P. Aranzola, S. Grugeon, S. Panier, L. Dupont, J. A. Hernandez-Viezcas, B. Mummareddy, B. L. Armstrong, P. Cortes, S. T. Sreenivasan, E. MacDonald, *Sci. Rep.* **2022**, *12*, 19010.

[28] C. Delmas, C. Fouassier, P. Hagenmuller, *Physica B+C* **1980**, *99*, 81.

[29] C. A. Marianetti, G. Kotliar, G. Ceder, *Nat. Mater.* **2004**, *3*, 627.

[30] J. N. Reimers, J. R. Dahn, *J. Electrochem. Soc.* **1992**, *139*, 2091.

[31] Y. Tian, G. Zeng, A. Rutt, T. Shi, H. Kim, J. Wang, J. Koettgen, Y. Sun, B. Ouyang, T. Chen, Z. Lun, Z. Rong, K. Persson, G. Ceder, *Chem. Rev.* **2021**, *121*, 1623.

[32] S. Xia, J. Lopez, C. Liang, Z. Zhang, Z. Bao, Y. Cui, W. Liu, *Adv. Sci.* **2019**, *6*, 1802353.

[33] Y. Li, J. Li, H. Xiao, T, Xie, W. Zheng, J. He, H. Zhu, S. Huang, *Adv. Funct. Mater.* **2023**, *33*, 2213905.

[34] S. Nakamura, A. Maljuk, Y. Maruyama, M. Nagao, S. Watauchi, T. Hayashi, Y. Anzai, Y. Furukawa, C. D. Ling, G. Deng, M. Avdeev, B. Buchner, I. Tanaka, *Cryst. Growth Des.* **2019**, *19*, 415.

[35] S. Somiya, *Handbook of Advanced Ceramics: Materials, Applications, Processing and Properties*, Academic Press, Waltham, MA **2013**.

[36] E. J. Cheng, N. J. Taylor, J. Wolfenstine, J. Sakamoto, *J. Asian Ceram. Soc.* **2017**, *5*, 113.

[37] S. Yu, D. J. Siegel, *ACS Appl. Mater. Interfaces* **2018**, *10*, 38151.

[38] W. C. Oliver, G. M. Pharr, *J. Mater. Res.* **1992**, *7*, 1564.

[39] L. Wu, J. Zhang, *J. Appl. Phys.* **2015**, *118*, 225101.

[40] M. Qu, W. H. Woodford, J. M. Maloney, W. C. Carter, Y. Chiang, K. J. Van Vliet, *Adv. Energy Mater.* **2012**, *2*, 940.

[41] J. J. Vlassak, W. D. Nix, *Phil. Mag. A* **1993**, *67*, 1045.

[42] J. J. Vlassak, W. D. Nix, *J. Mech. Phys. Solids* **1994**, *42*, 1223.

[43] J. W. Fergus, *J. Power Sources* **2010**, *195*, 939.

[44] M. S. Whittingham, *Proc. IEEE* **2012**, *100*, 1518.

[45] M. Malik, K. H. Chan, G. Azimi, *Mater. Today Energy* **2022**, *28*, 101066.

[46] Y. Hu, M. M. Doeff, R. Kostecki, R. Finones, *J. Electrochem. Soc.* **2004**, *151*, A1279.

[47] H. Liu, Y. P. Wu, E. Rahm, R. Holze, H. Q. Wu, *J. Solid State Electrochem.* **2004**, *8*, 450.

[48] X. Cheng, R. Zhang, C. Zhao, Q. Zhang, *Chem. Rev.* **2017**, *117*, 10403.

[49] D. Lin, Y. Liu, Y. Cui, *Nat. Nanotechnol.* **2017**, *12*, 194.

[50] X. Yan, L. Lin, Q. Chen, Q. Xie, B. Qu, L. Wang, D. Peng, *Carbon Energy* **2021**, *3*, 303.

[51] A. Zhang, X. Fang, C. Shen, Y. Liu, C. Zhou, *Nano Res.* **2016**, *9*, 3428.

[52] H. Wang, D. Lin, J. Xie, Y. Liu, H. Chen. Y. Li, J. Xu, G. Zhou, Z. Zhang, A. Pei, Y. Zhu, K. Liu, K. Wang, Y. Cui, *Adv. Energy Mater.* **2019**, *9*, 1802720.

[53] H. Yang, E. O. Fey, B. D. Trimm, N. Dimitrov, M. S. Whittingham, *J. Power Sources* **2014**, *272*, 900.

[54] K. Yan, Z. Lu, H. Lee, F. Xiong, P. Hsu, Y. Li, J. Zhao, S. Chu, Y. Cui, *Nat. Energy* **2016**, *1*, 16010.

[55] M. Shafiei, A. R. Riahi, F. G. Sen, A. T. Alpas, *Surf. Coat. Tech.* **2010**, *205*, 306.

[56] M. Todeschini, A. Bastos da Silva Fanta, F. Jensen, J. B. Wagner, A. Han, *ACS Appl. Mater. Interfaces* **2017**, *9*, 37374.

[57] T. Christen, M. W. Carlen, *J. Power Sources* **2000**, *91*, 210.

[58] K. Narita, M. A. Saccone, Y. Sun, J. R. Greer, *J. Mater. Res.* **2022**, *37*, 1535.

[59] H. Zhang, H. Ning, J. Busbee, Z. Shen, C. Kiggins, Y, Hua, J. Eaves, J. Davis III, T. Shi, Y. Shao, J. Zuo, X. Hong, Y. Chan, S. Wang, P. Wang, P. Sun, S. Xu, J. Liu, P. V. Braun, *Sci. Adv.* **2017**, *3*, e1602427.

[60] Z. Hua, Y. Liu, G. Yao, L. Wang, J. Ma, L. Liang, *J. Mater. Eng. Perform.* **2012**, *21*, 324.

[61] G. T. Hill, F. Shi, H. Zhou, Y. Han, C. Liu, *Matter* **2021**, *4*, 1611.

[62] C. Liu, Y. Li, D. Lin, P. Hsu, B. Liu, G. Yan, T. Wu, Y. Cui, S. Chu, *Joule* **2020**, *4*, 1459.

[63] Y. Li, F. Cui, M. B. Ross, D. Kim, Y. Sun, P. Yang, *Nano Lett.* **2017**, *17*, 1312.

[64] C. Xie, Z. Niu, D. Kim, M. Li, P. Yang, *Chem. Rev.* **2020**, *120*, 1184.

[65] C. Chen, Y. Li, S. Yu, S. Louisia, J. Jin, M. Li, M. B. Ross, P. Yang, *Joule* **2020**, *4*, 1688.